TÉCNICO LISBOA

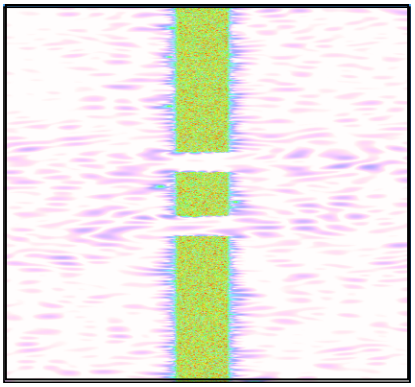

Nanoplasmonics at high laser intensities

João Tiago Serra Garcia Branco

Thesis to obtain the Master of Science Degree in

Engineering Physics

Supervisors: Doctor Marta Leitão Mota Fajardo
Doctor Hamed Merdji

Examination Committee

Chairperson: Professor Horácio João Matos Fernandes
Supervisor: Doctor Marta Leitão Mota Fajardo
Members of the Committee: Doctor Jorge Miguel Ramos Domingues Ferreira Vieira

November 2015

Dedicated to Eduardo Hermínio Serra

Acknowledgments

In a moment of such importance in my life, my gratitude is extended to the ones who helped me during this academic stage and also to those who left a mark on me and let me come this far.

First of all, I would like to start by thanking the ones who were directly involved in the work conducted for this master thesis and made all this possible: my advisors Dr[a]. Marta Fajardo, who admitted me on behalf of Group of Lasers and Plasmas (*GoLP*) and showed enthusiasm for the accomplishment of this project ever since the first day, and Dr. Hamed Merdji, whose interest in Ultrafast Optics and in Nanoplasmonics contributed for the consolidation of this investigation work. I cannot forget all the other fellow workers at GoLP who gave me the support I needed for solving the problems that came up during this task. A great, great thank to Swen Künzel (*Vielen Dank Sven!*), the (not so) German member of the group, for all the patience while helping me with the work towards the best direction. My thanks are also given to Paulo Alves and Fábio Cruz, for the clarifications regarding the simulation tools employed. Thank you too André Lopes, for the good company either at GoLP or during my college life, and for sharing all the nerves with me for the conclusion of this thesis. And my gratitude also to André Boné, for all the contribution and support given for the accomplishment of my work. To the people at the *Institut für Quantenoptik* in Hannover, where my interest in laser optics began to raise and where I had a wonderful opportunity, my kind regard in particular to Prof. Uwe Morgner, for accepting me for the internship during my Erasmus, and to José Andrade, for aiding me during the laboratory work.

Secondly, my gratitude goes to those of unconditional importance and with whom I spent the entire life with, my family. The first people that come to my mind are the ones who have been with me since the first minute: my father António and my mother Maria do Céu, thank you for all the guidance during these 23 years and for all the sustaint you gave me and still give; my gratitude to my sister Mariana, you are the company a brother truly needs and you have always given me the support for the hard moments; and to the rest of my family: grandparents, uncles, cousins and godparents: *Obrigado família!*

Thirdly, I recall those with whom I shared many good moments in my life. The people for the best occasions and who were with me these last 8 years of my life: Vasco Pires, Miguel Santos, Hugo Lopes, Rúben Silva and Hugo Almeida, thank you for all the help, all the companionship and positivity you all brought to me, with friends like you everybody got time for that. For the great years spent at the Instituto Superior Técnico, a big thank to all the Physicists with whom I have shared many good moments since the year of 2010 in this big institution.

A part of me remains in Hannover and there I realized that big friendships are not language dependent. This effort was also due to you my friends: Laura Quick, my friend from Carangola in Brazil who turned out to become one of my best friends, I thank you for the all the support, for all the adventures and for all the joy given especially during my stay in Germany; the J.M.M.K. group (me, Marius, Martina and Kasia), we all spent nice moments in Germany and I am truly glad to have met you; all the B1 class from the Deutsch Intensivkurz in Hannover, you are the best.

Finally, a special thank to a person who means so much and who is a part of my life. My heartfelt gratitude to you Selen, for always being there for the right moments and for giving me the *light* I need.

Resumo

À luz da evolução tanto das intensidades geradas pelos sistemas de laser bem como dos algoritmos computacionais de simulação, torna-se interessante investigar até que ponto poderemos aproveitar estas novas potencialidades no sentido de dar suporte a hipotéticas investigações experimentais futuras. Nesse contexto, a interacção luz-matéria revela ser um campo de estudo cujas bases podem ser consolidadas através destas novas ferramentas. Em particular, sendo ultrapassadas as dificuldades na obtenção de intensidades maiores e comprimentos de onda menores, é possível estudar a estrutura de materiais de determinada composição e configuração com maior detalhe.

Poder-se-á extrapolar esta ideia para um metal, como uma folha de Titânio, objecto que estará na base do presente trabalho. Será utilizado um código *PIC* (Partícula em Célula), designado *OSIRIS*, para a simulação de um plasma ultra denso como representação de uma estrutura metálica de espessura de 100 nm e com duas fendas de 300 nm, separadas por 600 nm. Esta simulação aplica-se sobretudo ao bombeamento do sistema, envolvendo a emissão de pulsos laser de 800 nm de comprimento de onda com intensidades entre 10^{14} W/cm^2 e 10^{16} W/cm^2. Os diagnósticos relevantes para analisar durante o tempo de interacção serão a evolução da densidade das espécies, da intensidade do campo eléctrico e dos perfis de temperatura da estrutura.

Esta informação torna-se útil na perspectiva de desenvolver um esquema de montagem laboratorial capaz de efectuar a sonda de um sistema para um alvo em expansão, implementando harmónicos de intensidade reduzida através da folha de dupla fenda.

Palavras-chave: Nanoplasmónica, Titânio, *OSIRIS*, Bombeamento, Sonda

Abstract

In light of the evolution either from generated intensities by the laser systems and from computational simulation algorithms, it becomes interesting to investigate how deep one can take advantage of such potential in order to give support on hypothetical future experimental investigations. Hence, light-matter interaction proves to be a field of study whose basis can be consolidated through these new tools. In particular, by overcoming the difficulties in obtaining bigger intensities and lower wavelengths, it becomes possible to study in detail the structure from materials of specific composition and configuration.

One can extrapolate this idea to a metal, like a Titanium foil, object which will be on the basis of the current work. A *PIC* (Particle-in-Cell) code, called *OSIRIS* is used to simulate an ultra dense plasma as a resemblance of a metallic structure with 100 nm of thickness and two 300 nm sized slits, separated by 600 nm. This simulation will be directed predominantly to the pumping of the system, involving the emission of 800 nm wavelength laser pulses with intensities between 10^{14} W/cm^2 and 10^{16} W/cm^2. The relevant diagnostics to analyse during the interaction time are the evolution of the species' density, of the electric field intensity and of the structure's temperature profiles.

This information becomes therefore useful for an attempt to develop a setup which is able to perform a probing of the system for an expanding target, by implementing harmonics of low intensity through the double slitted foil.

Keywords: Nanoplasmonics, Titanium, *OSIRIS*, Pumping, Probing

Contents

Acknowledgments v
Resumo vii
Abstract ix
List of Tables xiii
List of Figures xvi
Nomenclature 1
Glossary 1

1 Introduction **1**
1.1 Motivation 2
1.2 State of the art 3
1.2.1 Nanoplasmonics 3
1.2.2 Plasma simulation tools 5
1.2.3 Experimental plasma diagnostics 7
1.3 Objectives 9

2 Laser-Solid Interaction **11**
2.1 Laser Absorption Processes 11
2.1.1 Collisional absorption 12
2.1.2 Collisionless absorption 15
2.2 Solid heating, thermal conduction and expansion 19
2.2.1 Two-Temperature Model - TTM 19
2.2.2 Alternative approaches 20
2.2.3 Laser Induced Ablation 22
2.3 Nanoplasmonics 24
2.3.1 Field Enhancement 25
2.3.2 Harmonic Generation 26

3 Experiment and Simulation **31**
3.1 Experiment - CEA 31
3.2 OSIRIS Simulation Parameters 32
3.2.1 Titanium plasma parameters 32

3.2.2 Titanium specie parameters . . . 33
3.2.3 Foil geometry parameters . . . 35
3.2.4 Laser pump parameters . . . 35

4 Results - OSIRIS Simulations 37
4.1 Laser beam . . . 38
4.1.1 No foil . . . 38
4.1.2 With foil . . . 38
4.2 Temperature profiles - 1D . . . 39
4.3 Temperature and density profiles . . . 42
4.3.1 Temperature . . . 42
4.3.2 Density . . . 46
4.3.3 Temperature and density lineouts . . . 47
4.4 Field Enhancement . . . 49
4.4.1 $I_0 = 10^{14}\ W/cm^2$ . . . 51
4.4.2 $I_0 = 10^{15}\ W/cm^2$ . . . 52
4.4.3 $I_0 = 10^{16}\ W/cm^2$ . . . 53
4.4.4 Smaller slit size . . . 54

5 Discussion of Results 55
5.1 Comparison with temperature models . . . 55
5.1.1 Two Temperature Model . . . 55
5.2 Analysis of results . . . 59
5.2.1 Temperature and expansion . . . 59
5.2.2 Field Enhancement . . . 60

6 Conclusions 62
6.1 Achievements and improvements . . . 62
6.2 Future Work . . . 63
6.2.1 OSIRIS . . . 64
6.2.2 Plasma diagnostics . . . 64

Bibliography 70

List of Tables

2.1 Metal coefficients 20

3.1 Titanium plasma parameters 33
3.2 Thermal speed - electrons and protons 34
3.3 Laser beam parameters 35
3.4 OSIRIS laser parameters 36

5.1 TTM model parameters - Gold 56
5.2 TTM model parameters - Titanium 58

List of Figures

1.1 Conventional light and lasers . . . 1
1.2 Recent Laser Applications . . . 2
1.3 Instantaneous snapshot of the localization of an optical field in a nanosystem . . . 4
1.4 Plasmonic colors . . . 5
1.5 Vlasov and PIC approaches . . . 6
1.6 *OSIRIS* mechanism . . . 7
1.7 Examples of CDI imaging systems . . . 8

2.1 Brunel heating - capacitor approximation . . . 16
2.2 Resonance absorption . . . 18
2.3 Threshold Fluence of Cu . . . 23
2.4 Ablation depth - Cu, Ag and W . . . 24
2.5 Finite-difference time-domain simulation of local field enhancement. . . . 25
2.6 SHG, SFG and DFG . . . 27
2.7 Spectrum of high-order harmonic pulse . . . 28
2.8 Electron trajectories of an electron - non-relativistic case . . . 29
2.9 Electron trajectories of an electron - relativistic case . . . 29
2.10 Apparatus for high-harmonic generation by electric field enhancement . . . 30

3.1 Lab Setup . . . 32
3.2 Ionization degree for Titanium . . . 33
3.3 Collision frequency of solid Al as a function of the temperature . . . 35
3.4 Titanium foil display . . . 36

4.1 2D simulation window . . . 37
4.2 Laser beam - no foil . . . 38
4.3 Laser beam - with foil . . . 39
4.4 1D analysis ($I_0 = 10^{14}$ W/cm^2) . . . 40
4.5 1D analysis ($I_0 = 10^{15}$ W/cm^2) . . . 41
4.6 1D analysis ($I_0 = 10^{16}$ W/cm^2) . . . 41
4.7 Full 2D ($I_0 = 10^{14}$ W/cm^2) . . . 43
4.8 2D Maximum Temperatures ($I_0 = 10^{14}$ W/cm^2) . . . 43

4.9 Full 2D ($I_0 = 10^{16}$ W/cm^2) . . . 44
4.10 2D Maximum Temperatures ($I_0 = 10^{16}$ W/cm^2) . . . 45
4.11 2D profile of Ti foil evolution ($I_0 = 10^{14}$ W/cm^2) . . . 46
4.12 2D profile of Ti foil evolution ($I_0 = 10^{16}$ W/cm^2) . . . 47
4.13 Longitudinal lineouts ($I_0 = 10^{14}$ W/cm^2) . . . 48
4.14 Transverse lineouts ($I_0 = 10^{14}$ W/cm^2) . . . 48
4.15 Longitudinal lineouts ($I_0 = 10^{16}$ W/cm^2) . . . 48
4.16 Transverse lineouts ($I_0 = 10^{16}$ W/cm^2) . . . 49
4.17 Field Enhancement 2D view ($I_0 = 10^{15}$ W/cm^2) . . . 50
4.18 Field enhancement lineouts ($I_0 = 10^{14}$ W/cm^2) . . . 51
4.19 Field enhancement peak ($I_0 = 10^{14}$ W/cm^2) . . . 51
4.20 Field enhancement lineouts ($I_0 = 10^{15}$ W/cm^2) . . . 52
4.21 Field enhancement peak ($I_0 = 10^{15}$ W/cm^2) . . . 52
4.22 Field enhancement lineouts ($I_0 = 10^{16}$ W/cm^2) . . . 53
4.23 Field enhancement peak ($I_0 = 10^{16}$ W/cm^2) . . . 53
4.24 Field enhancement peak - smaller slit . . . 54

5.1 TTM model - Gold ($I_0 = 1 \times 10^{10}$ W/cm^2) . . . 56
5.2 TTM (Majchrzak and Dziatkiewicz) . . . 56
5.3 TTM model - Gold ($I_0 = 3.57 \times 10^{11}$ W/cm^2) . . . 57
5.4 TTM (Tsai and Jiang) . . . 57
5.5 TTM model ($I_0 = 10^{14}$ W/cm^2) . . . 58
5.6 TTM model ($I_0 = 10^{15}$ W/cm^2) . . . 59
5.7 TTM model ($I_0 = 10^{16}$ W/cm^2) . . . 59

Chapter 1

Introduction

Little did the scientific community realize that the process suggested by Albert Einstein in 1917, called *Stimulated Emission*, was carrying itself a tremendous potential and was the first step for a modern era. At the time, most light forms were diffuse and non-coherent, meaning that the light waves were distributed in several directions and that their phase relationship was not fixed, respectively (fig. 1.1). But through Einstein's process, the door was open for the conception of an extremely coherent and approximately monochromatic form of light, which is currently known as *Laser* (**L**ight **A**mplification by **S**timulated **E**mission of **R**adiation). Only until the 1950's experimental research was carried in order to develop the first laser systems by applying the theory of stimulated emission. On May 1960, the first laser system was made by Theodore Maiman, out of synthetic ruby, with a pulse duration between 1ms and 1μs. Through the development of techniques such as the *Q-switching* (Hellwarth 1961), active mode locking (Hargrove et al. 1964) and passive mode locking (Mocker and Collins 1965; DeMaria et al. 1966), a step was given to the pulse durations that could go from the nanosecond scale (10^{-9} s) down to the picosecond scale (10^{-12} s).

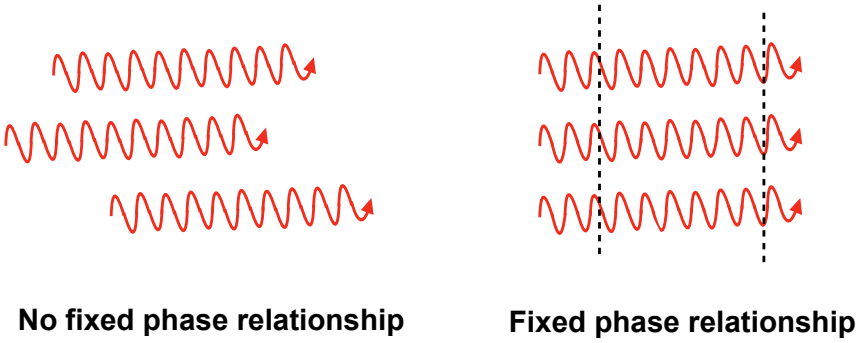

Figure 1.1: Difference between conventional light (left) and laser light (right)

In 1985 (Strickland and Mourou, 1985) the *ultrashort* pulse era is reached, through combining mode-locking with the concept of chirped pulse amplification (CPA). The pulses are stretched in time (chirped in frequency), amplified and finally recompressed (Perry and Mourou, 1994). Pulses could reach some

femtoseconds (10^{-15} s) in pulse duration and peak powers bigger than a Gigawatt ($> 10^{12}$ W).

Soon after this invention, there was a 'boom' of many ideas for laser applications, from worldwide communication to space research, from cutting edge technology to fields like chemistry and medicine (fig. 1.2). It is reasonable to state that the early pioneers of laser technology would be astonished to see the multitude of ways that lasers are used by everyone, everyday, in today's world.

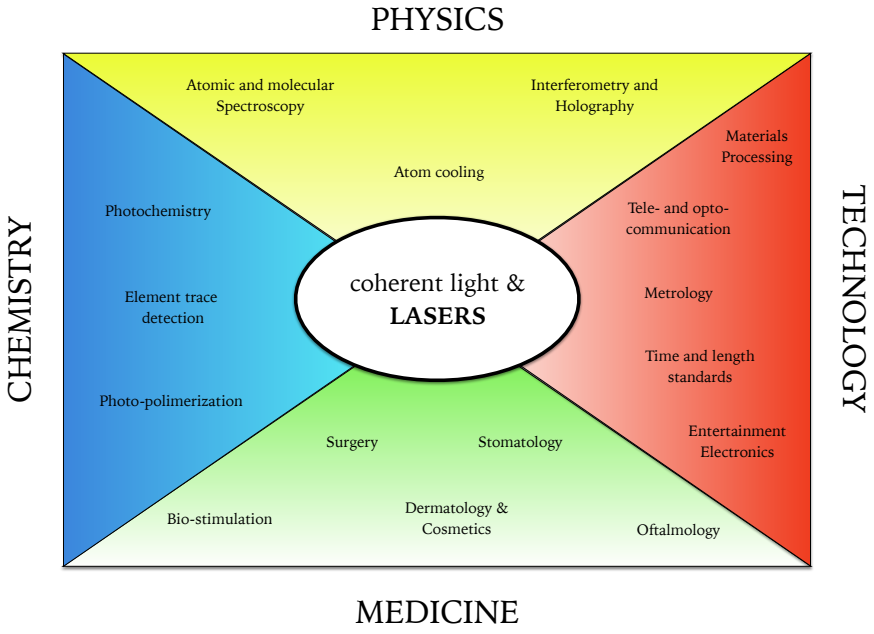

Figure 1.2: Recent Laser Applications - an overview (adapted from [1]).

One application of lasers in fundamental research is the interaction of matter with intense light, which leads to the field of plasma physics. For the interest of this thesis, one can scale plasma events down to the nanoscale. The study of such conditions is condensed in one of the emerging fields of study for laser-solid interaction physics, which is called *Nanoplasmonics* [2].

1.1 Motivation

One of the features in laser-matter interaction that was significant for scientists over the last two decades was laser absorption because of its relevance in several high intensity applications, such as hot electron production for fast ignition of fusion targets, bright X-Ray and Gamma-Ray sources, ion acceleration or the creation of high energy dense matter.

As mentioned before, this field of study joins the concepts of *Laser* and *Plasma*. As a laser hits a solid structure, it will suffer a transition from solid state, going to liquid state, and finally to the gas state. The continuous laser heating will create an electrified media, with former neutral particles giving place to positive and negative charges split. This is known as plasma state, which is the fourth state of matter.

Nevertheless, efficient use of lasers for precise material processing, for example, is impossible without a thorough knowledge of the fundamental laws governing the interaction of laser radiation with

matter. For such purpose, and to achieve a better understanding of phenomena in nature, such as the electron-phonon interaction in a crystal or hot electron generation, systematic studies of laser-matter interaction are required.

The work developed for this master thesis is aimed to reinforce the development of this area, and is targeted towards the investigation of a particular study case - the interaction of a moderate-to-intense laser beam with a metallic target configuration made of Titanium (Ti). For this task, precise computational interfaces are mandatory, which is accomplished by employing a compute-intensive model of plasma physics.

Nowadays there are several numerical tools with different approaches which can be used in order to perform plasma state modelling. Hydrodynamic codes are the standard methods implemented for these solid matter cases, since they are accurate for collective effects in very high densities and for the description of macroscopic properties (particle mass, equations of state, opacity, conductivity, etc.). But in the context of this thesis, where microscopic and short time scale events are very likely to be created, a kinetic code becomes more adequate for the purpose. The employed plasma modelling code, called *PIC Code* (Particle-in-Cell code), is developed from kinetic theory and is sustained by a self-consistent algorithm that provides the electromagnetic fields by particle interaction (subsection 1.2.2).

As theoretical and experimental work hold hands together, with this study one achieves not only to strengthen the understanding of the dynamics for ultrafast events during the interaction between a laser and a solid density plasma, but also to help developing new ways for plasma-solid matter diagnostics and to confer support for eventual future laser-solid interaction experiments. Its short-term purpose is to provide results to the experimental team at the CEA (*Commissaritat à l'énergie atomique et aux énergies alternatives*) Institute from Saclay (Paris, France), who is carrying out this experiment in their laser laboratory facility.

1.2 State of the art

1.2.1 Nanoplasmonics

As mentioned in the previous section, the process of irradiating a metallic target with a laser beam involves a cycle of state transitions, from solid to plasma. Our Ti target is nanometer sized, and plasma events taking place will lie on the nanometer scale, which makes it relevant to this *Nanoplasmonics* field of study.

Nanoplasmonics, as the word might suggest, is the study of optical phenomena that arise in the nanoscale vicinity of metallic surfaces. Typically, the dimensions of the target should be small enough compared to the wavelength for these nanoplasmonic events be likely to happen (from [3], $\lambda/\delta_{target} \gtrsim 40$ is a good optimization ratio).

To first approximation, one can see it as a collective motion of free electrons from the metallic nanoparticle, like in the Drude model for a metal. These electrons are periodically displaced from the lattice ions when exposed to an external field, generating a differential concentration of positive and

negative charges at opposite surfaces. Electrons then generate an oscillator, whose energy is carried by the exploitation of *surface plasmons* (SP) - quanta of plasma oscillation -, with a frequency depending on the electronic mass and its restoring force. Typically, this restoring force depends on the size and shape of the metallic structure, as well as on the dielectric material on its neighbourhood (fig. 1.4).

On a scale of a few nanometers, the light incident on nanoplasmonic particles gives rise to an inhomogeneous distribution of intense and highly localized electric fields. Such local intensity spikes, which Lakshmi Pandey, Thomas George and Mark Stockman [4] studied in 1996, are recognized as one of the most important and universal phenomena in Nanoplasmonics (explanation in chapter 2).

This relatively young science endorses several innovate applications, most of which exploit this enhancement of local optical fields on tiny metal particles. Some applications are:

- **Oncology**: thermal phototherapy of tumors using gold shell core nanoparticles [5]
- **Pregnancy tests**: implementation of gold nanospheres linked to secondary antibodies, to spectral shift the barely visible scattered light by human chorionic gonadotropin hormone (hCG) produced in the beginning of pregnancy
- **Solar energy**: plasmon-assisted solar energy conversion by coupling solar radiation to semiconductor photovoltaic elements through the use of metal nanostructures [6]
- **Optical component fabrication**: light filter by extraordinary transmission though nanometer-scale holes in engineered metal substrates
- **Stained glass**: insertion of metallic colloidal suspensions in stained glass to originate light scattering phenomena at visible frequencies due to nanoplasmonic resonances (Exs.: Lycurgus Cup at the British Museum, UK or *Sainte Chapelle* in Paris, France)
- **Metamaterials**: development of novel materials which can exploit surface plasmons in order to modify the refractive index and therefore achieve optical properties not seen in nature

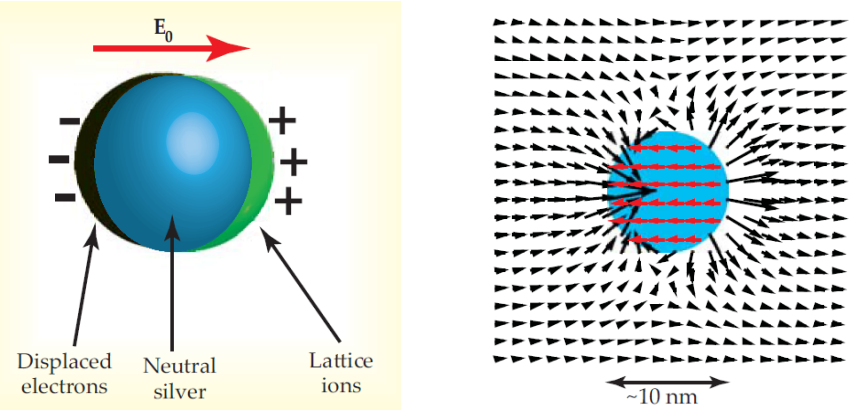

(a) $\vec{\mathbf{E}}$ field displacement of electrons and ions - SP creation

(b) Surface electric field amplification

Figure 1.3: An instantaneous snapshot of the localization of an optical field in a nanosystem (silver sphere). The surface plasmons are initially created after the exposure to an external field (a), leading to the creation of an amplified electric field of displaced electrons (black arrows) on the surrounding of the sphere (b) (from [2]).

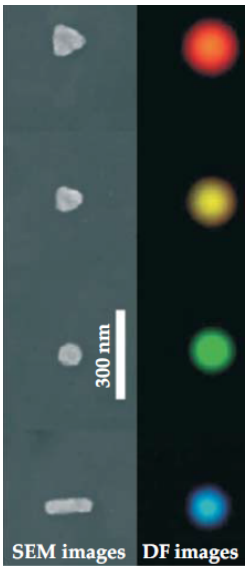

Figure 1.4: Gold nanoparticles imaged with scanning electron microscopy. The distinctly coloured light emission illustrates that the metal's resonance frequency can be tuned by varying its size and shape (from [3])

1.2.2 Plasma simulation tools

A big issue to untangle before beginning any kind of simulation is knowing the detail required for the description of the system, in the present case a plasma, which can depend on distinct elements such as the plasma initial state, reference time/length scales and the expected results that one might observe. The problem proves to be a puzzling task, as it comprehends transitions between two completely opposite states of matter: solid and plasma.

As pointed out previously, the hydrodynamic code is usually the favourite approach for most solid density plasma simulations. They work by solving the fluid equations from conservation laws - Lagrangian methods - where the coordinates move with the fluid and whose resolution can be adjusted with respect to different parameters.

Nonetheless, nanoplasmonic effects that might happen with the implementation of femtosecond laser pulses cannot be managed by this same approach. Besides, one peculiar aspect of ultrashort laser pulses is the fact that laser absorption becomes highly dependent on either target structure and preplasma conditions for these pulse durations [7]. These events are *kinetic* or *Maxwellian* sort, which is the main scope from PIC codes.

PIC Codes represent a breaking new alternative for plasma simulation, centred on microscopic features described through kinetic theory.

In the simplest kinetic description of a plasma, one starts from the particle velocity distribution function $f(\mathbf{r}, \mathbf{v})$, which evolves according to the Vlasov equation (Elliot, 1993):

$$\frac{\partial f}{\partial t} + \mathbf{v} \cdot \frac{\partial f}{\partial \mathbf{x}} + q\Big(\mathbf{E} + \frac{\mathbf{v}}{c} \times \mathbf{B}\Big) \cdot \frac{\partial f}{\partial \mathbf{p}} = 0 \tag{1.1}$$

As $f(\mathbf{r}, \mathbf{v})$ is 6-D, the general solution becomes a tedious task to solve. The PIC allows to overcome this problem (fig. 1.5).

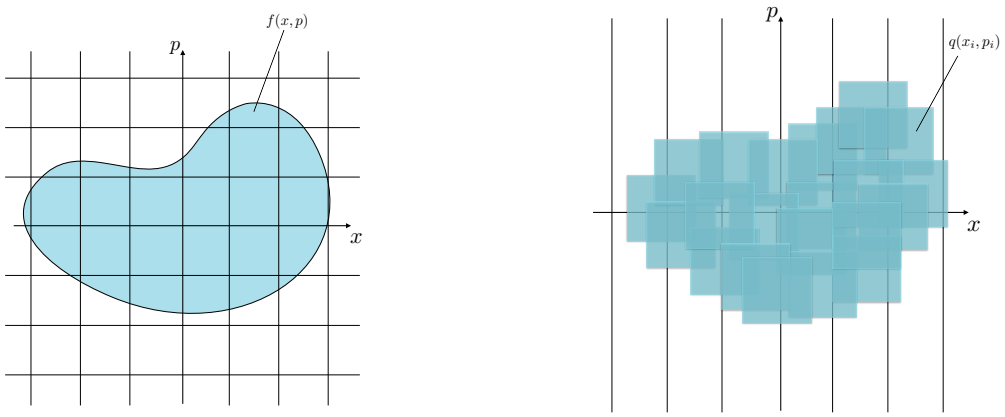

(a) Vlasov approach (b) PIC approach

Figure 1.5: Difference between Vlasov (left) and PIC (right) approaches (adapted from [8])

The first variation of this technique was developed by John M. Dawson in 1962, by creating the '1D1V' configuration (1 space coordinate plus 1 velocity). More recently, and thanks to the advances in computing power, fully electromagnetic simulations with 3 space coordinate and 3 velocities - '3D3V' - were conceived and placed PIC Codes as the state-of-the-art technique for plasma simulations [9],[10].

The two primary simplifying assumptions used by PIC codes are the use of macroparticles and the partial discretization of space and time. A macroparticle is a single simulation particle that represents a distribution of real particles and is typically a cluster on the order of 10^6–10^{10} real particles [11]. The macroparticle has continuous, well-defined velocity and position vectors, and has the same charge/mass ratio as the particles it represents, thus the same equation of motion. Effectively, using macroparticles instead of many real particles is equivalent to do a sampling of the full six-dimensional phase space for real particles, converging therefore on the correct answer with a sufficient resolution, as with any sampling. PIC simulations include a self-consistent treatment of fields and particles and, in principle, zero-fitting parameters, but they still allow for realistic target sizes giving access to the full damage morphology. Although the macroparticle position is continuous, real space is broken up into a grid consisting of nodes and cells. The grid is used to discretize fields and currents that are evaluated only at the nodes and each one of the aggregated cells is labelled with a given mass m_i and charge q_i.

In spite of existing some few examples of electron dynamic modulation in metal laser damage, only now began PIC codes to be included in the study of laser damage itself. The implemented framework was developed in Fortran-90 and is called *OSIRIS* [10], a three-dimensional, relativistic, massively parallel, object oriented particle-in-cell code.

The particles are placed within the grid, in whose vertices is deposited their charge and current. The new $\mathbf{E}$ and $\mathbf{B}$ fields by integrating Maxwell's equations, and from the Lorentz force equation the particles' new position is found. A new set of charge and current densities is then created and this cycle goes on again successively (fig. 1.6).

OSIRIS is characterized by the fact that every quantity is normalized to electron parameters, like electron mass m_e, electron charge e, electron plasma frequency ω_{pe} or light speed c. Length, time, electric field **E'** or energy K' are written as follows:

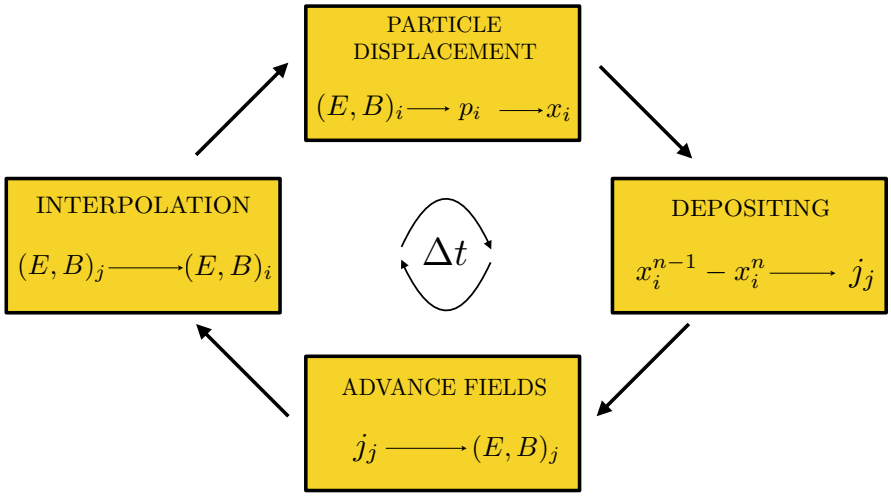

Figure 1.6: *OSIRIS* working mechanism (adapted from [12])

$$\mathbf{x}' = \left(\frac{\omega_{pe}}{c}\right)\mathbf{x} \tag{1.2}$$

$$t' = \omega_{pe} t \tag{1.3}$$

$$\mathbf{E}' = \left(\frac{e\omega_{pe}}{m_e c}\right)\mathbf{E} \tag{1.4}$$

$$K' = \left(\frac{1}{m_e c^2}\right)K \tag{1.5}$$

1.2.3 Experimental plasma diagnostics

For probing a target evolution in a real experiment we need first to account for the size of the objects we are studying, which is in this case much below the resolution limit of the typical laser light that is used (diffraction limit $\sim \lambda$). Short wavelength will allow a smaller diffraction limit with extreme ultra violet radiation (30 - 150 nm) originated from HHG (explanation in Chapter 2). From the so-called *Maréchal criterion*, a wavefront can be regarded as diffraction-limited if its RMS phase error is 14 times less than its wavelength. This implicates that, for XUV, the dimensions for the optics involved should be lower than the Å, meaning that an alternative to the conventional optics techniques, like a lensless imaging method, should be employed to image the plasma.

Two well-known lenssless imaging methods are: *coherent diffraction imaging* and *holography*.

Coherent diffraction imaging (CDI)

X-ray Crystallography has a record of extraordinary achievements in science, as it had a big impact on different branches of Physics. It was originally used to reconstruct 3D atomic-resolution images of molecules from beams diffracted by their crystal forms. However, with respect to macromolecular crystallography, the crystallographer David Sayre re-adapted the methods of crystallography for imaging general non-periodic objects, and for that he developed a new ”lensless”, very high spatial resolution

technique [13].

Imaging individual objects, with a few nanometer resolution in space and a few femtosecond resolution in time is relevant in many areas of science and represents a fascinating challenge today. Hence, advances in coherent diffraction using new coherent ultrashort x-ray sources have actually shown a high potential.

Coherent diffraction imaging (CDI) overcomes many restrictions, offering means to produce images of non-crystalline objects at a resolution, in principle, limited by the wavelength only. In this lensless technique, a spatially coherent laser beam hits an isolated sample (surrounded by a zero-scattering area), and the far-field diffraction pattern of the object is recorded on an area detector, generally by a CCD camera. Since the detector records only the diffracted intensities, the "real image" is obtained from the amplitude and phase diffraction pattern using an iterative algorithm based on Fourier transforms. In figure (fig. 1.7) some techniques are displayed.

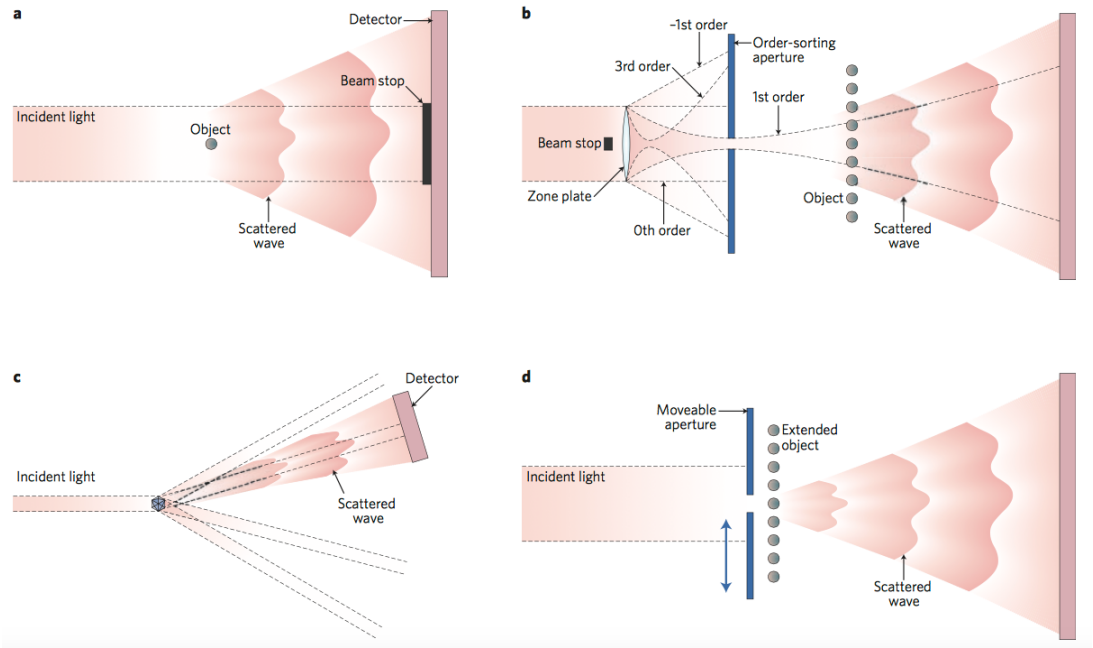

Figure 1.7: Examples of imaging systems - a) *Plane Wave CDI*; b) *Fresnel CDI*; c) *Bragg CDI*; d) *Scanning diffraction microscopy* (from [14])

Recently some other innovative techniques came up with innovative methods - *single-shot CDI with XUV* [15] and *CDI with XUV using nanofocused illumination* [16] are two examples of those.

Holography

After being influenced by the work of scientists such as W.L.Bragg on x-ray crystallography, Dennis Gabor came to a new idea in 1948 that could be useful for optical devices and its applications. This relatively cutting-edge mechanism, at the time called *wavefront reconstruction*, is today known as holography.

In this process, again without additional lenses, the object light waves interfere with a reference picture and whose interference pattern is recorded through a CCD, what we call a *hologram* [17]. The holographic method consists on two operations: *recording* and *reconstruction*. Since the wavefronts are coherent, we need to detect information about the amplitude and phase of the waves. However, recording media respond only to light intensity, requiring therefore that the phase information must somehow be converted to intensity variations for recording purposes. The technique for accomplishing this task is based on interferometry as we mentioned; that is, the original wave of amplitude U_0 is mixed with a reference wave U_r, and their interference pattern is recorded. The intensity of the wave sum is gathered in a CCD camera and reconstructed numerically (the recipe for the so-called digital holography). To decode the information in the hologram and reconstruct the object wave, the reference wave U_r, is again used to illuminate the hologram.

This field has had several applications in Physics and in today's World, namely: Microscopy, Interferometry, Imaging through distorting media, Data storage, Artificial Neural Networks, Holographic Art or Security. Some improvements for this technique were achieved by the implementation of innovative methods: *X-ray holography with customizable reference* [18], *Multiple reference Fourier transform holography with soft x rays* [19], etc...

1.3 Objectives

In this thesis, the main task will be the investigation of the interaction between an ultrafast and ultraintense Ti:sapphire laser (800 nm) with a metallic foil made of Titanium. The foil is designed as a dense plasma in OSIRIS, which is in good agreement with established temperature models.

A simulation with a duration $\leq$ 15 ps to investigate the density and temperature profiles is executed. On the other hand, electric field intensity analysis is performed within a temporal window slightly longer than the pulse duration, typically until a few femtoseconds after the interaction of the pulse with the foil.

With these diagnostics it will be possible to estimate the results for upcoming experiments of such nature and to explore new ways to implement an imaging setup to picture the evolution of an expanding plasma. The general scope on the tasks for this thesis, having in mind the work projected at CEA, is given below:

- **EXPERIMENT AT CEA**
    - Describe a laser pump experiment with plasmonic field effects
    - Investigate modifications from the dynamics of the system by enhanced field effects
    - Discuss the application of high harmonics to perform imaging diagnostics of the system

Chapter 2

Laser-Solid Interaction

The understanding of the behaviour of solid objects when exposed to a laser field, especially the mechanism from which they absorb light, is an important issue attracting continued interest since the invention of lasers. In the 1960s, when the concept of *confined inertial fusion* had been proposed, laser absorption and plasma heating immediately received attention. The mechanisms that take place in different cases will depend on the intensity imposed: if the laser has a moderate intensity (between 10^{13} W/cm^2 and 10^{15} W/cm^2) the absorption can be dominated either by *inverse bremmstrahlung*, *multiphoton ionization* or also *collisional absorption* during the laser-solid interaction; for bigger intensities ($\geq 10^{16}$ W/cm^2), collisionless absorption processes can play a bigger role, leading to phenomena like *resonance absorption* or *vacuum heating*. Generally speaking, the absorption depends upon the laser parameters - intensity, wavelength, pulse duration and polarization - and target properties - density distributions, shape, materials and temperature. When the laser approaches 10^{18} W/cm^2, relativistic effects become more significant, and the laser ponderomotive force becomes high enough to accelerate electrons directly. This generates highly non-linear processes, showing strong kinetic effects which complicate the laser absorption problem. In these cases the kinetic numerical methods inherent to PIC codes are again a good starting point to understand the physics involved.

With *Chirped Pulse Amplification* techniques, compact ultrashort laser pulse sources can be created, and the introduction of these in experiments featured plasma density scale lengths as short as less than a laser wavelength [7].

The way a plasma absorbs light waves is then an outspread question with different answers, each of them leading to different particle activity and introducing changes in the thermodynamic properties of the system. In the coming sections these matters will be explored and a distinction between collisional and collisionless absorption processes is put into discussion.

2.1 Laser Absorption Processes

The typical way of studying the laser absorption processes is by investigating the *absorption coefficient*, the fraction of absorbed laser power by a structure. This can be done through collisional or non-

collisional effects, i.e., it can depend on the particle-to-particle interaction. In this section an overview of the main absorption means that can take place in both regimes is given.

2.1.1 Collisional absorption

Helmholtz equations

The Helmholtz equations for electromagnetic wave propagation in an inhomogeneous plasma are one of the most well known and comprehensive treatments of this topic. Starting from the Lorentz equation of motion for the electrons including the collisional damping, the following can be written:

$$m\frac{\partial \mathbf{v}}{\partial t} = -e\Big(\mathbf{E} + \frac{\mathbf{v}}{c} \times \mathbf{B}\Big) - m\nu_{ei}\mathbf{v} \tag{2.1}$$

where ν_{ei} is the electron-ion frequency defined by:

$$\nu_{ei} = \frac{4}{3}\sqrt{2\pi}\frac{n_e Z^* e^4}{m^2 v_{te}^3}\ln\Lambda \simeq 2.91 \times 10^{-6} Z^* n_e T_e^{-3/2}\ln\Lambda \;\; s^{-1} \tag{2.2}$$

also known as the *Spitzer* collision formula. Z^* is the number of free electrons per atom, n_e is the electron density in cm^{-3}, T_e is the electron temperature in eV and $\ln\Lambda$ is the Coulomb logarithm. By definition, $\ln\Lambda = \ln\left(\frac{b_{max}}{b_{min}}\right)$, where b_{max} and b_{min} are the maximum and minimum impact parameters for Coulomb collisions, respectively.

The relevant EM wave equations for $\mathbf{E}$ and $\mathbf{B}$ are:

$$\nabla^2\mathbf{E} - \frac{1}{c^2}\frac{\partial^2\mathbf{E}}{\partial t^2} = \frac{4\pi}{c^2}\frac{\partial \mathbf{J}}{\partial t} + \nabla(\nabla\cdot\mathbf{E}) \tag{2.3a}$$

$$\nabla^2\mathbf{B} - \frac{1}{c^2}\frac{\partial^2\mathbf{B}}{\partial t^2} = -\frac{4\pi}{c}\nabla\times\mathbf{J} \tag{2.3b}$$

One can assume all field and fluid dynamics to have harmonic time behaviour. Formally this is achieved by making an expansion $f(\mathbf{x},t) = f_0(\mathbf{x}) + f_1(\mathbf{x})e^{-i\omega t} + f_2(\mathbf{x})e^{-2i\omega t} + ...$

From this and under the simplifications done by Gibbon [11], one can write the following:

$$\frac{\partial}{\partial t} \rightarrow -i\omega \tag{2.4a}$$

$$n_e \rightarrow n_0 + n_1 \tag{2.4b}$$

$$\mathbf{J} \rightarrow -en_0\mathbf{v}_1 \tag{2.4c}$$

$$(\mathbf{E} + \mathbf{v}\times\mathbf{B}) \rightarrow \mathbf{E}_1 \tag{2.4d}$$

From the Lorentz equations and solving for $\mathbf{v}_1$:

$$\mathbf{v}_1 = \frac{-i}{\omega + i\nu_{ei}}\frac{e\mathbf{E}_1}{m} \tag{2.5}$$

By substituting $\mathbf{v_1}$ for the expression of $\mathbf{J}$, equation 2.6 for $\mathbf{E}_1$ can be written as follows:

$$\nabla^2 \mathbf{E}_1 + \frac{\omega^2}{c^2}\mathbf{E}_1 = \frac{\omega\omega_p^2}{c^2}\frac{\mathbf{E}_1}{\omega + i\nu_{ei}} + \nabla(\nabla \cdot \mathbf{E}_1) \tag{2.6}$$

For a planar, electromagnetic wave propagating in a uniform plasma, $\nabla \rightarrow i\mathbf{k}$, and $\mathbf{E}_1 \perp \mathbf{k}$, meaning that $\nabla \cdot \mathbf{E}_1 = 0$. In this case the formula for the dispersion relation becomes the following:

$$k^2 = \frac{\omega^2}{c^2}\left[1 - \frac{\omega_p^2}{\omega(\omega + i\nu_{ei})}\right] \tag{2.7}$$

which provides a dielectric constant of the propagation medium of

$$\varepsilon \equiv \frac{k^2 c^2}{w^2} = 1 - \frac{\omega_p^2}{\omega(\omega + i\nu_{ei})} \tag{2.8}$$

In the interaction region where collisional absorption happens, there will be an underdense region, so $\nu_{ei}/\omega \leq 1$ can thus be assumed in order to write the Taylor expansion:

$$k \simeq \pm\frac{\omega}{c}\left(1 - \frac{\omega_p^2}{\omega^2}\right)^{1/2}\left(1 + i\frac{\nu_{ei}}{2\omega}\frac{\omega_p^2}{\omega^2}\frac{1}{1 - \omega_p^2/\omega^2}\right) \tag{2.9}$$

The wavevector expression above displays a damping behaviour. Since the intensity of a light wave is proportional to the square of the electric field, by definition, the absorption coefficient η is given by twice the imaginary part of k:

$$\eta = \frac{\nu_{ei}}{c}\frac{\omega_p^2}{\omega^2}\left(1 - \frac{\omega_p^2}{\omega^2}\right)^{-1/2} \tag{2.10}$$

Due to the damping by the collisional absorption, the laser intensity I changes while propagating in a plasma. If it propagates along the x direction, the evolution of I is given by:

$$\frac{dI}{dx} = -\eta(x)I \tag{2.11}$$

The problem is that for short timescales the absorption rate is not analytically computable and for certain values the theory vanishes. Nevertheless, this works well for slowly varying density gradients L over a laser wavelength, i.e., $L^{-1} \ll k$, and in this case the WKB approximation can be used. Considering a linear density profile $n_e = n_c(1 + x/l), -\infty \leq x \leq 0$ and by using $\omega_p^2/\omega^2 = n_e/n_c$ and $\nu_{ei} \propto n_e$ (n_c being the critical density), the absorption coefficient can be rewritten as

$$\eta = \left[\frac{\nu_{ei}(n_c)}{c}\right]\left(\frac{n_e}{n_c}\right)\left(1 - \frac{n_e}{n_c}\right)^{-1/2} \tag{2.12}$$

From eq. 2.11, and knowing that the absorption rate $A = \dfrac{I_{in} - I_{out}}{I_{in}}$, the final result is thus:

$$A = 1 - \exp\left(-2\int_{-\infty}^{0}\eta\, dx\right) = 1 - \exp\left[-\frac{8}{3}\frac{\nu_{ei}(n_c)l}{c}\right] \tag{2.13}$$

which is similar to the formula from Kruer, 1988 in this same limit for s-polarized light, apart from an

angular dependence:

$$\eta_{Kruer} = 1 - \exp\left[-\frac{8}{3}\frac{\nu_{ei}(n_c)l}{c}\cos^3(\theta)\right] \tag{2.14}$$

This slightly different result arises from the *ansatz* of oblique-incidence, which was not considered in the previous calculations.

Normal skin effect (NSE)

In the limit $L \to 0$, there should be a perfect density step and Fresnel-like absorption behaviour of metal-optics is recovered. This is the ideal case for short-pulse laser-solid interactions, therefore it is worth checking the solutions of Helmholtz equations in this circumstance.

Considering s-polarized light, and starting from the $\mathbf{E}$ field equation (eq 2.6), the density is now written as a Heaviside step function $n_0(x) = n_0\Theta(x)$. This way the dielectric function becomes:

$$\varepsilon(x) = 1 - \frac{\omega_p^2}{\omega^2}\Theta(x) \tag{2.15}$$

In the vacuum region (x< 0) the electric field has the solution

$$E = 2E_0 \sin(kx\cos(\theta) + \phi) \tag{2.16}$$

where $k = \omega/c$, E_0 is the amplitude of the laser field and ϕ a phase factor to be determined. In the overdense region, the field is evanescent:

$$E = E(0)\exp(-x/l_s) \tag{2.17}$$

where

$$l_s = \frac{c}{\omega_p}\left(1 - \frac{\omega^2}{\omega_p^2}\cos^2(\theta)\right)^{-1/2} \tag{2.18}$$

is the collisional skin-depth. In the highly overdense limit, $n_0/n_c \gg 1$, therefore $l_s \simeq c/\omega_p$. By matching the boundary conditions from both regions, the values for $E(0)$ and ϕ are thus:

$$E(0) = 2E_0\frac{\omega}{\omega_p}\cos(\theta) \tag{2.19a}$$

$$\phi = \arctan\Big(-l_s\frac{\omega}{c}\cos(\theta)\Big) \tag{2.19b}$$

The electron-ion collisions will give a metal-surface with finite conductivity behaviour to the plasma. The result for the reflectivity under such conditions, for s-light and p-light is, from [20],

$$R_s = \left|\frac{\sin(\theta - \theta_t)}{\sin(\theta + \theta_t)}\right| \tag{2.20a}$$

$$R_p = \left| \frac{\tan(\theta - \theta_t)}{\tan(\theta + \theta_t)} \right| \tag{2.20b}$$

where θ is the angle of incidence and $\theta_t = \arcsin(\sin\theta/\sqrt{\varepsilon})$ is the generalized complex angle of the transmitted light rays from Snell's law.

The scaling of the absorption coefficient can be obtained analytically in some particular cases. The electric permittivity and refractive index can be split into real and imaginary parts: $\varepsilon = \varepsilon_r + i\varepsilon_i$, $n = n_r + in_i$. Since $\varepsilon = n^2$, and by making the substitutions: $\tilde{\nu} = \frac{\nu_{ei}}{\omega}$ and $\tilde{\omega_p} = \frac{\omega_p}{\omega}$, leads to:

$$\varepsilon_r = 1 - \frac{\tilde{\omega_p}^2}{(1+\tilde{\nu}^2)} = n_r^2 - n_i^2 \tag{2.21a}$$

$$\varepsilon_i = \frac{\tilde{\nu}\tilde{\omega_p}^2}{1+\tilde{\nu}^2} = 2n_r n_i \tag{2.21b}$$

Normal incidence, $\theta \to 0$, makes:

$$R_s = R_p = \left| \frac{1-n}{1+n} \right|^2 \tag{2.22}$$

which provides an absorption coefficient of

$$\eta = 1 - R_s = \frac{4n_r}{(1+n_r)^2 + n_i^2} \tag{2.23}$$

The only thing left is to find n_r and n_i. There will be two distinct cases, which are the existence of low ($\tilde{\nu} \ll 1$) or strong ($\tilde{\nu} \gg 1$) damping. Assuming highly overdense plasma ($\omega_p \gg \omega$) for low damping, $n_i \approx \tilde{\nu}\frac{\tilde{\omega_p}^2}{2n_r}$, and therefore $n_r = \frac{\tilde{\nu}^2\tilde{\omega_p}^2}{2}$. For the strong damping regime, $n_r = n_i = \frac{\tilde{\omega_p}^2}{2\tilde{\nu}}$. By replacing these terms in equation 2.23, the absorption coefficient for the normal skin effect is:

$$\eta_{nse} = \begin{cases} \dfrac{2\nu_{ei}}{\omega_p} & \text{for} \quad \nu_{ei} << \omega_0 \\ \dfrac{2\nu_{ei}}{\omega_p}\sqrt{\omega_0/\nu_{ei}} & \text{for} \quad \nu_{ei} > \omega_0 \end{cases} \tag{2.24}$$

2.1.2 Collisionless absorption

Modest intensity experiments and hydrodynamic models were showing quite a good match, both in terms of measured reflectivity and plasma parameters [21], [22]. However, with the growth in terms of laser system development, soon became the theory and experimental results in disagreement between each other. Generally, for intensities above the order of 10^{15} W/cm^2, the plasma temperature rises sufficiently so that collisions are disregarded during the interaction. New ways for laser energy deposition that don't rely on particle collision must be unveiled.

Vacuum heating - Brunel mechanism

The interaction process is different when a p-polarized laser pulse is incident obliquely on the target such that the electric field can pull electrons out of the steep plasmas. Consider a resonantly driven plasma

wave at the critical density with field amplitude E_p. In a sharp-edged profile, where little field swelling will happen, $E_p \sim E_L$ (E_L the incident laser electric field). Electrons will undergo oscillations with amplitude $A \sim \frac{eE_L}{m_e\omega^2} \gg L$. The oscillating electron driven by the laser electric field will bring away and convert the energy of the laser pulse to the kinetic energy of the plasma when they penetrate into the over-dense plasma. Such an absorption process was first described by Brunel as the vacuum heating [23].

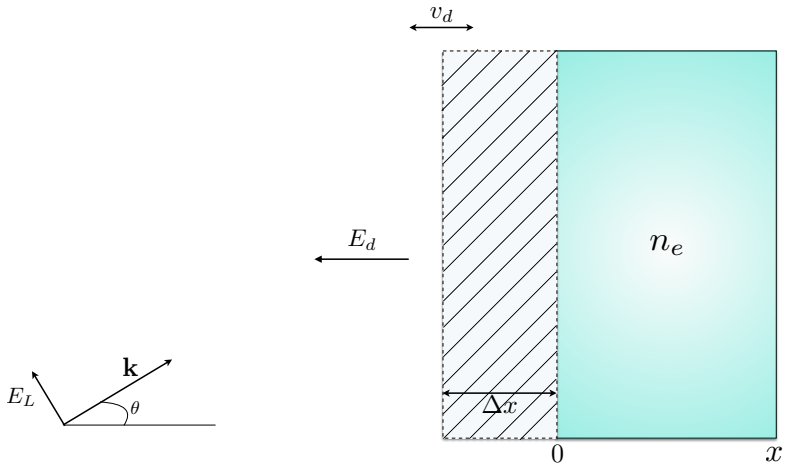

Figure 2.1: Capacitor model of the Brunel heating mechanism (adapted from [11])

Brunel explained this model using the *capacitor approximation* (fig. 2.1). The magnetic field of the wave is ignored ($\mathbf{v}\times\mathbf{B} = \vec{0}$) and the laser field E_L has a normal component E_d to the target surface.If the incidence is angular, the driving electric field is written as $E_d = 2E_L \sin\theta$. This field pulls an electronic slab out to a distance Δx from the origin. The surface density number of this slab is $\sigma = n_e\Delta x$, meaning the electric field created is $\Delta E = 4\pi e\sigma$. Since $\Delta E \equiv E_d$, the surface density is thus:

$$\sigma = \frac{2E_L \sin\theta}{4\pi e} \tag{2.25}$$

As the electrons return to the initial position, they will acquire a velocity of $v_d = 2v_{os}\sin\theta$, where $v_{os} = \frac{eE_0}{m\omega}$ is the usual *quiver velocity* in a laser field.

The average energy density absorbed per laser cycle is given by:

$$P_a = \frac{\sigma}{\tau}\frac{mv_d^2}{2} \simeq \frac{1}{16\pi^2}\frac{e}{m\omega}E_d^3 \tag{2.26}$$

Knowing that the incoming laser power is $P_L = \frac{cE_L^2}{8\pi}\cos\theta$ and using the formula for E_d, the fractional absorption rate is then given by:

$$\eta_a = \frac{P_a}{P_L} = \frac{4\sin^3\theta}{\pi\cos\theta}a_0 \tag{2.27}$$

where $a_0 = \frac{v_{os}}{c}$.

This absorption rate predicts therefore more absorption at large angles for incidence and higher laser irradiance. Besides, this expression predicts 100% absorption if both these parameters are large enough. Two corrections can be done to improve the model.

First, E_d is written as a function of the absorption rate, i.e., the surface is considered to have imperfect reflectivity:

$$E_d = [1 + (1 - \eta_a)^{1/2}]E_L \sin\theta = fE_L \sin\theta \tag{2.28}$$

where $f = 1+(1-\eta_a)^{1/2}$ is the field amplification factor. Second, assuming the return velocities of the electrons to be relativistic at bigger intensities, their kinetic energy can be replaced with $U_k = (\gamma-1)mc^2$ in the absorbed power expression, with $\gamma = (1 + v_d^2/c^2)^{1/2}$. This leads to the implicit expression,

$$\eta_B = \frac{f}{\pi a_0}[(1 + f^2 a_0^2 \sin^2\theta)^{1/2} - 1]\frac{\sin\theta}{\cos\theta} \tag{2.29}$$

This formula reproduces Brunel's original formula.

Now, it is possible to make a distinction between low-intensity ($a_0 \ll 1$) and high-intensity ($a_0 \gg 1$) regimes. The low-intensity case shows a coefficient of the form:

$$\eta_{VH}^{L} = \frac{a_0}{2\pi}\frac{f^3 \sin^3\theta}{\cos\theta} \tag{2.30}$$

In the strong relativistic limit ($f a_0 \sin\theta \gg 1$),

$$\eta_{VH}^{H} = \frac{f^2}{\pi}\frac{\sin^2\theta}{\cos\theta} \tag{2.31}$$

Anomalous skin effect (ASE)

Similar to Brunel mechanism is the process of *anomalous skin effect*. It is a well-known effect in solid state physics [24] and was firstly studied by Weibel in the context of step-like vacuum plasma interfaces.

Electrons within the skin depth $l_s = \dfrac{c}{\omega_p}$ oscillate in the laser field and dissipate energy with collisions with ions (inverse-bremmstrahlung). Technically this is the Fresnel limit, considered earlier in subsection 2.1.1. The oscillation energy is thus locally thermalized provided that the electron mean-free-path, $\lambda_{mfp} = v_{te}/\nu_{ei}$ is smaller than l_s.

Supposing that the temperature increased leading to $\lambda_{mfp} > l_s$, making the mean thermal excursion length $v_{te}/\omega > l_s$. In such conditions the relationship between the induced current and the electric field becomes *nonlocal*, therefore the effective collision frequency is now given by the excursion time in this enlarged layer l_a, i.e., $\nu_{\text{eff}} = v_{te}/l_a$. This value of l_a is [25]:

$$l_a \simeq \left(\frac{c^2 v_{te}}{\omega\omega_p^2}\right). \tag{2.32}$$

l_a can have a different expression from the kinetic theory, where nonlocal nature of electron current is taken into account self-consistently by integrating the velocity distribution function. This 'quasi-linear' analysis is mathematically written as [26]:

$$\frac{1}{l_a^3} = \frac{2\pi^2\omega_p^2\omega}{c^2}\int_0^\infty v f_0(v) dv \tag{2.33}$$

where $f_0(v) = \frac{1}{(2\pi v_{te}^2)^{3/2}} \exp(-v^2/2v_{te}^2)$ is taken as a Maxwellian term in an expansion of the slowly varying part of the distribution function.

Therefore,

$$l_a = \left(\frac{2}{\pi}\right)^{1/6} \left(\frac{c^2 v_{te}}{\omega \omega_p^2}\right)^{1/3} \tag{2.34}$$

and so the corresponding absorption rate is [26]:

$$\eta_{ase} = \frac{8\omega l_a}{3\sqrt{3}c} \simeq \left(\frac{T_e}{511\ keV}\right)^{1/6} \left(\frac{n_c}{n_e}\right)^{1/3} \tag{2.35}$$

Resonance absorption

When an electromagnetic wave is obliquely incident on an inhomogeneous plasma and polarized in the plane of incidence, it is well known that it can be absorbed resonantly by linear mode conversion into an electron plasma wave. This process, known as resonant absorption, has some implications for laser target experiments and microwave laboratory experiments.

For long density scale-lengths ($kL \gg 1$), the absorption fraction is said to have a self-similar dependence on the parameter $\xi = (kL)^{1/3} \sin\theta$, where θ is the incidence angle (Denisov, 1957; Ginzburg, 1964). In this limit the angular absorption behaviour is given by the curve $\phi(\xi)$ (eq. 2.36).

$$\Phi(\xi) \sim 2.3\xi \exp(-2\xi^3/3) \tag{2.36}$$

To a good approximation, the fractional absorption (fig. 2.2) is given by:

$$\eta_{ra} = \frac{\Phi^2(\xi)}{2} \tag{2.37}$$

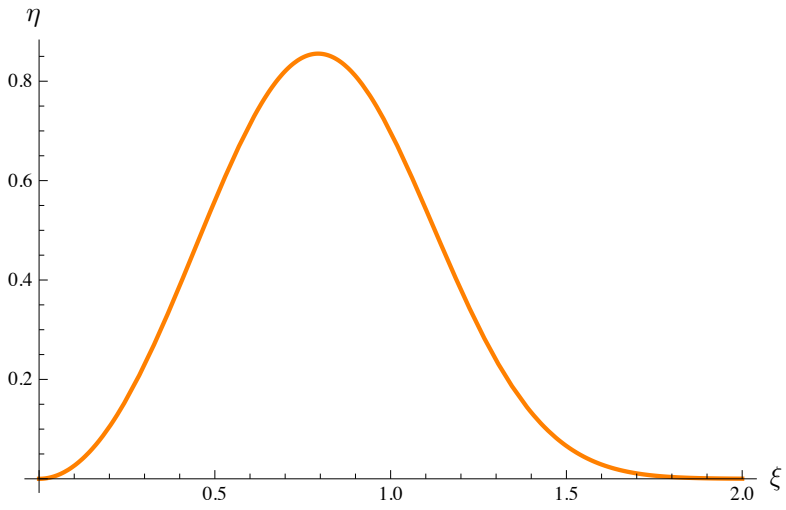

Figure 2.2: Resonance absorption graph

2.2 Solid heating, thermal conduction and expansion

The absorption of laser energy will result in the heating of the target material, meaning that heating and light absorption are intimately related and should be treated self-consistently.

In the absence of hydrodynamic motion, the problem is reduced to a transport problem: propagation of a non-linear heat-wave into a cold, conducting, semi-infinite medium with a continuous heat source at one boundary. There are several approaches, here three of these possibilities are provided.

2.2.1 Two-Temperature Model - TTM

The two-temperature model is widely used for the calculation of the electron and phonon temperatures after interaction with ultrashort laser pulses, being therefore implemented in metal dynamics [27], [28], [29]. Here, the *ansatz* for the configuration of a metal is a vibrational structure sustained by the coupling of vibrational *quanta* - phonons - and electrons which both form lattices that are coupled with each other. By solving two coupled differential equations for the electron and phonon temperatures, the ultrafast dynamics of the interaction is modelled.

In its present form it was first introduced by Anisimov et al. [30], although the main idea to a description of two different temperature subsystems was initially coined by Kaganov et al. [31]. The problem can be reduced to a 1-D problem as long as the diameter of the focus spot is much broader than the skin depth. The TTM equation system is written in the following way:

$$\mathcal{C}_e(T_e)\frac{\partial T_e}{\partial t} - \frac{\partial}{\partial x}\Big(\lambda_e(T_e)\frac{\partial T_e}{\partial x}\Big) = S(x,t) - h_{ex}(T_e - T_{ph}) \tag{2.38a}$$

$$\mathcal{C}_{ph}(T_{ph})\frac{\partial T_{ph}}{\partial t} = h_{ex}(T_e - T_{ph}) \tag{2.38b}$$

This is a non-linear, inhomogeneous system of coupled differential equations for the electron (T_e) and phonon (T_{ph}) temperatures, where $\mathcal{C}$ is the heat capacity, λ_e is the electronic thermal conductivity as a function of the electron temperature, $S(x,t)$ is the laser source term and h_{ex} is the heat exchange coefficient. The neglect of phonon diffusion in the 2nd equation is due to the smallness of the phonon temperature gradient compared to the one for the electrons and to the big difference of thermal conductivity between both species. The source term can be written as,

$$S(x,t) = (1-R)\alpha e^{-\alpha x} I_0 g_L(x,t) \tag{2.39}$$

where R is the reflectivity, α the absorption coefficient, I_0 the maximum of the laser intensity and $g_L(x,t)$ a function describing the spatial and time dependence of the laser pulse.

The interesting quantity in 2.38 is h_{ex}, which can be defined mathematically by:

$$h_{ex} = \frac{3\hbar}{\pi k_B}\langle\Omega^2\rangle\Lambda_{e-ph}\gamma_e \tag{2.40}$$

Here, apart from $\hbar$ being the reduced Planck constant and k_B the Boltzmann constant, $\langle\Omega^2\rangle$ is taken as the mean square of phonon frequencies, Λ_{e-ph} the electron-phonon coupling constant and γ_e the

coefficient of electronic specific heat. Important to mark is that the heat capacity of the phonons can be taken as constant, unlike in the case for the electrons, whose heat capacity is here considered as varying linearly with temperature - $\mathcal{C}_e = \gamma_e T_e$ -, a thermodynamic approximation with no atomic physics involved. In table 2.1 are values for selected metals. Notice that the product $\langle\Omega^2\rangle\Lambda_{e-ph}$ is an important term in superconductivity theory [32].

Metal	$\gamma_e \cdot 10^{-5}$ (J cm^{-3} K^{-2})	$\langle\Omega^2\rangle$ (meV^2)	Λ_{e-ph}	h_{ex} (GW cm^{-3} K^{-1})	$\tau_e(T = 300K)$ (fs)	λ_e (W cm^{-1} K^{-1})	$\alpha \cdot 10^5$ (K^{-1})
Au	6.7	178	0.15	26	773	3.1	7.31
Ag	6.5	344	0.12	35	557	4.18	8.56
Cu	9.7	377	0.1	94	310	3.85	7.60
Al	12.7	-	0.43	380	100	2.38	11.00
Nb	71.7	275	1.04	3888	55	0.52	4.78
Pb	16.0	31	1.55	122	366	0.38	6.66
Ti	8.5	601	0.54	1207	21	0.22	6.30
V	117.7	352	0.82	5571	63	0.31	5.10
W	13.7	425	0.26	259	159	1.74	4.34

Table 2.1: Metal coefficients for electronic specific heat, mean square of phonon frequencies, electron-phonon coupling constant, heat exchange coefficient, temperature relaxation time, thermal conductivity and absorption coefficient (from [33], [34] and [35]).

The boundary conditions have to be specified as well. The spatial interval where the equation needs to be solved is $0 < x < L$, with L being the thickness of the foil, while the time interval needs to be longer than the laser pulse duration τ_p ($t \gg \tau_p$).

2.2.2 Alternative approaches

For its wide use in femtosecond pulse science and for its consistency, the TTM will be the reference which will be taken into account for comparison with the OSIRIS results. Some other alternative analyses are here left as an extra, which won't be implemented for the cross checking with the results.

Temperature scaling in a plasma

Another treatment of the heat transport law to retrieve a temperature scaling as a function of plasma and laser parameters can be taken. Unlike in the case in the TTM and ETTM, this scaling includes no lattice structure. Instead, an approach considering only a collective ion-electron ensemble can be made.

The starting point is done by writing the heat equation as:

$$\frac{\partial \epsilon}{\partial t} + \nabla \cdot (\mathbf{q} + \mathbf{\Phi}_a) = 0 \tag{2.41}$$

where, ϵ is the energy density, $\mathbf{q}$ the heat flow and $\mathbf{\Phi} = \eta_a \mathbf{\Phi_L}$ the absorbed laser flux.

The simplest model possible applied for femtosecond pulses is *volume heating*. If the penetration depth of the heat wave is less than the skin depth $l_s = \frac{c}{\omega_p}$, thermal transport is neglected. Writing $\epsilon = \frac{3}{2} n_e k_B T_e$ and $\nabla \cdot \Phi_a \sim \frac{\Phi_a}{l_s}$, leads to the relation:

$$\frac{dT_e}{dt} \simeq \frac{\Phi_a}{n_e l_s} \tag{2.42}$$

which can be written in the form of the heating rate

$$\frac{d}{dt}(k_B T_e) \simeq 4\frac{\Phi_a}{W/cm^2}\left(\frac{n_e}{cm^{-3}}\right)^{-1}\left(\frac{l_s}{cm}\right)^{-1} \text{keV/fs} \tag{2.43}$$

This equation gives the initial heating rate near the surface of a solid-density plasma. After some femtoseconds, thermal transport must be considered due to huge temperature gradients generated and the formula loses its validity.

For the ideal plasma case, $q(x) = -\lambda_e \frac{\partial T_e}{\partial x}$, which is the usual Spitzer-Härm heat flow [36]. λ_e is the electron thermal conductivity as before, being defined as:

$$\lambda_e = 32\left(\frac{2}{\pi}\right)^{1/2}\frac{n_e}{\nu_0 m^{5/2}}T_e^{5/2} \tag{2.44}$$

where

$$\nu_0 = \frac{2\pi n_e Z e^4 \ln\Lambda}{m^2} \tag{2.45}$$

Substituting in the heat equation for ϵ and q, and making again the assumption of 1-D heat diffusion like in the previous sub-sections, one can write

$$\frac{3}{2}n_e k_B \frac{\partial T_e}{\partial t} = \frac{\partial}{\partial x}\left(\lambda_e \frac{\partial T_e}{\partial x}\right) + \frac{\partial \Phi_L}{\partial x} \tag{2.46}$$

This equation has a self-similar solution (by self-similar one means that the shape of the heatwave remains the same while hitting the target). The analytical solution for this problem is given by Rozmus and Tikhonchuk [26], which stated that the boundary condition for the heat flow must be equal to the incoming laser flux ($q|_{x=0} = \eta_a I_0$). Using mathematical techniques from Zel'dovich and Raizer [37], the surface temperature scaling of Rozmus and Tikhonchuk is computed as:

$$T_e(0) = 119\left(\frac{n_e}{10^{23}cm^{-3}}\right)^{1/12} Z^{1/12}\left(\frac{I_a}{10^{15}W/cm^2}\right)^{1/3}\left(\frac{t_p}{100fs}\right)^{1/6} \text{eV} \tag{2.47}$$

A similar expression was obtained by Rosen [38] using physical arguments based on classical heat-flow and constant absorption:

$$T_e(0) = 250\left(\frac{n_e}{10^{23}cm^{-3}}\right)^{-2/9} Z^{2/9}\left(\frac{I_a}{10^{15}W/cm^2}\right)^{4/9}\left(\frac{t_p}{100fs}\right)^{2/9} \text{eV} \tag{2.48}$$

which has a bigger intensity and pulse duration dependence than in the previous formula. Rosen treated the heated plasma layer as a black-body radiator, applying this result to estimate the soft x-ray yield from femtosecond laser-produced plasmas.

Extended Two-Temperature Model - ETTM

During his work on heat conduction and thermodynamics, Fourier obtained the famous heat conduction equation:

$$\mathbf{q} = -\lambda \nabla T \tag{2.49}$$

where $\mathbf{q}$ is the local heat flux density, λ is the thermal conductivity and ∇T is the temperature gradient. The thermal conductivity can vary with temperature, although the variation is usually small over a significant range of temperatures for some common materials, meaning it is sometimes considered a constant.

However, Maxwell later on derived a similar formula with an additional term:

$$\tau \frac{\partial \mathbf{q}}{\partial t} + \mathbf{q} = -\lambda \nabla T \tag{2.50}$$

He stated that the first term could be disregarded, with the argument that "the rate of conduction would rapidly establish itself". While for long time scales such statement is true, the same does not happen for femtosecond time scales. A modern derivation of this equation is given by the theory of extended thermodynamics [39]. Adding the energy conservation condition, one gets an equation system for the electrons alone:

$$\tau \frac{\partial \mathbf{q_e}}{\partial t} + \mathbf{q_e} = -\lambda_e(T_e) \nabla T_e \tag{2.51a}$$

$$\nabla \mathbf{q_e} + \frac{\partial u_e(T_e)}{\partial t} = S(x,t) - h_{ex}(T_e - T_{ph}) \tag{2.51b}$$

where the new term $u_e(T_e) = 0.5 \cdot \gamma_e T_e$ is the electron internal energy. The phonon equation is unmodified. After eliminating the heat flow in favour of the temperature, the electron and phonon temperature equation system becomes:

$$\tau \frac{\partial^2 u_e(T_e)}{\partial t^2} + \frac{\partial u_e(T_e)}{\partial t} - \frac{\partial \lambda_e(T_e)}{\partial x}\frac{\partial T_e}{\partial x} - \lambda_e(T_e)\frac{\partial^2 T_e}{\partial x^2} = \left(1 + \tau \frac{\partial}{\partial t}\right) S(x,t) - h_{ex}\left(1 + \tau \frac{\partial}{\partial t}\right)(T_e - T_{ph}) \tag{2.52a}$$

$$\mathcal{C}_{ph}(T_{ph}) \frac{\partial T_{ph}}{\partial t} = h_{ex}(T_e - T_{ph}) \tag{2.52b}$$

This is called the *Extended Two-temperature Model* (ETTM) [40],[41].

It is important to highlight that τ must be considered constant, otherwise the term $\nabla \tau \frac{\partial \mathbf{q}}{\partial t}$ would not vanish. In the limit $\tau \to 0$ the classical parabolic equation of heat conduction comes again.

2.2.3 Laser Induced Ablation

Many studies, either computational or experimental, involving the ablation of metallic structures interacting with lasers have been carried out intensively. Some of these, again, rely on the TTM in order to

investigate the dependence of the threshold fluence and melting depth on pulse duration. It is observed that for pulses shorter than approximately 1 ps, the threshold fluence and melting depth are independent of the pulse duration (fig. 2.2.3), while for pulses longer than $\sim$ 40 fs both increase proportionally to $\tau^{0.47}$ and $\tau^{0.51}$, respectively [27] in good agreement with approximate analytical expressions predicting a $\sqrt{\tau}$ dependence.

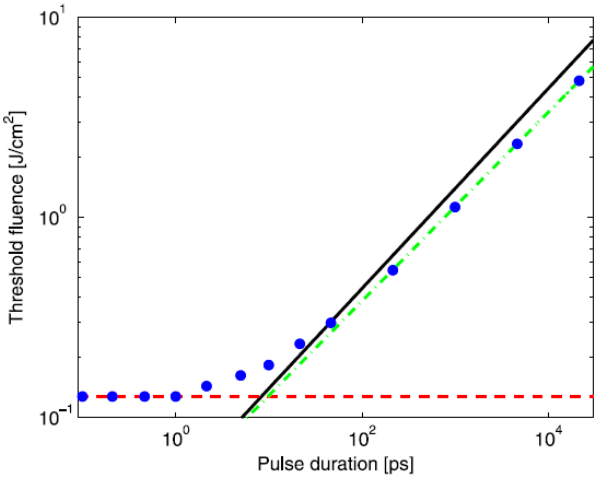

Figure 2.3: Threshold Fluence of Cu. Three regimes are seen: a constant value below 1 ps, a transition region, and then a power law at longer pulse durations. The red dashed line is a fit to the data points below 1 ps, and the green dash-dotted line a fit to the data $\geq$ 40 ps. The black solid line in represents eq. 2.53. (from [27])

From hydrodynamic analysis and some simplifications, this same law for the fluence can be written as:

$$F_{th,long}(\tau) = \frac{\pi T_{abl}}{2.1524(4\ln 2)^{1/4}}\sqrt{C\lambda\tau} \tag{2.53}$$

where T_{abl} is the ablation temperature, λ is the conductivity and C a constant proportional to the heat capacity.

Ultra-short laser pulses are suitable for micro- and nano-structuring of surfaces, but to affect the material as little as possible one must account to operate close to the threshold fluence, i.e., the minimum fluence at which ablation occurs. This threshold can be also identified through the ablation temperature which is determined by the *ablation criterion*. An assumption that can be made is that ablation takes place when the combined energy of electron and lattice systems exceeds the required energy for the material to undergo heating, melting and evaporation. Typically, the heating and melting energies are much smaller than the evaporation energy values. As heat propagation in the TTM model is neglected for the phonon case, the lattice only receives energy locally from the vibrating electrons. The maximum energy density at a certain point is therefore achieved when one reaches an exceeding limit for the lattice temperature, i.e., the case when there is a thermal balance between electrons and lattice. The ablation criterion can thus be written:

$$\mathcal{C}_{ph} \cdot T_{ph,max} + \int_{T_0}^{T_{ph,max}} \mathcal{C}_e(T_e)\, dT_e \geq \Delta H_v \tag{2.54}$$

where, $\mathcal{C}_e$ and $\mathcal{C}_{ph}$ are the heat capacity for electrons and lattice respectively, $T_{ph,max}$ is the maximum lattice temperature, T_0 is the initial temperature, T_e is the electron temperature and ΔH_v is the vaporization enthalpy.

From this equation the ablation temperature, T_{abl}, is then computed as the minimum value that the lattice temperature must reach to verify the inequality. The values are 9100 K, 8400 K and 20100 K for copper, silver and tungsten, respectively [27].

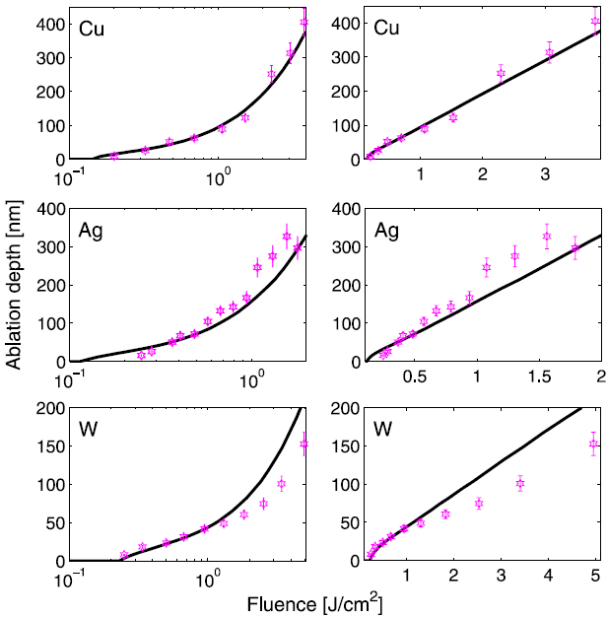

Figure 2.4: Depth of the ablated holes vs. the absorbed fluence for copper, silver and tungsten samples on logarithmic (left) and linear (right) fluence scale. The purple stars are the experimental points and the black solid line results of TTM simulations.

2.3 Nanoplasmonics

In subsection 1.2.1 the concept of *Nanoplasmonics* was explored. This fascinating study area has a wide set of physical applications as mentioned and is seen as a field with much more potential for future developments.

The application of a plasma code for the simulation of a metal slab interacting with an intense electromagnetic field makes diagnostics for nanoplasmonic effects mandatory for the accomplishment of this task.

In the following subsections, two of its main functionalities which have implications in the current work are presented: *Field Enhancement* and *Harmonic Generation*.

2.3.1 Field Enhancement

Strong laser beams, as highlighted before, make electrons oscillate when these are bound to protons in a metal, originating the exploitation of vibrating modes, the surface plasmons (SP), which are localized, collective oscillations of electron density and carry the oscillation energy.

There is a particular case of SP exploitation that is characterized by the generation of electric fields even more intense than the ones that gave the initial perturbation of the system, a concept which is known as *Field Enhancement*. This occurs when there is a collective motion of free electrons confined in narrowly localized regions of the metal, where they are highly concentrated.

When high power radiation hits a nano-structure, it excites an inhomogeneous distribution of SP surrounding its surface. But when they couple with a photon, the result is what's known as surface plasmon polariton (SPP) - electromagnetic waves that propagate at an interface between a plasmonic metal and a dielectric. Compared with the incident light, the SPPs can be much shorter in wavelength. These are responsible for a differential distribution of electric field enhancement.

Hotspots are the peaks of electric enhancement, most of which arise in sharp tips of the nano structures. The large enhancement of the local fields at a hotspot arises from the multiplication of the enhancement factors due to the SP resonance, the constructive interference of the fields from different SP's and the enhancement due to the morphology of the nanoparticle employed [2]. A typical configuration in Nanoplasmonics for such effect is the *gold bow-tie nano antenna* (fig. 2.5).

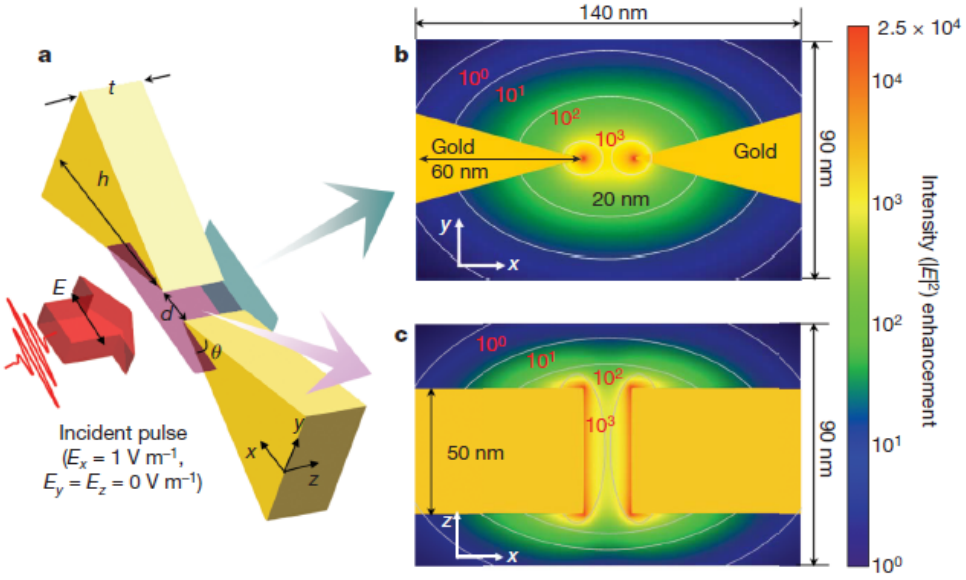

Figure 2.5: Finite-difference time-domain simulation of local field enhancement. a) Geometrical conditions for simulation of a single bow-tie element. The polarization direction of the incident pulse is parallel to the x–z plane. b) Intensity field computed in the x–y plane. c) Same simulation result viewed in the x–z plane. The design parameters selected were $h = 175$ nm, $d = 20$ nm, $t = 50$ nm and $\theta = 30^o$. The intensity enhancement factor, which reached a maximum of 2.5×10^4 at the apex of each triangle, turned out to be $> 10^2$ within the 60nm×350nm×350nm (x×y×z) volume in the gap. (from [3])

Gold is the preferable metal in field enhancement experiment, mainly because its thermal conductivity is very high, which allows the material to dissipate heat more efficiently, lowering its damage and

maintaining its stability for a longer interval of time.

The *lightning rod effect* is a hotspot case that happens when non-resonant SP lead to a high field amplification in sharp edges using a vertically polarized laser beam, as viewed in the bow-tie figure 2.5.

This is one of the main interests in Nanoplasmonics, the enhancement or amplification of light signals. The use of field enhancement can be extrapolated to the development of Optics, being the production of coherent XUV light through the generation of high-harmonics in a gas chamber (following section) one of the typical uses.

2.3.2 Harmonic Generation

In spite of having a linear behaviour in many events in nature, when dealing with stronger electric fields things become different. One of the most interesting phenomena with such characteristic is called *harmonic generation*. There are two main procedures for harmonic generation: low order and high order. In the next subsections a distinction between these two is made.

Low Order Harmonic Generation

Lasers with higher intensities create conditions on the target surfaces which changes the electronic structure and therefore some properties like refraction-index or reflectivity.

From classical electrodynamics, the electric displacement vector $\mathbf{D}$ equals $\mathbf{D} = \varepsilon_0\mathbf{E}+\mathbf{P}$, being $\mathbf{P}$ the polarization density. $\mathbf{P}$ is given in terms of a sum of matrix values χ_{ij} applied to the electric field, hence $P_i = \varepsilon_0 \sum_j \chi_{ij} E_j$. For low electric fields, $\mathbf{P} = \varepsilon_0\chi\mathbf{E}$, and the *electric susceptibility* term χ, in isotropic conditions, just a scalar.

This is the electric susceptibility by definition. But with strong electric fields it must be taken into account another effects, namely the non-linear dependence of the polarization density on the electric field, this means, in powers of the electric field:

$$P(t) = \varepsilon_0 \sum_n \chi^{(n)} E^n(t) = \varepsilon_0(\chi^{(1)}E + \chi^{(2)}E^2 + ...) \tag{2.55}$$

Here the term $\chi^{(n)}$ is the *n*-th order of susceptibility, and this is of main importance for electric fields of higher frequencies (than the driving field) to arise: *harmonic generation*. Notice that the units of $\chi^{(n)}$ vary with the value of n.

As a first insight, let's look at the *second harmonic generation* (SHG), related to the second order polarization density $P^{(2)}$ and with terms with twice the frequency of the original wave(s). If one considers a simple case with 2 monochromatic waves with frequencies ω_1 and ω_2, hence with a global electric field expression:

$$E(t) = Re\{E_1 e^{i\omega_1 t} + E_2 e^{i\omega_2 t}\} = \frac{1}{2}E_1 e^{i\omega_1 t} + \frac{1}{2}E_2 e^{i\omega_2 t} + c.c. \tag{2.56}$$

where *c.c* is the complex conjugate contributions for the monochromaticity. Therefore, the formula for the polarization density of 2nd order is:

$$P^{(2)}(t) = \frac{\varepsilon_0 \chi^{(2)}}{2}(|E_1|^2 + |E_2|^2) + \frac{\varepsilon_0 \chi^{(2)}}{4}(E_1^2 e^{i(2\omega_1)t} + E_2^2 e^{i(2\omega_2)t}) + \frac{\varepsilon_0 \chi^{(2)}}{2}(E_1 E_2 e^{i(\omega_1+\omega_2)t} + E_1^* E_2 e^{i(\omega_1-\omega_2)t}) + c.c \tag{2.57}$$

The first term in parenthesis is called *Optical Rectification* - *OR*. The second is the SHG, since there are terms with twice the original frequency. The remaining includes in first place the *Sum Frequency Generation* - *SFG* - and the *Difference Frequency Generation* - *DFG* -, since it involves, respectively, the sum and difference of both sources' frequencies. (fig. 2.6)

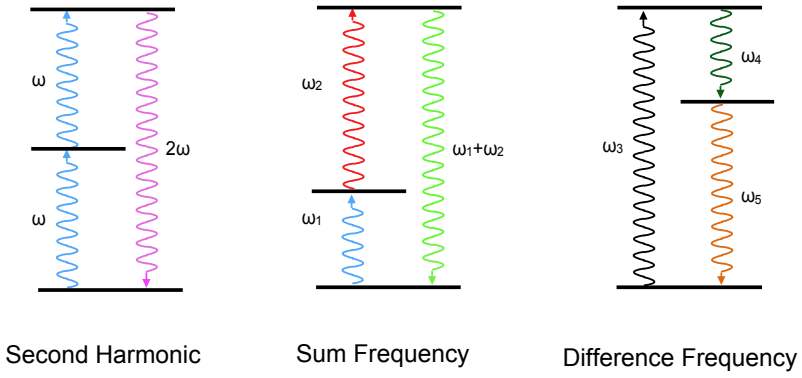

Figure 2.6: Illustration of the three cases - *SHG*, *SFG* and *DFG*.

Low harmonic generation occurs typically when laser pulses interact with crystalline structures.

High Harmonic Generation - HHG

When linearly polarized fields with much higher intensities are interacting with matter, field intensities are reachable in a way that they become comparable to the binding energy of the outermost electrons to the nucleus, which can therefore be ionized. These ionized electrons will start to oscillate in the laser field, gaining kinetic energy and recombining with the parent ion, leading to the emission of a high energy photon at XUV wavelengths. Such feature is in fact observed more accurately when using gas-phase elements (Argon is the conventional element).

This extreme effect - *high-harmonic generation* (HHG) - is one of the main sources of fully coherent ultraviolet light (XUV) and is the basis of the field of attosecond science [42]. The typical spectrum of HHG pulse has a rapid intensity decrease of low harmonics, followed by a long plateau and an abrupt cutoff (fig. 2.7).

An intuitive semiclassical model of HHG at the microscopic level was developed by Corkum [43] called 3-step model:

- 1st step: the electric field causes ionization of a valence electron by one of the 3 possibilities: multiphoton ionization, tunelling or over-the-barrier ionization.
- 2nd step: After ionization, the free electron is accelerated by the field.

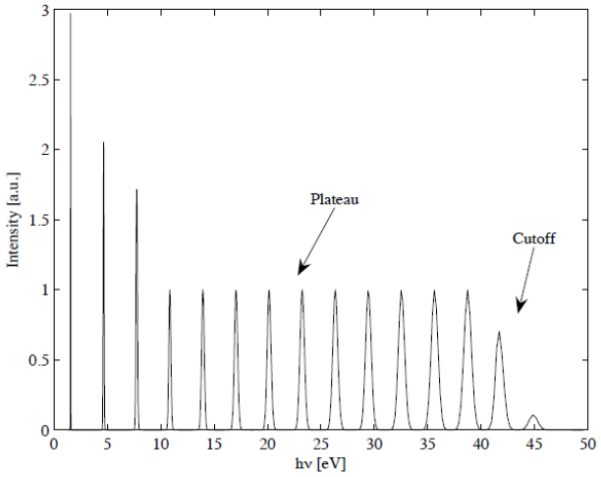

Figure 2.7: Spectrum of high-order harmonic pulse.[14]

- 3rd step: Since the field is oscillating, the electron has a probability of recombining with the parent ion. When that happens, there is the emission of a high-energy photon.

The question is whether there is HHG production while varying the intensity of the laser. A comparison between the non-relativistic ($< 10^{17}$ W/cm^2) and relativistic cases ($\geq 10^{17}$ W/cm^2) can be taken.

Having a wave linearly polarized in the x-direction, means that the vector potential is $\mathbf{A} = A_0 \cos(kz - \omega t)\mathbf{e}_x$. The Lorentz force for the electron is written as

$$\mathbf{F} = -e(\mathbf{E} + \mathbf{v} \times \mathbf{B}) \tag{2.58}$$

Regarding the fact that $\mathbf{E} = -\dfrac{\partial \mathbf{A}}{\partial t}$ and $\mathbf{B} = \nabla \times \mathbf{A}$, then

$$\mathbf{E} = -\omega A_0 \sin(kz - \omega t)\mathbf{e}_x \tag{2.59}$$

$$\mathbf{B} = -kA_0 \sin(kz - \omega t)\mathbf{e}_y \tag{2.60}$$

$$\mathbf{v} \times \mathbf{B} = v_z k A_0 \sin(kz - \omega t)\mathbf{e}_x - v_x k A_0 \sin(kz - \omega t\mathbf{e}_z \tag{2.61}$$

For the non-relativistic regime, writing every vector component of the force momentum, taking in mind the conditions

$$\mathbf{p}(t_0) = 0, \quad \mathbf{r}(t_0) = 0, \quad \frac{v_x}{c} << 1, \quad \frac{v_z}{c} << 1 \tag{2.62}$$

the following trajectories will arise:

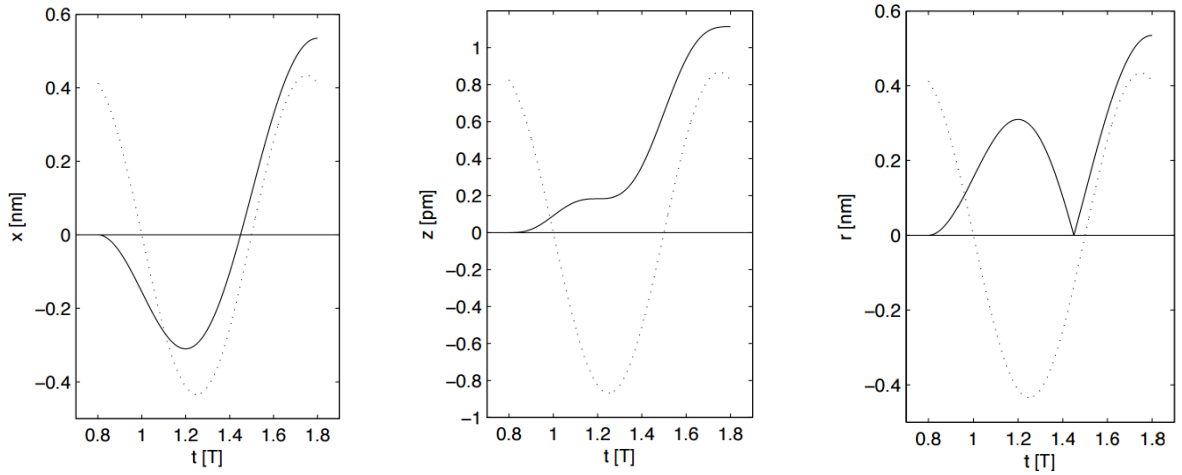

(a) Trajectory in x direction (b) Trajectory in z direction (c) Modulus of the full trajectory r

Figure 2.8: Electron trajectories of an electron in the 800 nm (T = 2.67 fs) for laser intensity of 10^{13} W/cm^2 and t_0=0.8 T. The dotted line is the electric field felt.(from [14])

When the intensities go above 10^{17} W/cm^2, relativistic effects take place and the atoms will overionize. Now that the speed on the different directions is closer to c, it cannot be repeated the same process as before with simplification of the system of equations. The system is solved numerically, leading to the following trajectories:

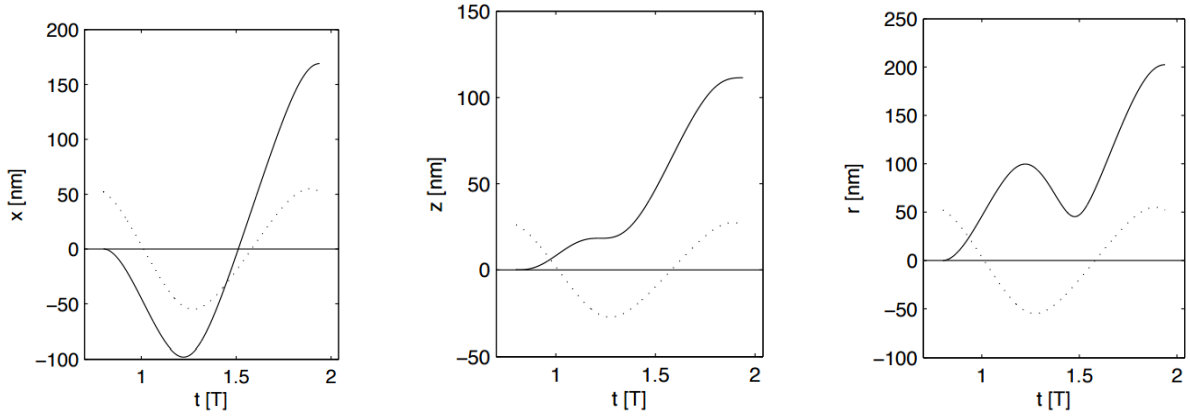

(a) Trajectory in x direction (b) Trajectory in z direction (c) Modulus of the full trajectory r

Figure 2.9: Electron trajectories of an electron in the 800 nm (T = 2.67 fs) for laser intensity of 10^{18} W/cm^2 and t_0=0.8 T. The dotted line is the electric field felt.(from[14])

The drift in z-direction is in this case more significant, making it less probable for electrons to recombine with ions as the field strength gets stronger. This proves the low efficiency of strong lasers to generate HHG.

The cutoff energy, predicted by Krause et al. [44] by the use of a numerical approach, can be written:

$$E_{cutoff} = I_p + 3.17U_p \tag{2.63}$$

I_p being the ionization potential of the bound electron and U_p the ponderomotive energy of the laser,

which satisfies $U_p \equiv \langle E_k \rangle = \frac{e^2 \mu_0}{8\pi^2 m_e c} I\lambda^2$.

This is the typical emission of harmonics from a gas driven by an intense femtosecond laser pulse, but the same can also take place in solids. While in gas-phase the harmonic generation there is a recombination of the loose electron with the parent ion (the 'hole' in solid language), in solids the mechanism is slightly different. From [42], the motion of electrons is tunnelled into the conduction band of the solid, generating a current-driven emission of photons. This is characteristic from solids unlike in gases, since electrons in vacuum always move synchronously with the laser field. As the electron oscillates coherently with the field, it returns information about the structure of the band in which it moves. Integer and non-integer harmonics generated in laser-ablated plasmas have been extensively studied since they yield useful diagnostic information on the properties of the plasma (density gradient, expansion velocity, etc.) near the critical surface [45], [46].

Kim et al. [3] managed to combine HHG with nanoplasmonics, to produce XUV. In their setup, a modest femtosecond oscillator - 100 kW peak power, 1.3 nJ pulse energy and 10 fs pulse duration - is directly focused onto nanostructures having a 10^{11} W/cm^2 intensity. The enhancement factor obtained (20 dB) was enough for the production of XUV, with wavelengths scaling down to $\sim$ 47 nm, phenomenon only observable with intensities bigger than 10^{13} W/cm^2. The setup for their experiment is given by figure 2.10.

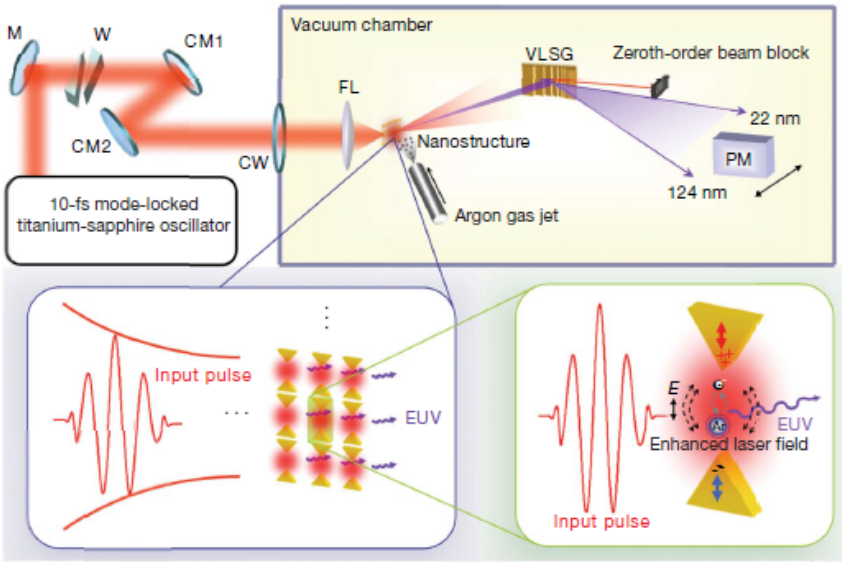

Figure 2.10: Apparatus for high-harmonic generation by electric field enhancement using a nanostructure of bow-tie elements. Anticlockwise from top: the overall system configured for the experiment, a detailed view of the two-dimensional array of bow-tie elements fabricated on a sapphire plate, and the magnified view of a single gold bow-tie element interacting with the incident pulse. Ar - argon atom; CM - chirped mirror; CW - chamber window; FL - focusing lens; M - mirror; PM - photon multiplier; VLSG - varied-line-spacing grating; W - wedge plate; E - electric field. (from [3])

Chapter 3

Experiment and Simulation

This work is not only performed to study the interaction of laser pulses with a metallic structure through the use of the computational tool OSIRIS but also to give support to the experiment taking place at the CEA, Saclay.

Though the computer power has gradually become more sophisticated, the simulation of an experiment of such complexity in a 100$\%$ realistic way is a demanding task. A typical PIC simulation is designed to work with charged particles, not being able to fully reproduce a low temperature solid when modelling on time-scales of sufficient length to experience non-trivial atomic motion. The evaluation of the classical Maxwell's equations and the Lorentz force for simple charges does not generate forces that maintain the structural rigidity of a solid, in this case a bound phonon-electron system. Instead, the atoms or ions disperse freely as if in gaseous form.

This work contemplates the simulation of the pumping of the target, and a further insight on the conditions for the probing of the target. For the first part the interest lies within the observation of either short-time scale effects such as field enhancement and peak electron temperatures, as well as events that endure for a long temporal window like target thermalization and expansion. The interest of the second part is a high harmonic probe source to study the diffraction pattern coming from the double slit target. With this study the imaging system for the experiment can be designed and recorded data interpreted.

3.1 Experiment - CEA

The 40 fs pulses of a Ti:Sapphire laser ($\lambda = 800$ nm) are split into two optical beam paths by a beam-splitter. The first beam path hits the target directly after being focused to a spot size of $\sim 2\,\mu m$. This one has an obliquely incident angle to the target. The second beam is directed into a cell where it generates harmonics, which will be sent perpendicularly to the foil. At the end, a CCD camera registers the diffracted image. Below is the setup of the experiment:

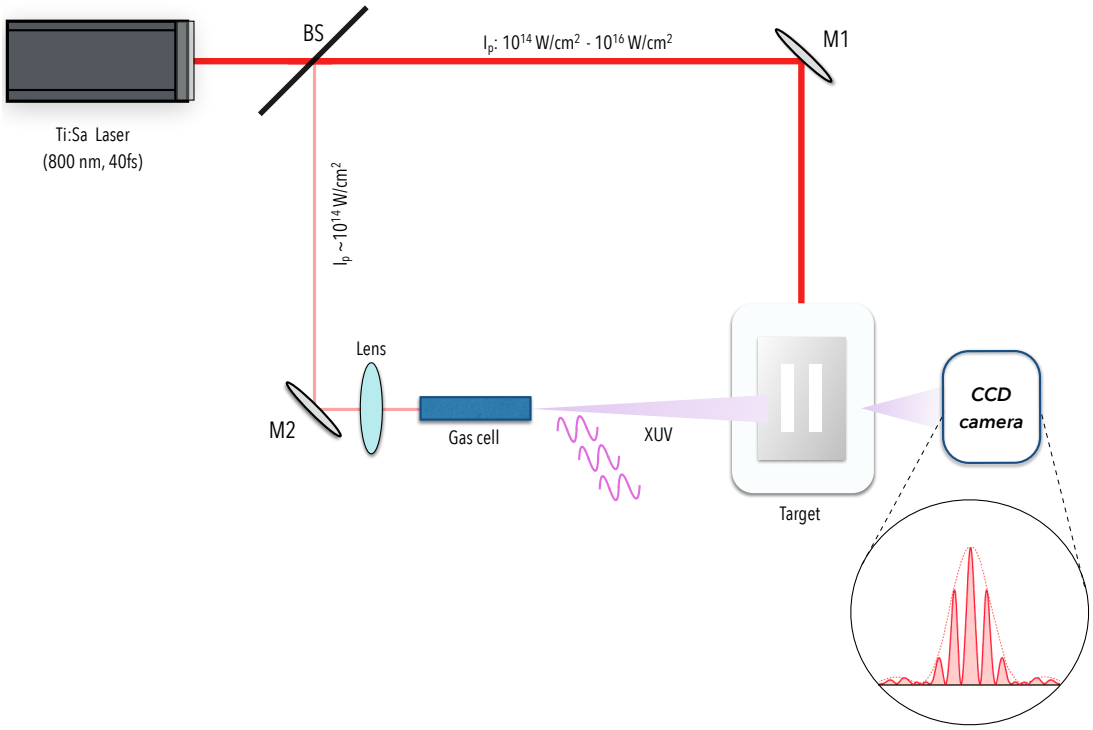

Figure 3.1: Lab setup for double slitted Titanium foil experiment (BS - Beam splitter; M - Mirror; XUV - extreme ultraviolet).

3.2 OSIRIS Simulation Parameters

The working principle of OSIRIS is discussed in detail in the introductory chapter. The following task is to design the whole simulation layout and for that OSIRIS requires determinate parameter values to specify the geometry, composition of the slitted foil and also the characteristics for the interacting laser fields.

3.2.1 Titanium plasma parameters

The first parameters to be computed are the plasma density and the electron plasma frequency of Titanium, since many of the quantities are normalized to this last quantity. The formulas for these are:

$$n_e = \frac{\rho N_A Z^*}{A_r} \tag{3.1a}$$

$$\omega_{pe} = \sqrt{\frac{e^2 n_e}{\varepsilon_0 m_e}} \tag{3.1b}$$

where ρ is the bulk density, N_A is the Avogadro number, Z^* is the ionization degree of the species, A_r the atomic mass, ε_0 the vacuum permittivity, e the electron charge and m_e the electron mass.

The bulk density and the atomic mass of Ti are given, unlike Z^* which depends on density and temperature. For such, the ionization level values are hence analysed for different temperatures (fig. 3.2).

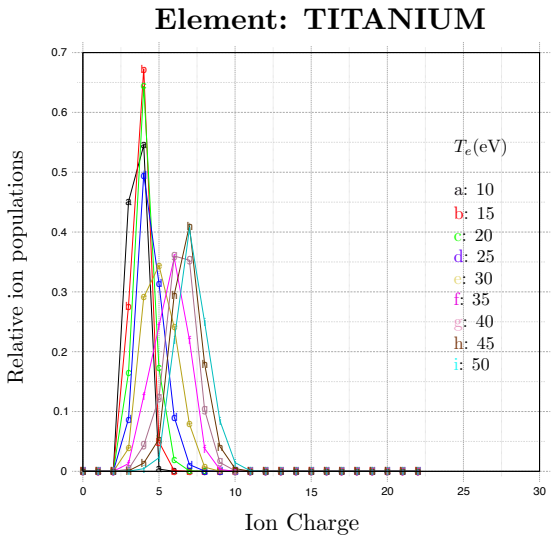

(a) Relative ion populations with specific charge value assuming local thermal equilibrium - different temperatures (adapted from [47])

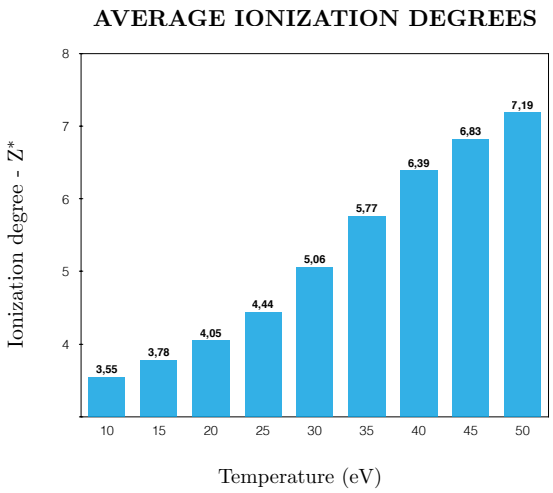

(b) Average ionization as a function of temperature

Figure 3.2: Ionization degree for Titanium

For the lowest temperature - 10 eV - the average ionization level is around 3.55, which is the value to be used in the simulations. Notice that an ionization level, say, for values between 2 and 8 (the limit values on the graph), does not change the plasma frequency value significantly and its magnitude remains with the same power, since it is multiplied by a factor between approximately 1 and 3. This way it becomes possible to compute the plasma frequency and consequently the reference length $\Delta x_{ref} = \frac{c}{\omega_{pe}}$ and reference time $\Delta t_{ref} = \frac{1}{\omega_{pe}}$.

A_r (g/mol)	ρ (g/cm^3)	Z^*	n_e(cm^{-3})	ω_{pe} (s^{-1})	Δx_{ref} (nm)	Δt_{ref} (fs)
47.867	4.506	3.55	2.01×10^{23}	2.56×10^{16}	11.74	0.03912

Table 3.1: Titanium plasma parameters

3.2.2 Titanium specie parameters

Titanium is a metallic element with 22 protons. The most stable isotope is $^{48}_{22}Ti$, a specie with 26 neutrons. To design a metal in OSIRIS, a system resembling an extremelly cold (room temperature) charged gas must be implemented. Since the neutrons have a mass approximately the same as the protons, the metal can be 'built' only from 2 species: electrons and protons. The '*rqm*' parameter in OSIRIS defines the reciprocal charge over mass ratio, meaning that for electrons rqm$_{el}$ = -1, while for protons rqm$_{prot} \simeq$ 1836.15. Since each Ti atom has 22 protons and 26 neutrons, this value needs to be multiplied by 48, therefore the second specie has rqm$_{Ti} \simeq$ 88135.

This will make the difference when defining the initial temperature of the whole system. The temperature is related to the thermal momentum, which is the (normalized) 'u_{th}' parameter in OSIRIS, and will be defined as a Maxwellian (classical) distribution, with a thermal speed associated to the room temperature ($\sim$ 300K).

u_{th} is equal to $\gamma_{th} \times v_{th}$, but for the employed temperature the value of the relativistic term γ_{th} is pretty much close to 1. Since the metal is in thermal equilibrium, both electron and proton species need to have both the same temperature. Provided that $v_{th} = \sqrt{\frac{T}{m}}$, T_0 = 300 K = 0.026 eV and that the value for the electron mass is m_e = 511 keV/c^2, substituting the values gives the normalized u_{th} for electrons. Using $m_i v_{th_i}^2 = m_e v_{th_e}^2 \Leftrightarrow v_{th_i} = v_{th_e} \sqrt{\frac{m_e}{m_i}}$ the same value for protons is computed (table 3.2).

T_0 (K)	rqm$_e$	rqm$_{Ti}$	u_{th_e}(norm)	u_{th_i} (norm)
300	-1	88135	2.25×10^{-4}	7.58×10^{-7}

Table 3.2: Thermal speed - electrons and protons

Typically below 10^{16} W/cm^2 collisional effects become dominant, but when higher intensities are reached collisionless absorption dominates. However, the collisions can still be present, even though in small proportion.

This comes into discussion since OSIRIS has a function that can include collisions within the system. It can work by 2 different ways: either a fixed value of $\ln \Lambda$ - Coulomb logarithm - is given, and this value remains fixed along the process, or OSIRIS iteratively computes the local $\ln \Lambda$ during the several time steps.

The problem for the first choice is that computing analytically the ion-electron collision frequency for a low temperature metal is a demanding task. So far only through experimental work became possible to determine this quantity. The experimentalists at the Max-Planck Institüt, for example, have made studies with low temperature metals, such as Aluminium. They interpolated the collision frequency function for different temperature regimes to determine the value for the cold Al (fig. 3.3). For cold Al the collision frequency is $\nu_{\text{Al}} = 8.5 \times 10^{14} s^{-1}$.

The problem for the second choice is that the ion-electron collision frequency in OSIRIS follows the Spitzer formula (eq. 2.2) which is not well behaved for low temperatures such as the ones from the target before the irradiation takes place. In the limit of a cold solid at temperatures below the Fermi temperature ($\sim$ 10 eV) the electrons are in a degenerate state. The collision frequency is no longer dependent on the electron temperature, but governed by the scattering of electrons by phonons or lattice vibrations.

The collision function will be, therefore, split in two ways.

For the density and temperature profiles, and since both are intimately associated, the best possible approach is by implementing an automatic Coulomb logarithm, as the temperatures involved during the majority of the simulation temporal window will reach values bigger than 1 eV for the various intensities, which are compatible with the Spitzer formula.

On the other hand, for the field enhancement analysis, since it is a phenomenon which takes place on a solid, or at least on a more rigid, cold structure, requires a target which remains the more intact as possible at an extremely low temperature, thus requiring a collision frequency for a cold target. The values for metals other than Al, in spite of some differences in terms of ionization levels, has a similar order of magnitude, meaning $\nu_{\text{cold metal}} \sim 10^{15}\, s^{-1}$. By returning to the Spitzer formula, the Coulomb logarithm value is thus $\ln \Lambda \simeq 0.2153$.

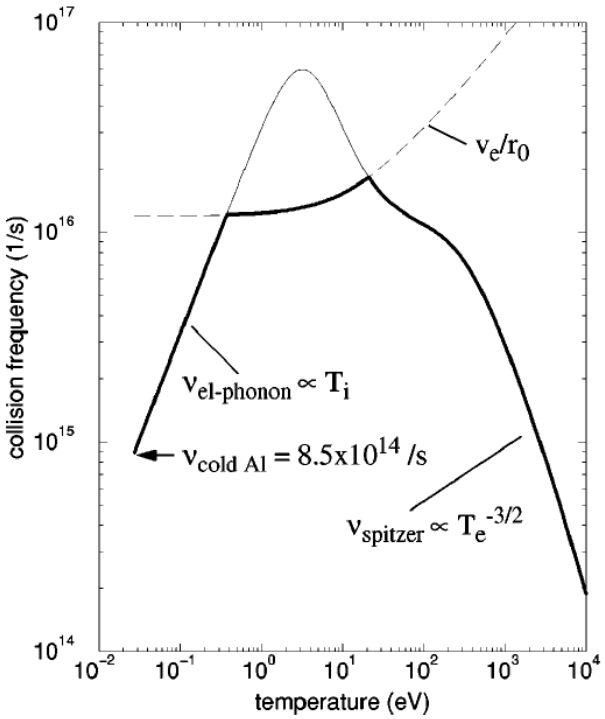

Figure 3.3: Collision frequency of solid Al as a function of the temperature $T_e = T_i$ (thick solid line). The thin solid line is the interpolation of $\nu^{-1} = \nu_{Spitzer}^{-1} + \nu_{el-phon}^{-1}$, the dashed line is the upper limit of the collision frequency given by the requirement $\lambda_e < r_0$. (from [48])

3.2.3 Foil geometry parameters

The foil is 100 nm thick, and has 2 slits with 300 nm width each and 600 nm away from each other. These lengths can be expressed in normalized units (n.u.) in respect to the parameter Δx_{ref} (fig. 3.4). The height of the foil and of the slits are not relevant since the simulations will be of 2D nature and the laser beam propagation will be on the x_1 direction as seen from a section cutting the slits.

3.2.4 Laser pump parameters

Finally it's important take a look on the laser beam parameters (table 3.3) and how they are expressed in normalized units and/or according to the OSIRIS tools.

Type	Pulse duration (fs)	Intensity (W/cm^2)	λ_{laser} (nm)	ω_{laser} (s^{-1})
Gaussian	40	10^{14} - 10^{16}	800	2.36×10^{16}

Table 3.3: Laser beam parameters

The OSIRIS laser pulse function does not work with intensities, wavelengths or frequencies directly. Instead, it uses 2 parameters for such: a_0 (normalized vector potential) and ω_0 (normalized frequency).

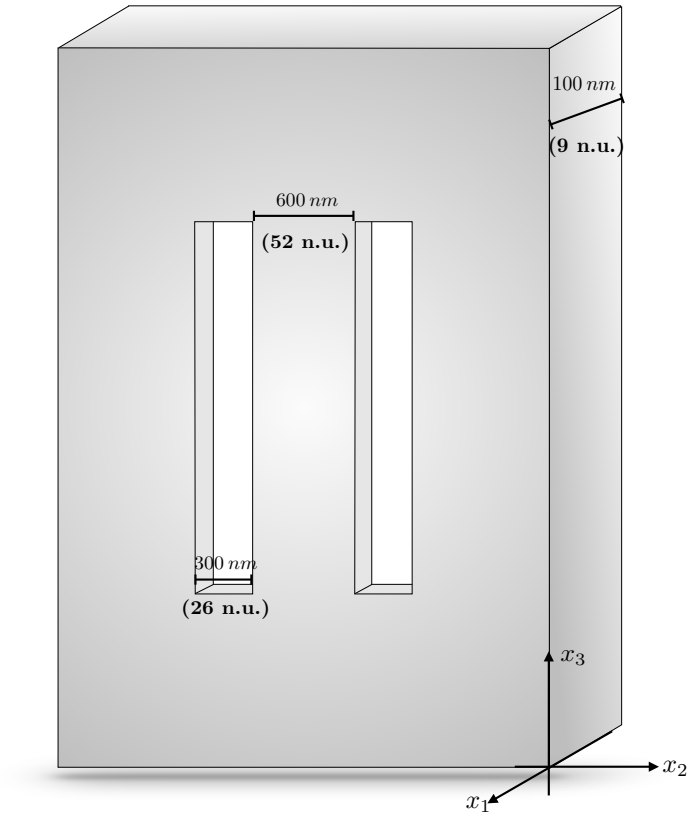

Figure 3.4: Titanium foil display in 3D - with and without normalized units

These parameters are defined as:

$$a_0 = 0.855 \times 10^{-9}\ I^{1/2}[\text{W/cm}^2]\ \lambda[\mu\text{m}] \tag{3.2a}$$

$$\omega_0 = \frac{\omega_{laser}}{\omega_{pe}} \tag{3.2b}$$

For the pulse duration, a polynomial longitudinal profile is defined, characterized by 3 parameters: lon_{rise}, lon_{flat} and lon_{fall} (respectively the rising duration, the flat duration and the falling duration of the pulse), each one normalized according to the reference time. For this case one considers a non-flat pulse, meaning that each half of the pulse has 20 fs (the rising and the falling parts):

ω_0	a_0 (10^{14} W/cm^2)	a_0 (10^{15} W/cm^2)	a_0 (10^{16} W/cm^2)	lon_{rise}	lon_{flat}	lon_{rise}
0.0922	0.00684	0.0216	0.0684	512	0	512

Table 3.4: OSIRIS laser parameters

The polarization direction of the incident femtosecond pulse in the simulations is positioned parallel to the axis that includes both slits - direction x_2 as in figure 3.4.

Chapter 4

Results - OSIRIS Simulations

The simulations take place in 1D and 2D (fig. 4.1) windows.

The 1D simulations are only implemented for temperature diagnostics, in order to compare with the TTM. Here, the target is just a linear profile with electrons and protons, and for that reason no transverse heat propagation takes place.

For the 2D simulations, the target will have a double opening, the *double slit*, which will evolve according to the interaction of the laser with the structure. Already at the first cycle of the laser beam the electron temperature reaches a peak value, making the slits close as time goes by as expansion takes place. Before showing the results of the simulation, a perspective on the laser beam propagation with or without foil is given (section 4.1).

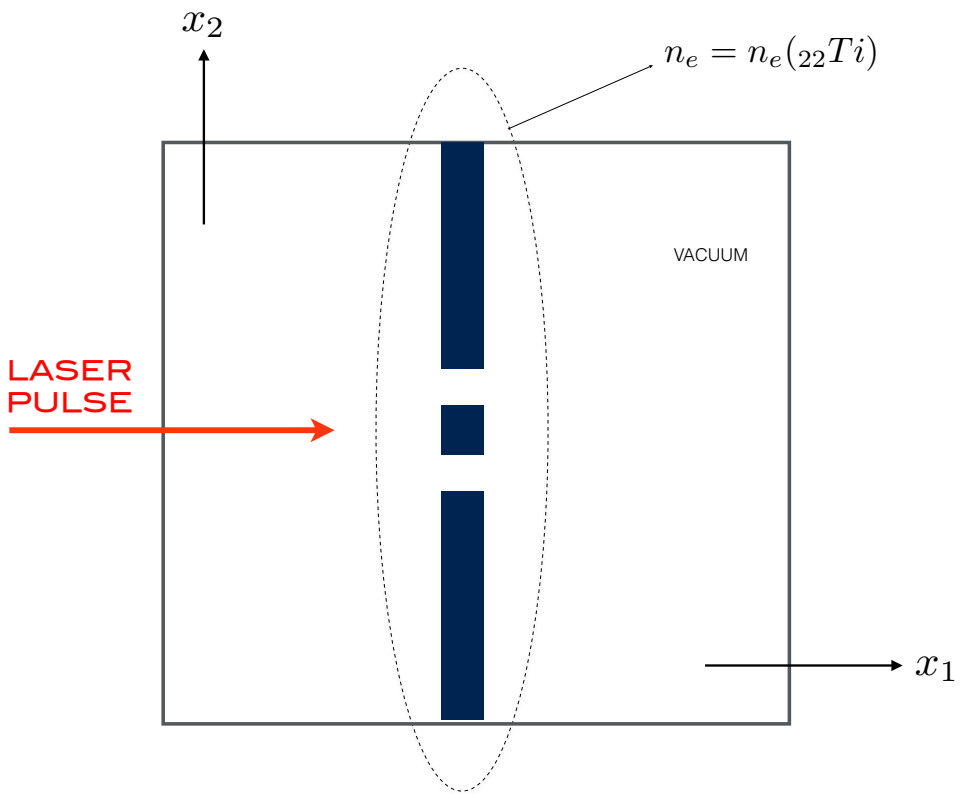

Figure 4.1: 2D simulation window

4.1 Laser beam

A display for the laser beam propagation within the 2D simulation box is here provided. The focus is located on $x_1 = 0$ and each plot is retrieved in steps of 10 fs ($\tau_p = 40$ fs). The intensity is $I_0 = 10^{16}$ W/cm^2 ($a_0 = 0.0684$), the spot size is 1 μm and the simulation box is slightly larger (500 by 900) than the upcoming simulations in 2D. From this test one can observe the change of behaviour of the beam fronts when a dense target is introduced.

4.1.1 No foil

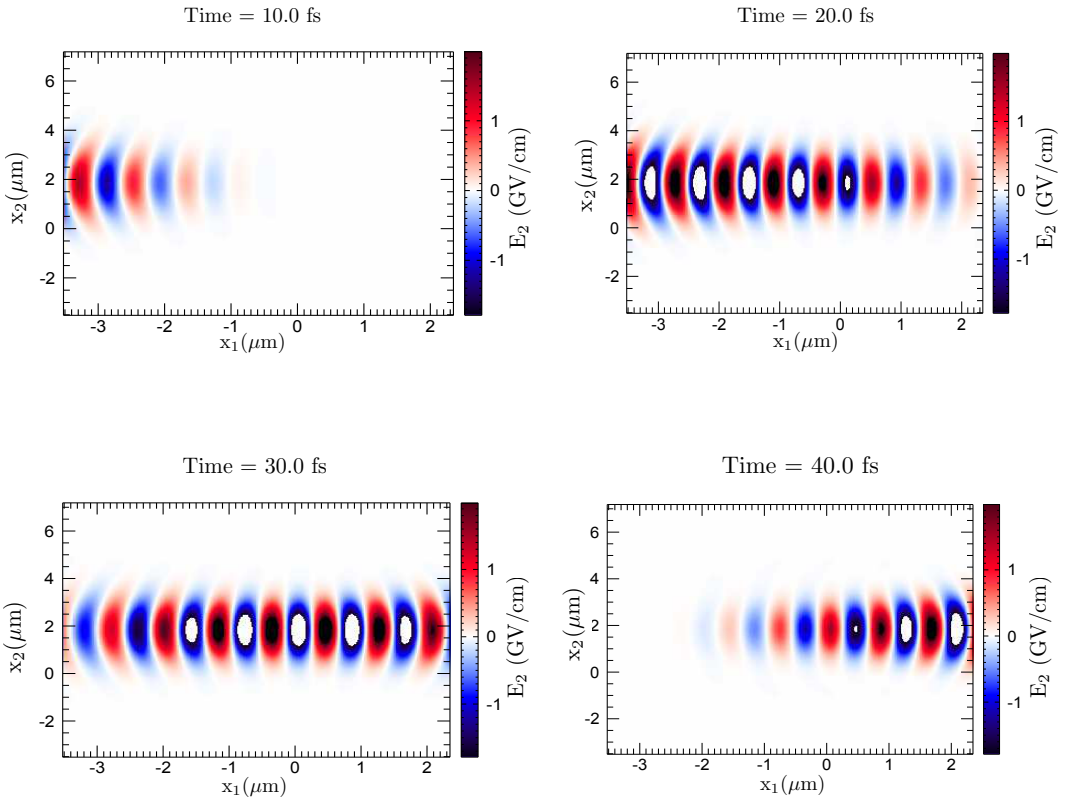

Figure 4.2: Laser beam with no foil (intervals of 10 fs).

4.1.2 With foil

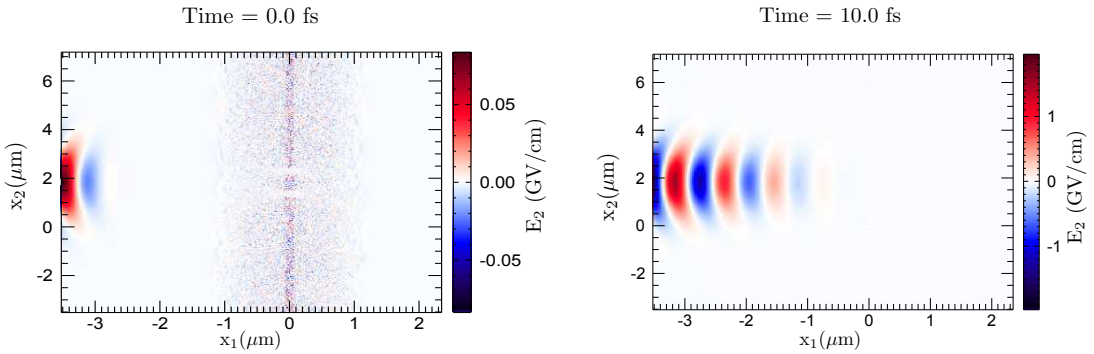

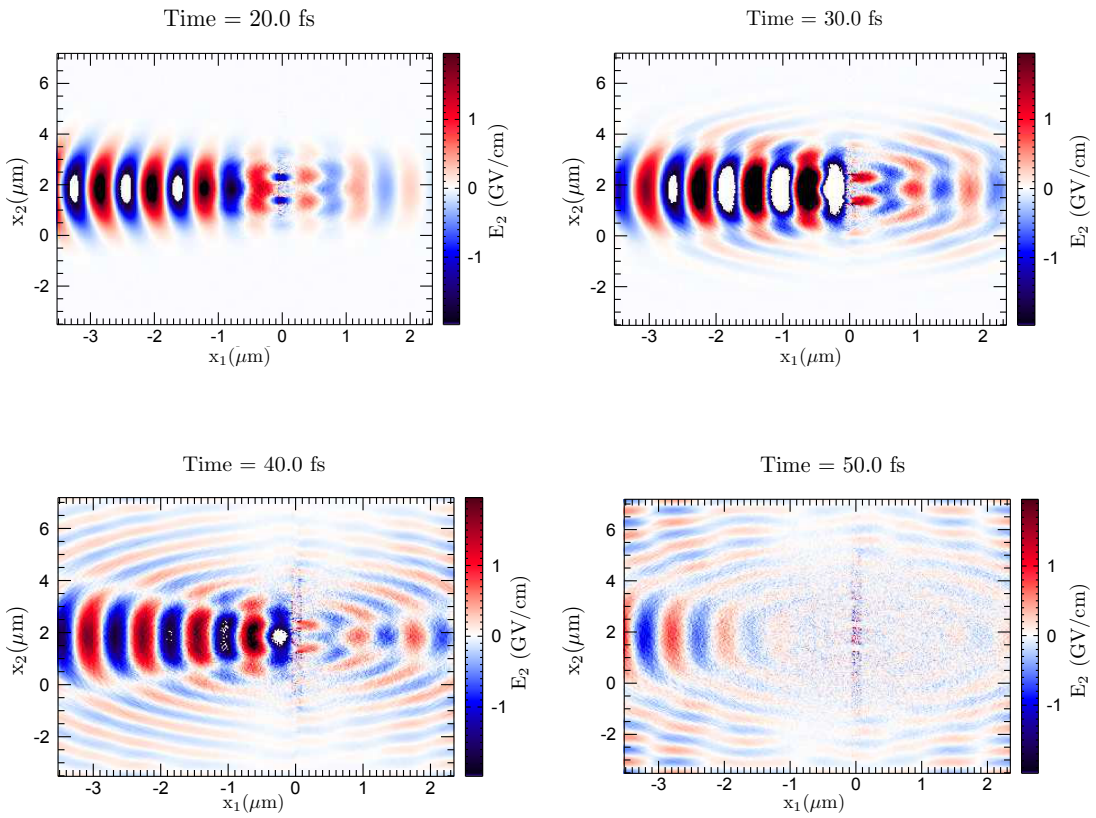

Figure 4.3: Laser propagation in simulation box - with Ti foil (intervals of 10 fs).

By comparing figures 4.2 and 4.3, one can see the beam deformation caused by the foil. The beam, after reaching the slits, features two behaviours: 1st, the waves diffract and make a characteristic pattern by constructive and destructive interference of the refracted beam fronts; 2nd, a part of the beam is reflected ($\omega_{pe} > \omega_{laser}$), and the reflected wavefronts interfere with the incoming waves, making themselves an intensity pattern as well.

4.2 Temperature profiles - 1D

In this section, a 1D profile for the Titanium is implemented, to make a further comparison with the results from the TTM (chapter 5) and check the compatibility of this theoretical model with the OSIRIS results.

The simulations are limited to simulation power and parameters. Not only is the simulation duration t_{sim} relevant ($\Delta t_{\text{ref}} \ll t_{\text{sim}} \sim$ ps), but also does the number of particles per cell (p.p.c.) have an important role for the convergence of the results. Maintaining the simulation duration the same for all intensities, while an oversized number of p.p.c. can improve the results, on the other hand by raising this number the simulations become extremely long in terms of CPU hours. The chosen approach is the following:

- **1st: Determine the equilibrium temperature for a given value of p.p.c.**

  - For the electrons, take ($T(t_0)$,t_0) points and make a fit for an exponentially decreasing function with an equilibrium temperature - $T(t) = T_{eq} + ae^{-bt}$ - starting from the peak temperature

- For the protons, retrieve points ($T(t_0)$,t_0) and make a fit for a 2 region function: the first region with an exponential increase of the temperature; the second region, with an exponential decrease tending to an equilibrium temperature. 2 sets of hyperbolic tangents, similar to the Heaviside function, are used to weight the exponentials in the right regions - $T(t) = 0.5\,a(\tanh(-b(t-c)) + 1)(1 - e^{-dt}) + 0.5\,T_{eq}(\tanh(e(t-f)) + 1)(ge^{-ht} + 1)$ - starting from the room temperature

- Make the average between the equilibrium temperatures obtained for both species and get the T_{eq} associated to a given number of p.p.c.

- Repeat the same procedure using a different number of p.p.c. (500, 1200, 3000 and 8000)

- **2nd: Determine the final equilibrium temperature for each intensity using different values for the p.p.c.**

- Make a fit for an exponentially increasing function tending to a limit in the infinity of the equilibrium temperatures T_{eq} as a function of the number n of particles per cell used - $T_{eq}(n) = T_{eq_{final}}(1 - e^{-bn})$

- Obtain the parameter $T_{eq_{final}}$

- Repeat the same procedure using a different intensity

The results of several simulations are provided in the following subsections.

$I_0 = 10^{14}$ W/cm^2

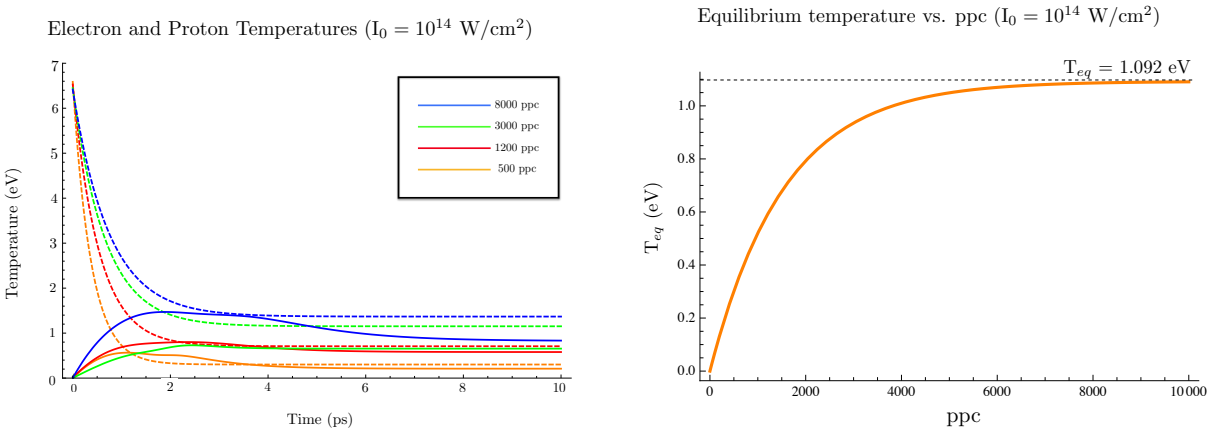

(a) Temperature (in eV) as a function of time for different number of ppc (electrons in dashed, and protons in thick)

(b) Equilibrium temperatures (in eV) as a function of the number of ppc

Figure 4.4: 1D analysis ($I_0 = 10^{14}$ W/cm^2)

$I_0 = 10^{15}$ W/cm^2

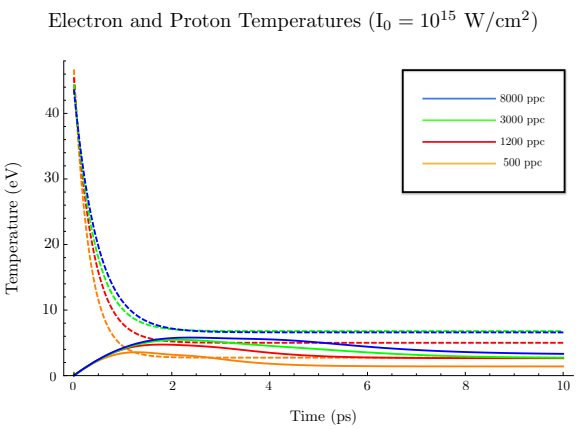

(a) Temperature (in eV) as a function of time for different number of ppc (electrons in dashed, and protons in thick)

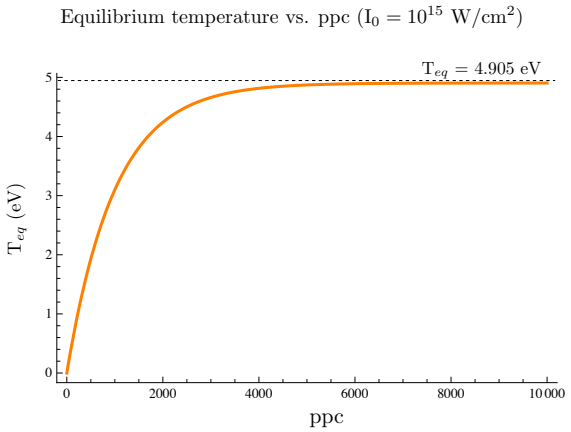

(b) Equilibrium temperatures (in eV) as a function of the number of ppc

Figure 4.5: 1D analysis ($I_0 = 10^{15}$ W/cm^2)

$I_0 = 10^{16}$ W/cm^2

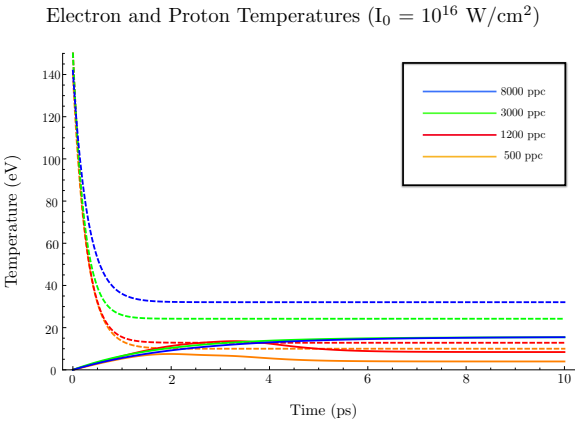

(a) Species' temperature (in eV) as a function of time for different number of ppc (electrons in dashed, and protons in thick)

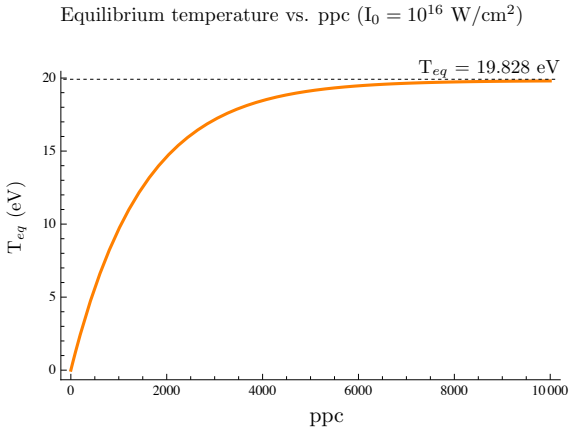

(b) Equilibrium temperatures (in eV) as a function of the number of ppc

Figure 4.6: 1D analysis ($I_0 = 10^{16}$ W/cm^2)

The points used for the fits were retrieved distinctly for electrons and protons.

The electron temperatures for the different instants were taken at the position where the maximum temperature was reached. On the other hand, for the protons the selected region for data collection was not so direct. In the simulations, the protons reach a peak in the beginning, something that the TTM does not predict (shown in subsection 4.3.1). They begin by heating for some eV at the front of the target (at the position where the electrons reach the peak), and after they experience a cooling down the protons in the inner part of the profile begin to warm up. The behaviour of this inner zone more or less matches the one expected by the TTM, i.e. a slow increase towards an equilibrium value (although showing a peak value for certain cases), hence the proton temperatures were retrieved at this position and not at the same position from the electrons. This is the reason why the proton temperature is fitted

to exponential increasing and decreasing functions. Note that this 1D profile is still a plasma, not a rigid structure, therefore expansion can also take place which introduces modifications to the heating deposition and to the configuration itself.

Notice also that as the number of p.p.c. is raised, the equilibrium temperatures of electrons and protons tend to be even more distant. This effect is justified because the bigger the number of p.p.c., the more collisions will be present in the simulation, meaning that the species will take more time to thermalize.

Although the adjustment to the exponentials can give an idea of the behaviour of the species temperature, this procedure does not reproduce the temperature evolution 100% accurately. Again, this approach was made to obtain convergence of results and to get a set of parameters to compare with the TTM.

4.3 Temperature and density profiles

4.3.1 Temperature

In this subsection, two sorts of information are retrieved: the 2D views for the electron temperature (the ones absorbing the laser energy directly) at different instants and a graph for the maximum temperatures obtained in the 2D window for electrons and protons.

2D view ($I_0 = 10^{14}$ W/cm^2)

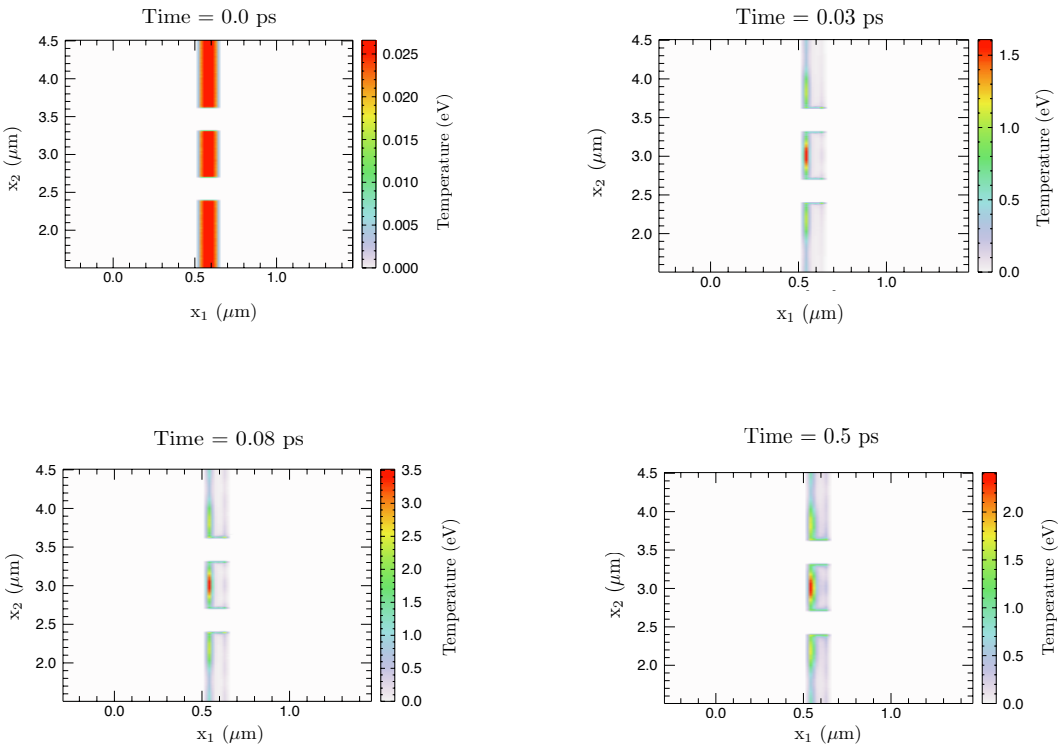

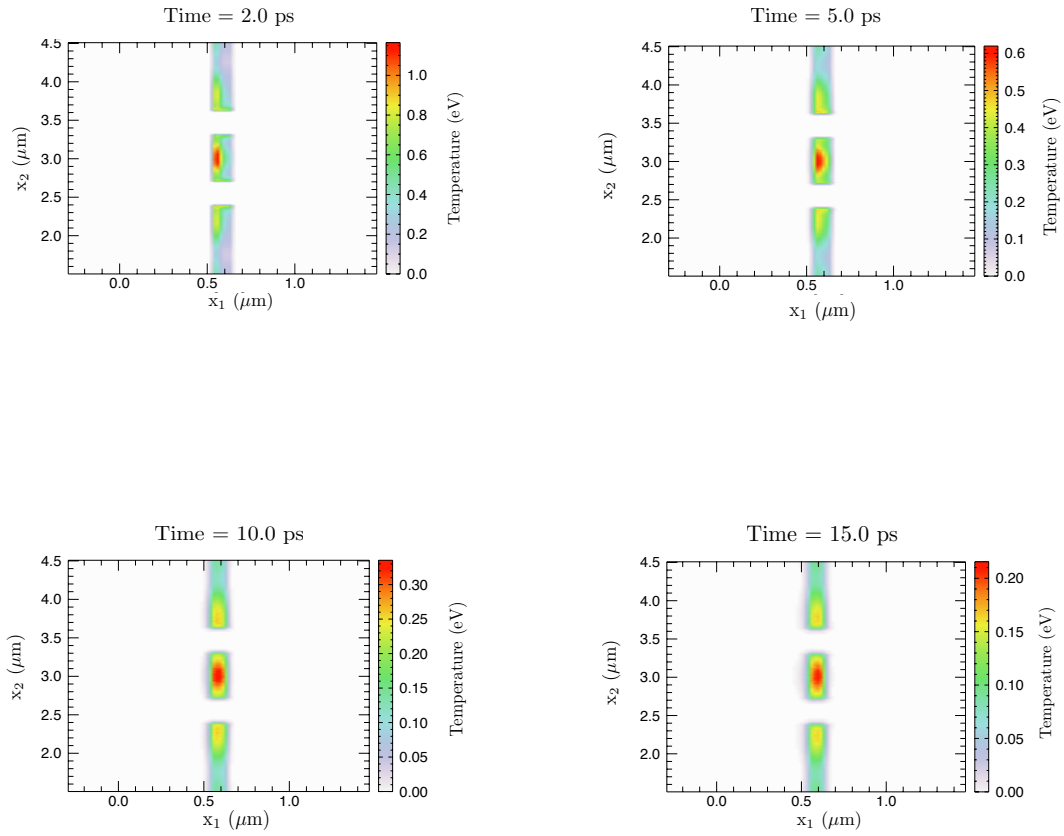

Figure 4.7: Full 2D (I_0 = 10^{14} W/cm^2)

Species maximum temperatures ($I_0 = 10^{14}$ W/cm^2)

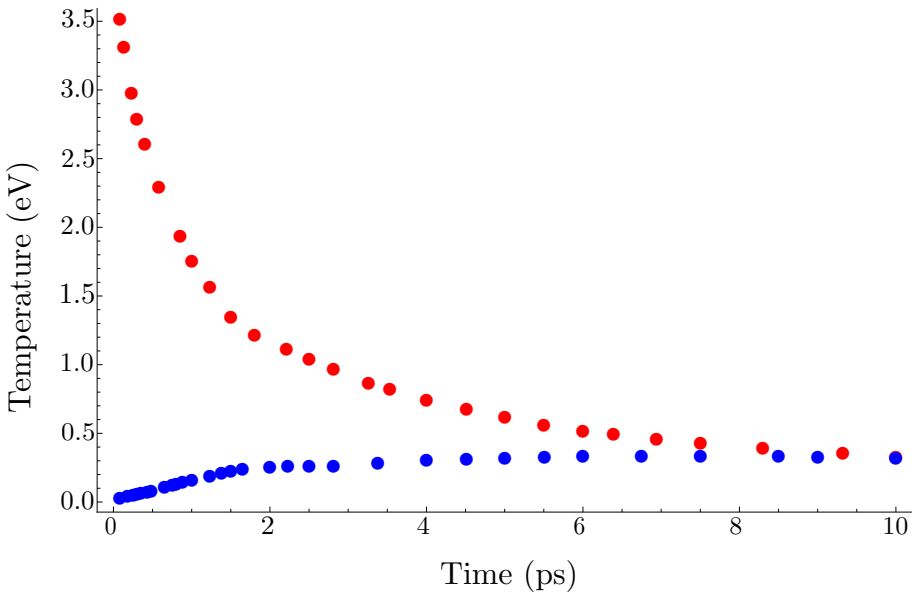

Figure 4.8: 2D Maximum Temperatures for I_0 = 10^{14} W/cm^2 (electrons - red, protons - blue)

2D view ($I_0 = 10^{16}$ W/cm^2)

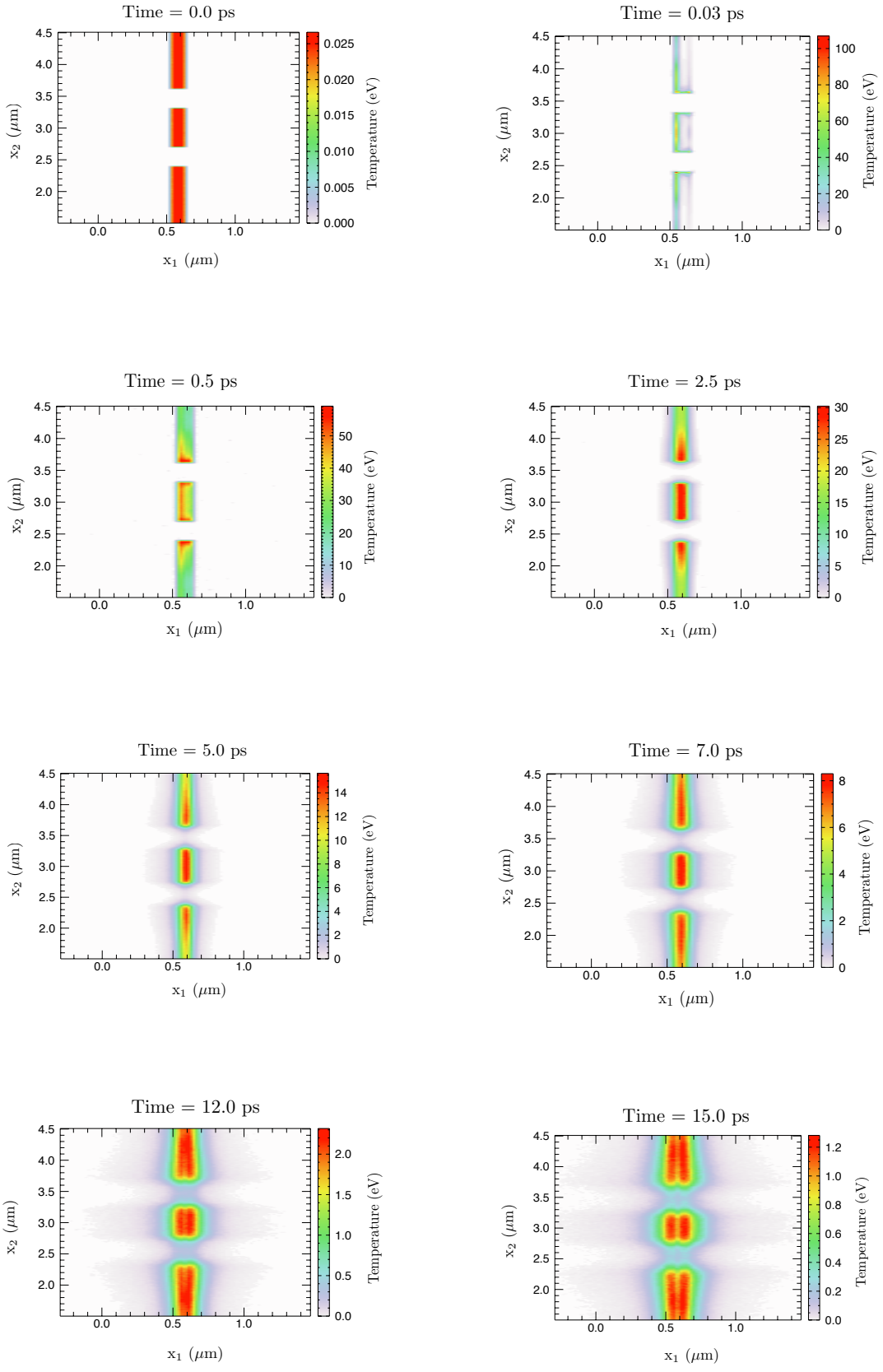

Figure 4.9: Full 2D (I_0 = 10^{16} W/cm^2)

Species maximum temperatures ($I_0 = 10^{16}$ W/cm^2)

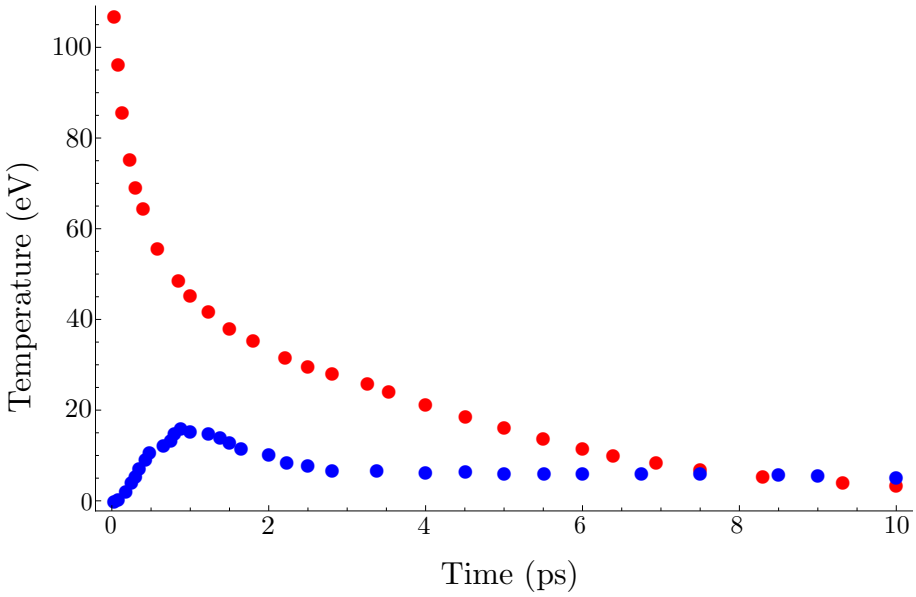

Figure 4.10: 2D Maximum Temperatures for I_0 = 10^{16} W/cm^2 (electrons - red, protons - blue)

The points retrieved for the species maximum temperatures were taken in different positions of the simulation box. Remind that in the TTM the analysis of the temperature is 1D and is made in a very localized region. However, in 2D the profile is not unidirectional and heat can propagate transversely.

An initial attempt to analyse the temperature evolution along time was done by fixing the position at a point close to the left bound of the target and on the horizontal axis of the simulation box. Although the peak temperature is clearly observed, as time goes by the heat flows onto a different region and the temperature in that point decreases abruptly to very low values when compared with the expected ones. This means that making an analysis of the temperature in a single point will not reproduce the physics of the system in terms of heat propagation.

The way found to obtain a temperature pattern for both species that clearly shows how the target is evolving was by registering the maximum values for several time steps and plot them in a graph. As expected the majority of the points were located near the left limit of the foil.

In the 2D windows for both intensities, a fraction of hot electrons propagate from the left to the right, remaining confined at the middle point. For I_0 = 10^{16} W/cm^2 the target featured a bigger thermalization comparing with I_0 = 10^{14} W/cm^2, meaning that bigger powers can heat an object as a whole more easily.

For I_0 = 10^{16} W/cm^2, like in the 1D profile, there is a peak for the proton temperature at the beginning of the simulation ($\simeq$ 1 ps), showing that at this magnitude the fields accelerate protons at the edge of the target. As referred previously, this intensity represents the transition between collisional and collisionless absorption, and this result, though only qualitatively, suggests that there might be some evidence of the latter as collisionless absorption is characterized by a more prominent temperature increase.

In conclusion, a comparison between the expected equilibrium temperatures in the 1D and the results obtained in the 2D is made. In the 2D simulations (both for the expansion and the temperature), a particle per cell number of 3600 (60 $\times$ 60 in x_1 and x_2) was used. The equilibrium temperatures obtained for

$I_0 = 10^{14}$ W/cm^2 and $I_0 = 10^{16}$ W/cm^2, from figures 4.8 and 4.10 respectively, are around 0.5 eV and 10 eV. Looking at the graphs of the equilibrium temperatures as a function of the p.p.c. (figures 4.4 and 4.6), for this same number of p.p.c. the expected value for T_{eq} is respectively 0.9 eV and 17 eV. The difference is not so big, but is understandable in light of the limiting validity of the $T_{eq}(p.p.c.)$ adjustment and because of the transverse heat propagation as highlighted before.

4.3.2 Density

The objective in this subsection is to observe the evolution in terms of the density of the Ti foil, i.e., how the expansion of the slab goes on after being irradiated by a laser pulse. 2D plots for the density evolution for $I_0 = 10^{14}$ W/cm^2 and $I_0 = 10^{16}$ W/cm^2 are shown.

For Titanium, one can use the ablation criterion formula (eq. 2.2.3) to find the theoretical temperature at which it should start ablating. Knowing that ΔH_v(Ti)$= 425$ kJ/mol, $T_0 = 300$ K and $\mathcal{C}_e(T_e) = \gamma T_e$, the formula is satisfied for $T_{ph} = 13694K \sim 1.19eV$. At this temperature the Titanium should start expanding.

2D view ($I_0 = 10^{14}$ W/cm^2)

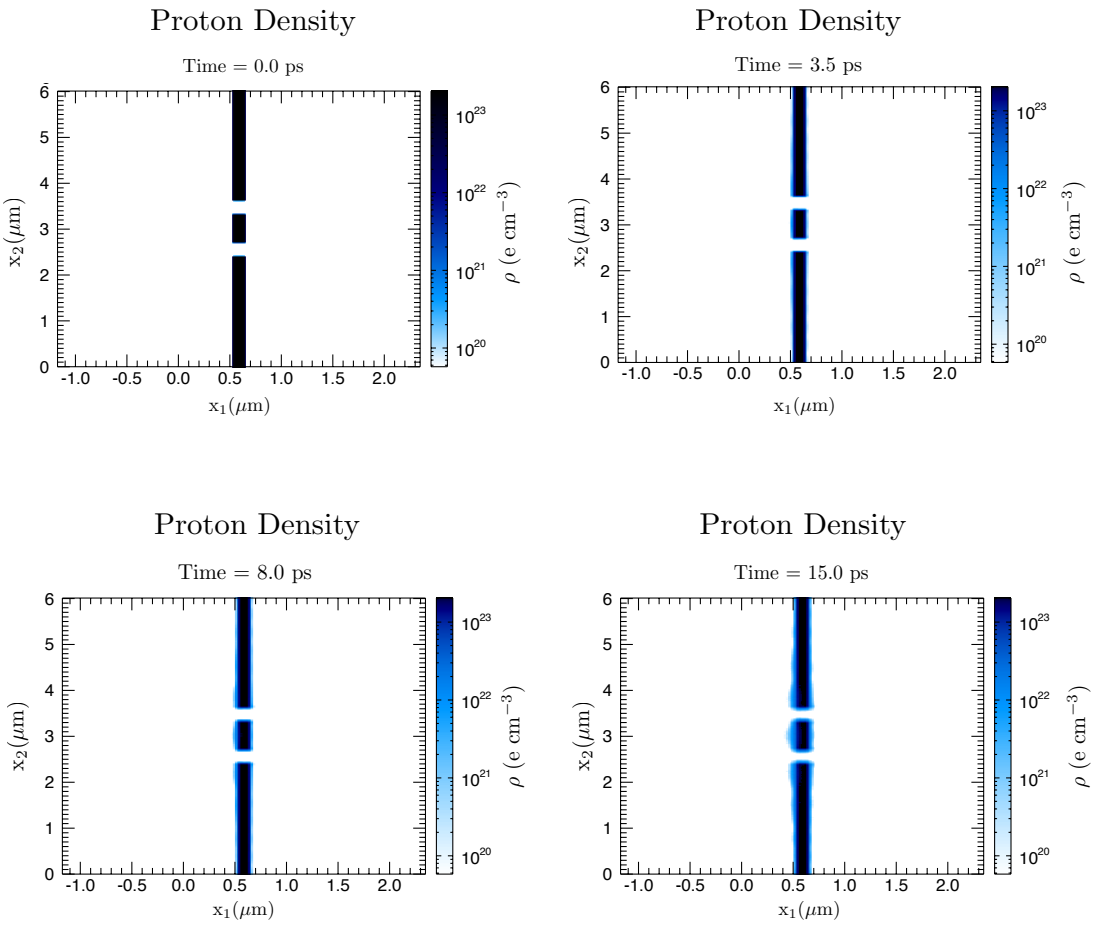

Figure 4.11: 2D profile of Ti foil evolution ($I_0 = 10^{14}$ W/cm^2)

2D view ($I_0 = 10^{14}$ W/cm^2)

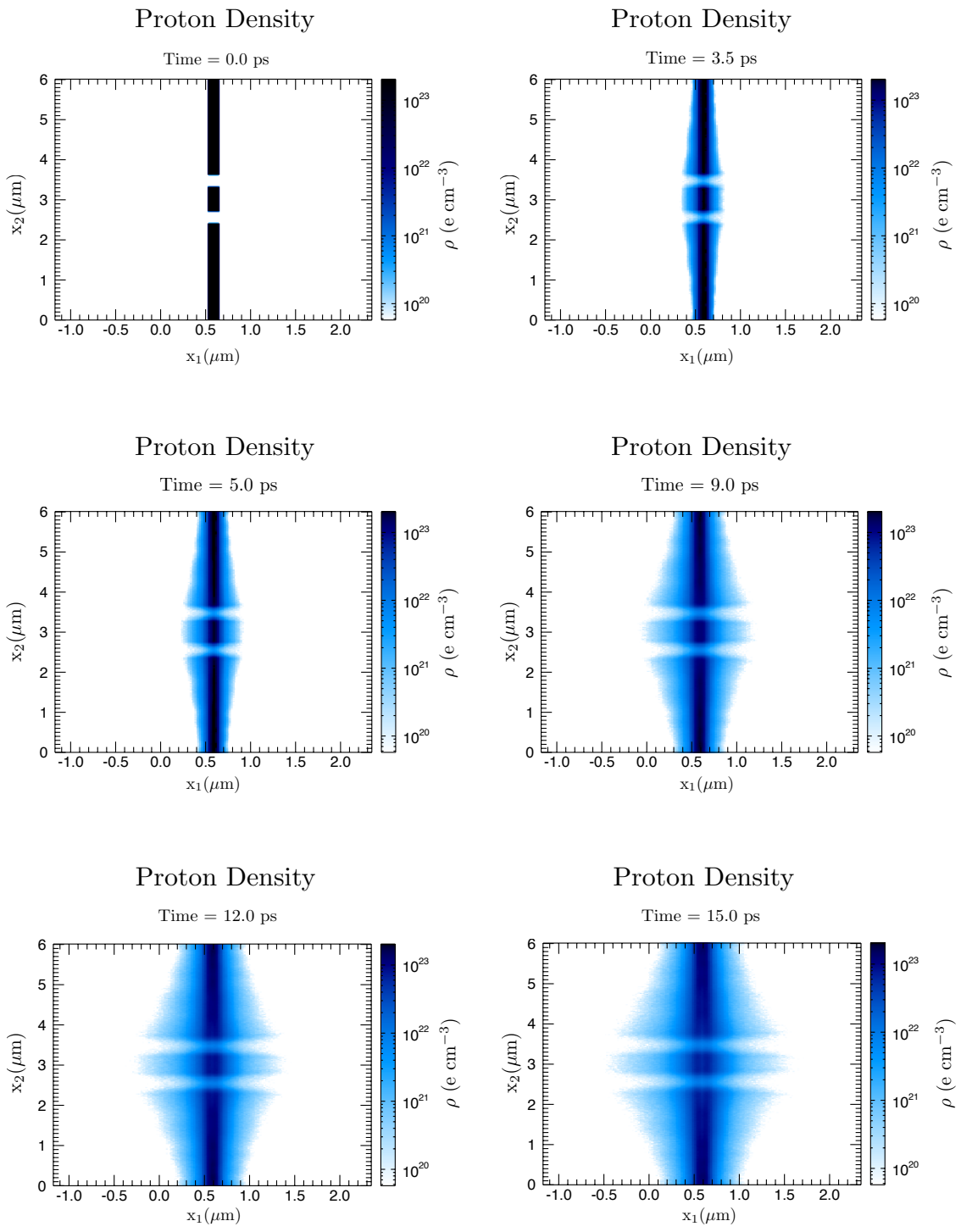

Figure 4.12: 2D profile of Ti foil evolution ($I_0 = 10^{16}$ W/cm^2)

4.3.3 Temperature and density lineouts

The lineouts in this subsection give a perspective on the correlation between density and temperature as time goes by, as well as on the range of values the density and temperature are reaching during the simulations. The lineouts cut the target in half (horizontally and vertically).

Longitudinal lineouts ($I_0 = 10^{14}$ W/cm^2)

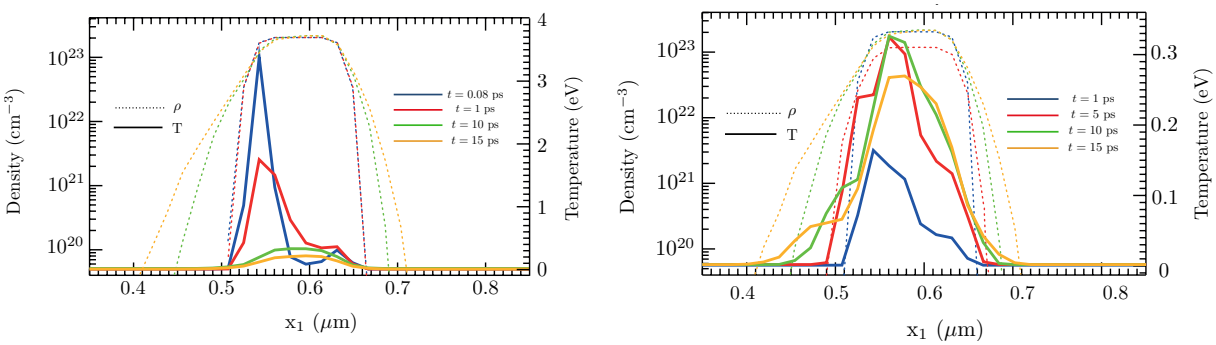

Figure 4.13: Longitudinal lineouts for temperature and density profiles of electrons (left) and protons (right) - $I_0 = 10^{14}$ W/cm^2

Transverse lineouts ($I_0 = 10^{14}$ W/cm^2)

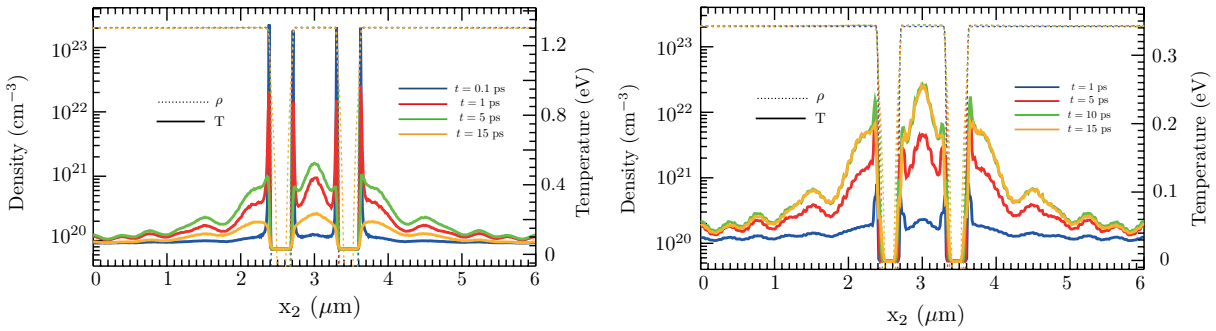

Figure 4.14: Transverse lineouts for temperature and density profiles of electrons (left) and protons (right) - $I_0 = 10^{14}$ W/cm^2

Longitudinal lineouts ($I_0 = 10^{16}$ W/cm^2)

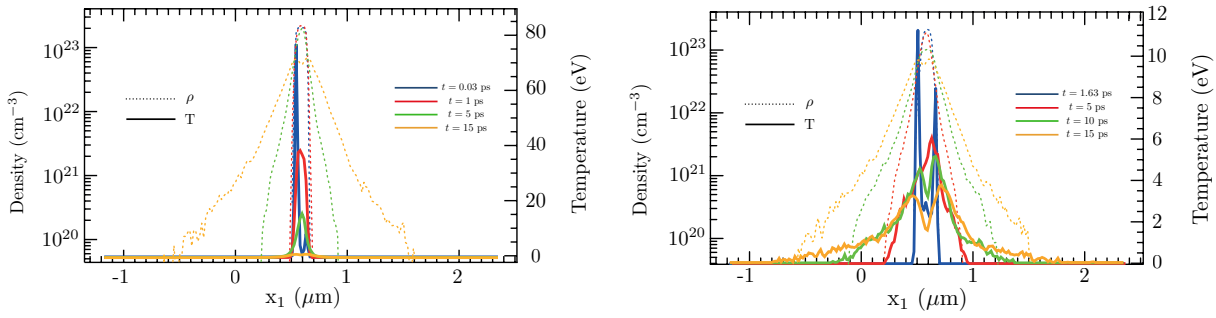

Figure 4.15: Longitudinal lineouts for temperature and density profiles of electrons (left) and protons (right) - $I_0 = 10^{16}$ W/cm^2

Transverse lineouts ($I_0 = 10^{16}$ W/cm^2)

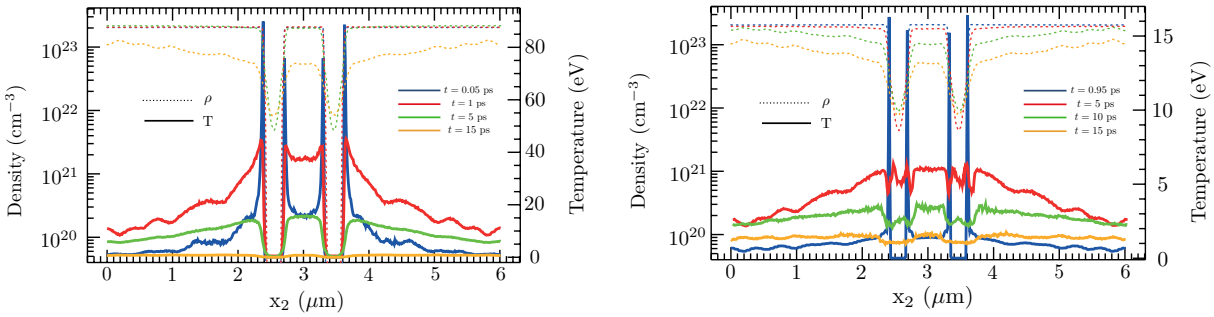

Figure 4.16: Transverse lineouts for temperature and density profiles of electrons (left) and protons (right) - $I_0 = 10^{16}$ W/cm^2

In terms of density, from the results for $I_0 = 10^{14}$ W/cm^2, one can conclude that the target barely expands during the temporal window of the simulation (it ablates $\simeq$ 100 nm maximum to the left). The slits themselves are closing really slowly as seen in the transverse profile, and this behaviour is also agreed by the density at the center of the foil, which is not changing significantly. On the other hand, for $I_0 = 10^{16}$ W/cm^2 a much more evident expansion takes place. The target reaches an horizontal expansion length of about 800 nm and at 5 ps the slits are already closed (closed in the sense that the density of protons filling the empty space has reached a sufficient magnitude to be considered as such, in this case with $\rho \sim 10^{22}$ cm^{-3}). Looking at the species density, unlike in the previous case, the density at the center drops after some picoseconds, lowering its magnitude in terms of density from 10^{23} to 10^{22}, which means that with this laser intensity the target itself trespasses the limit of solid density ($\rho_{solid} \sim 10^{23}$ cm^{-3}). Both species for the 2 intensities, though, follow the exact same pattern in terms of density, which is justified by the Coulomb force that makes the electrons and protons bound to each other.

In terms of temperature, the heating is more prominent on the tips of the foil as seen in the transverse lineouts, and the energy is more spread for the protons than for the electrons (which show a bigger temperature gradient) for both intensities. This is justified by the fact that the ions are much less collisional when comparing to electrons, meaning that heat takes more time to be transferred and so a more uniform temperature profile will arise. Again the protons reach a peak temperature and then cool down (the peak is reached more quickly for a higher power).

4.4 Field Enhancement

In this section, following the discussion in subsection 2.3.1, the electric field diagnostic after irradiation is made. Some intensity peaks should be visible at the edges of the foil slits.

The typical plot that follows the interaction of the pulse with the slab is shown below.

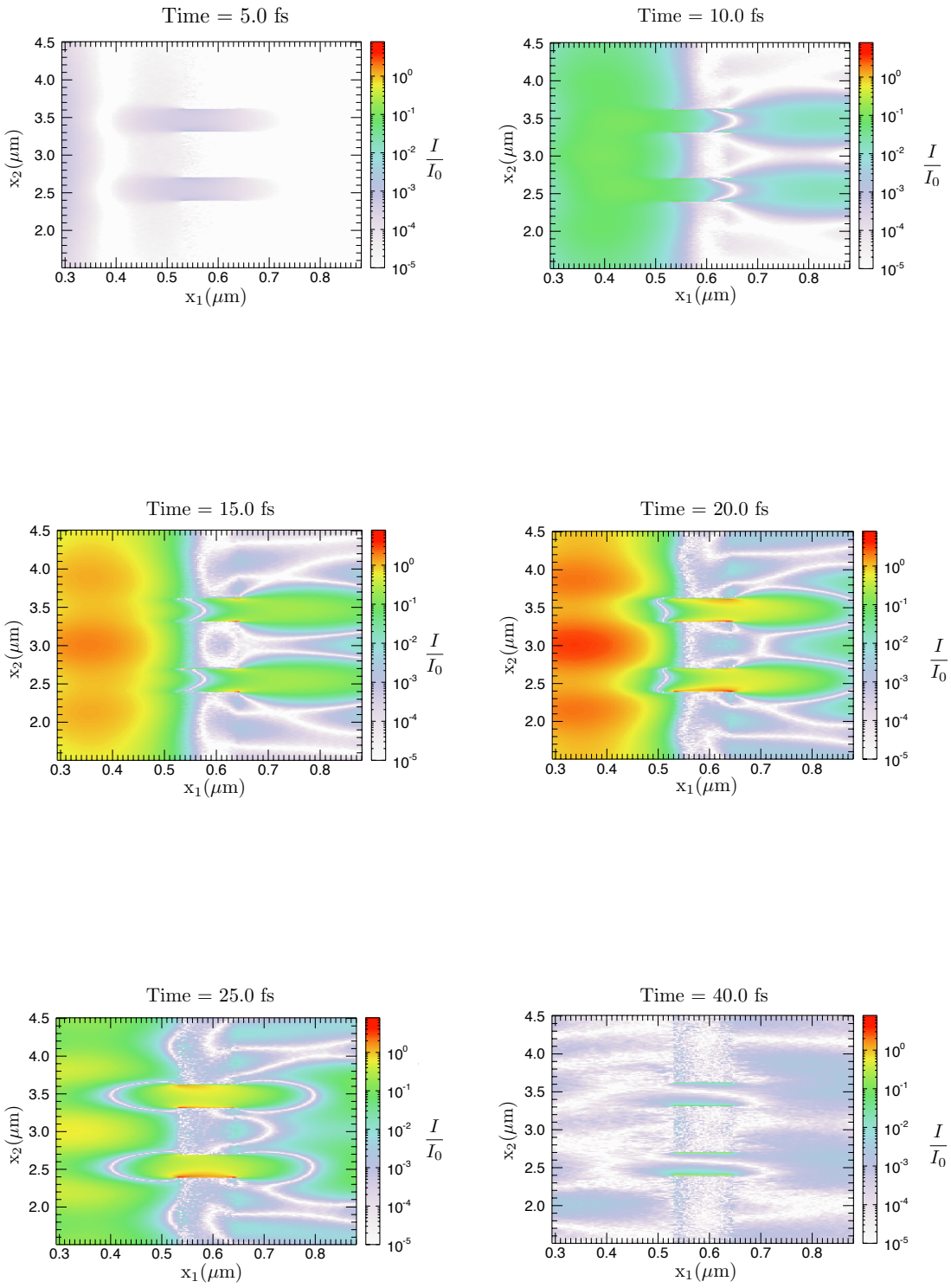

Figure 4.17: Field Enhancement 2D view ($I_0 = 10^{15}$ W/cm^2)

This can give a perspective on the foil heating, some interference phenomena taking place along the slit and reflection. In the following subsections the behaviour in terms of light intensity amplification at the edges of the foil and the duration of the enhanced signal is provided. Moreover, an analysis using a different slit size is done to explore some changes in terms of field enhancement.

4.4.1 $I_0 = 10^{14}\ W/cm^2$

Horizontal and vertical line-outs

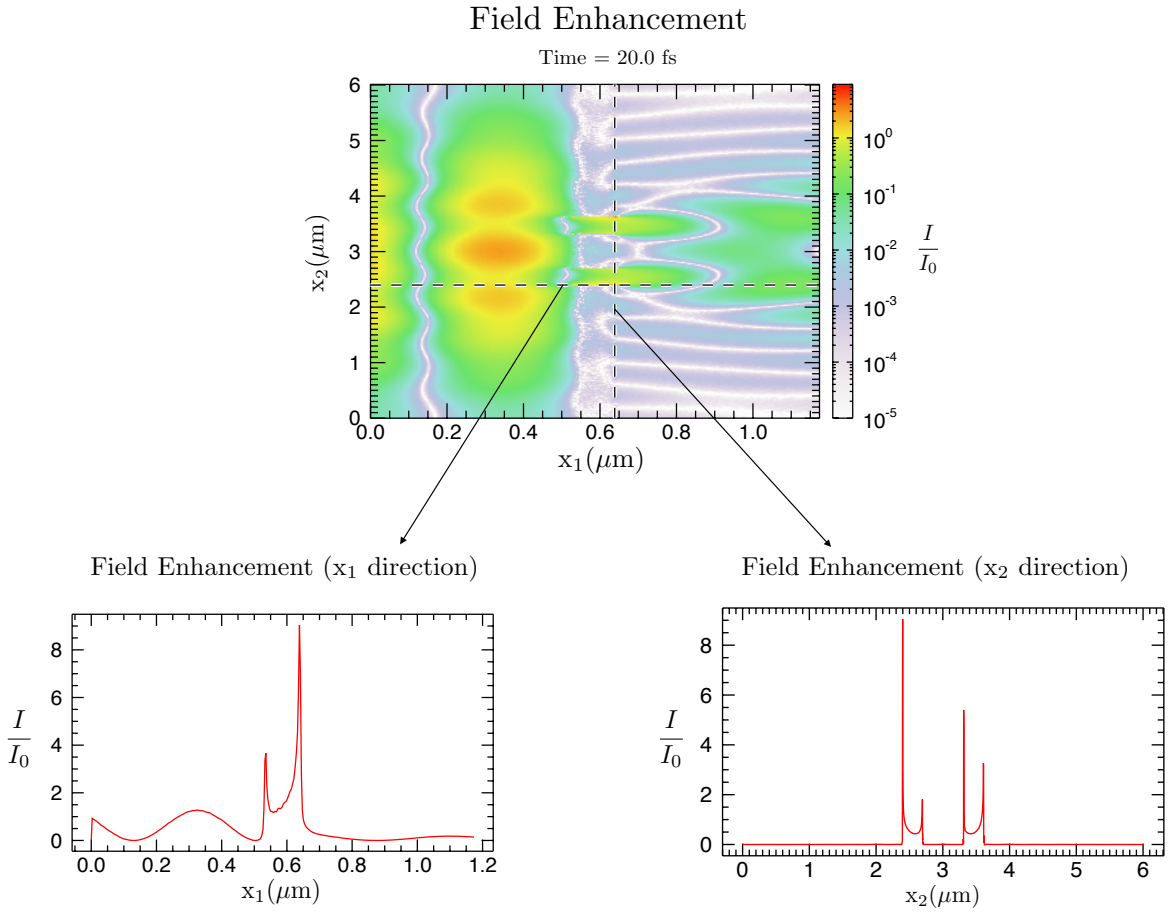

Figure 4.18: Field enhancement lineouts (25 fs)

Temporal evolution of maximum field enhancement

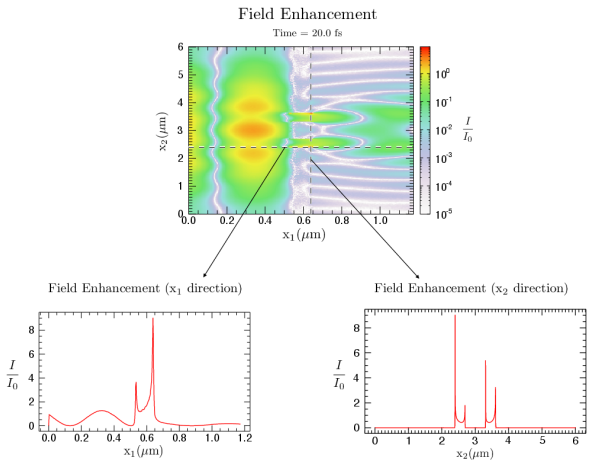

Figure 4.19: Field enhancement peak evolution along time

4.4.2 $I_0 = 10^{15}\ W/cm^2$

Horizontal and vertical line-outs

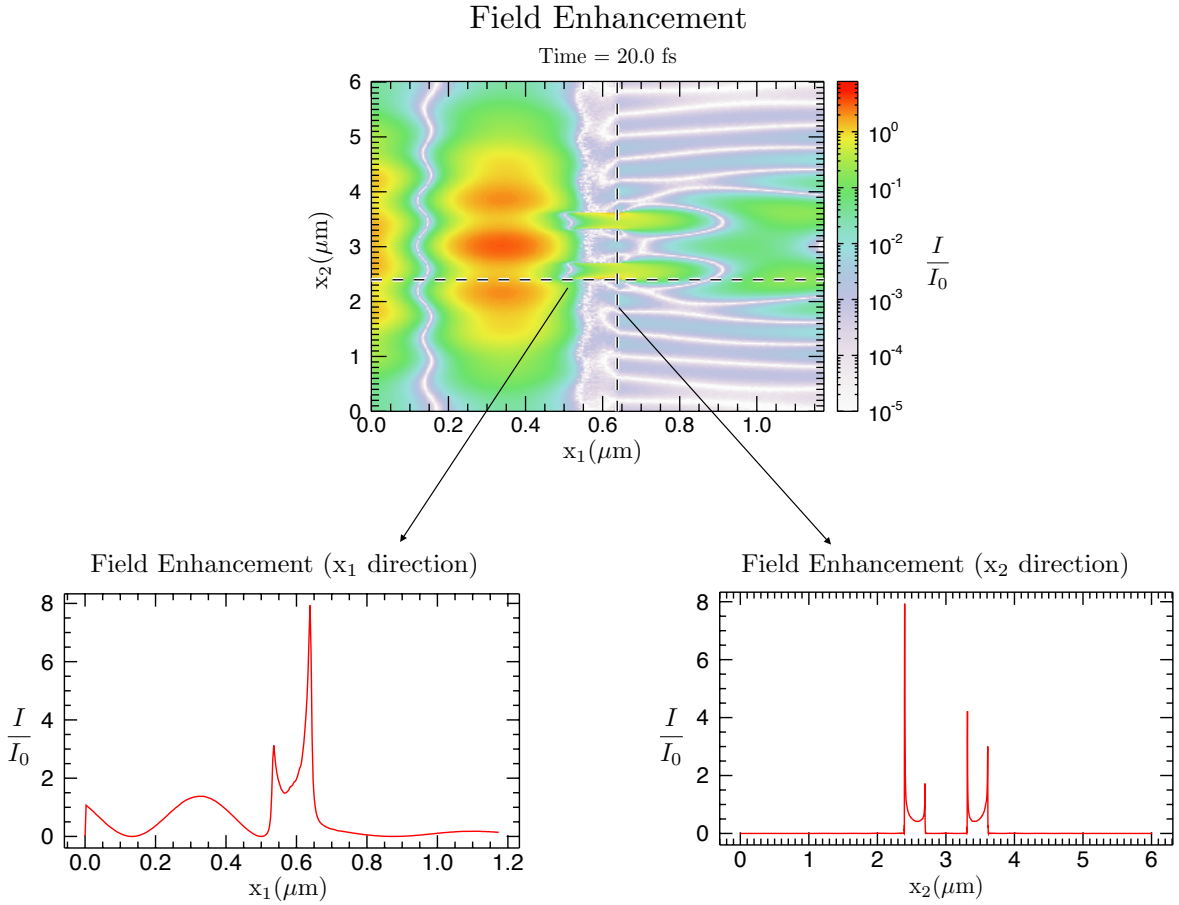

Figure 4.20: Field enhancement lineouts (25 fs)

Temporal evolution of maximum field enhancement

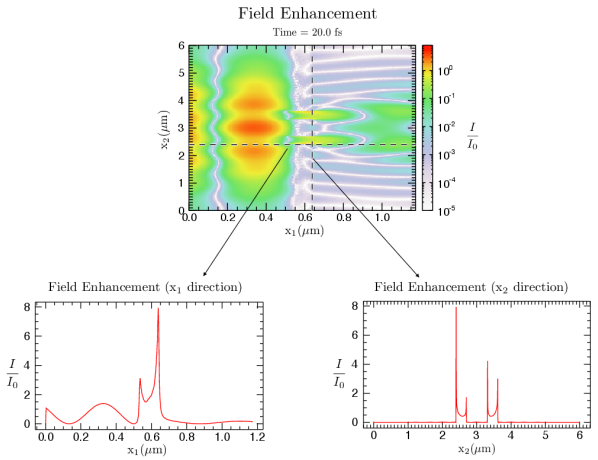

Figure 4.21: Field enhancement peak evolution along time

4.4.3 $I_0 = 10^{16}\ W/cm^2$

Horizontal and vertical line-outs

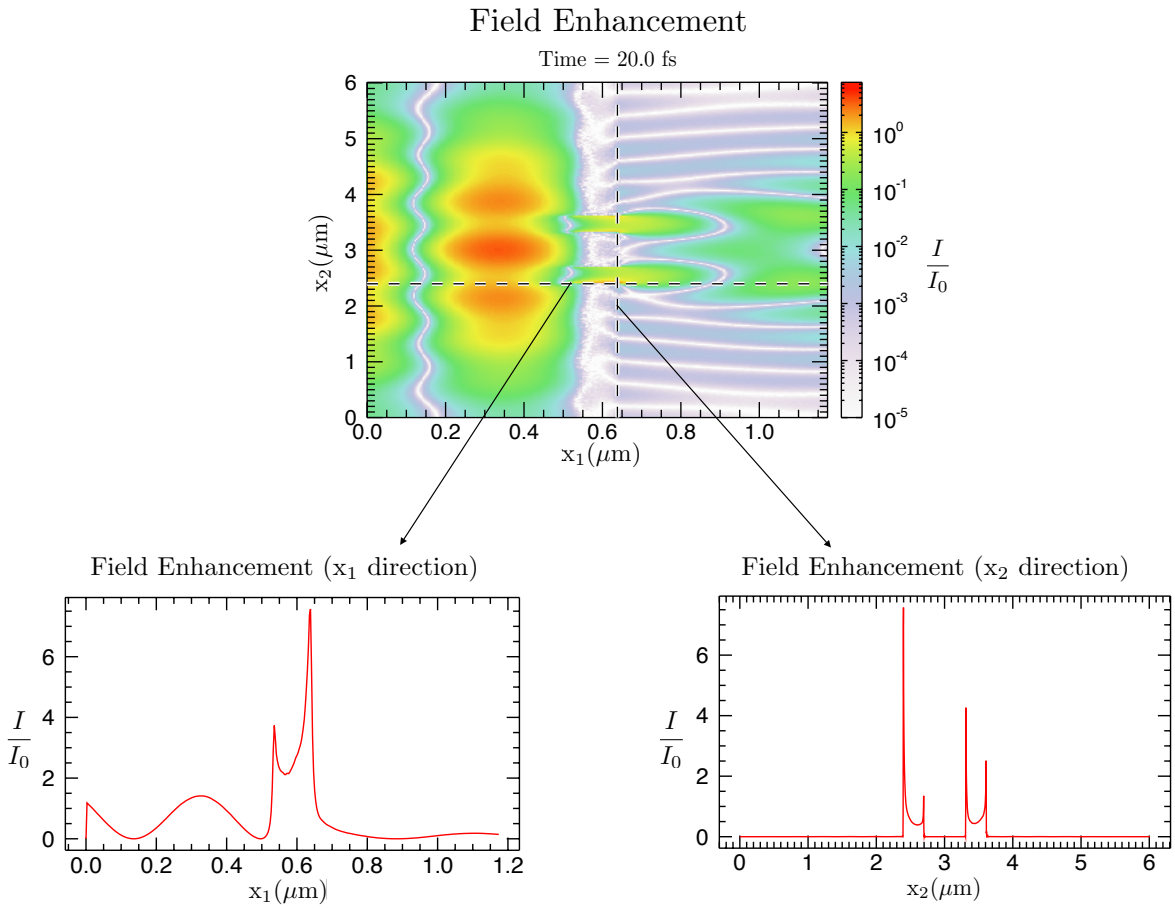

Figure 4.22: Field enhancement lineouts (25 fs)

Temporal evolution of maximum field enhancement

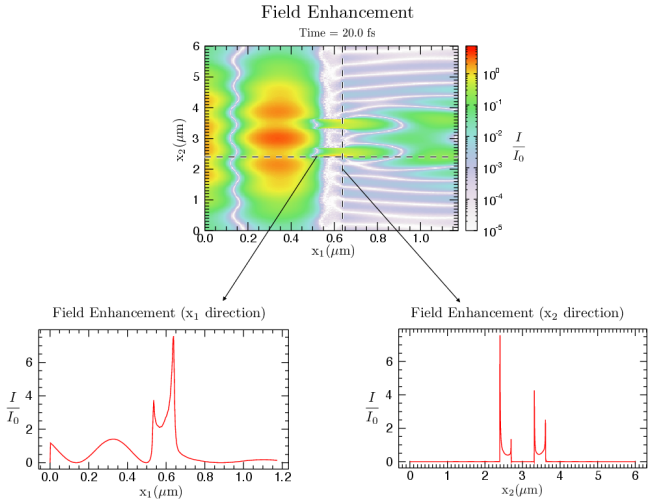

Figure 4.23: Field enhancement peak evolution along time

From the 2D plots and the lineouts one can observe that is close to the tips where the target displays a bigger enhancement factor, as expected. In addition, it is seen that the bigger the power of the laser, the smaller becomes the electric field amplification on the vicinity of the tips.

For all intensities, the maximum peak has a duration of $\simeq$ 20 fs, which is half of the pulse duration. This suggests that the system only starts feeling the perturbation 10 fs after the leading edge of the pulse interacts with the surface of the target, and returns to the initial state 10 fs before the pulse has crossed the full slab area.

4.4.4 Smaller slit size

Instead of using slits with a size of 300 nm, in this subsection the slit size will be considerably smaller, about 10 times smaller than the wavelength ($d_{slit} \simeq 80$ nm), using an intensity of 10^{14} W/cm^2. The maximum enhancement is given in figure 4.24.

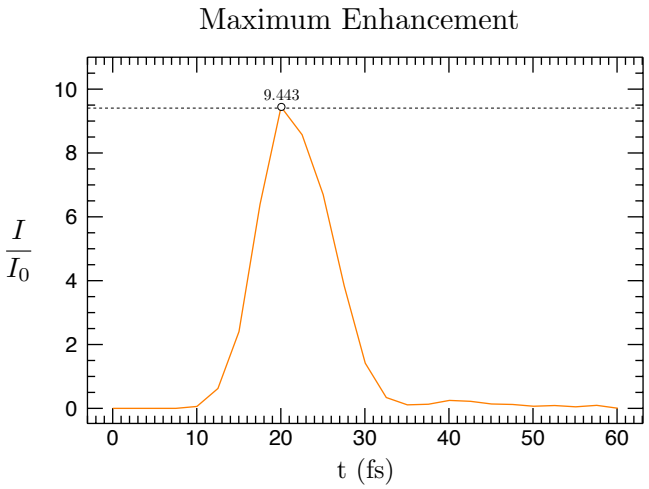

Figure 4.24: Field enhancement peak evolution along time ($I_0 = 10^{14}$ W/cm^2 and $d_{slit} = 80$ nm)

A smaller slit size originated a bigger enhancement peak value when compared with the case with 300 nm slits; however, there was only a slight increase from 9.139 to 9.443, meaning that there is no significant change. The smaller the slit the more confined can the collective plasmon oscillations be, but the target implemented is not a real compact solid and this fact has proven to have a bigger role for the enhancement to take place.

Chapter 5

Discussion of Results

5.1 Comparison with temperature models

5.1.1 Two Temperature Model

The laser source term for solving the differential equations 2.38a and 2.38b for the TTM depends on reflectivity, absorption, laser intensity and a function - $g_L(x,t)$ - which states the space and time dependence of the pulse. For Gaussian pulses, $g_L(x,t)$ can be taken as

$$g_L(x,t) = \sqrt{\frac{4\ln 2}{\pi}} \exp\left[-4\ln 2\Big(\frac{t-2\tau_p}{\tau_p}\Big)^2\right] \simeq 0.94 \exp\left[-2.77\Big(\frac{t-2\tau_p}{\tau_p}\Big)^2\right] \tag{5.1}$$

The laser source function is therefore written as [29]:

$$S(x,t) = 0.94(1-R)I_0\,\alpha \exp\left[-\alpha x - 2.77\Big(\frac{t-2\tau_p}{\tau_p}\Big)^2\right] \tag{5.2}$$

In addition, the electron heat conductivity is considered to be linearly dependent on the temperature:

$$\lambda(T_e) = \lambda_0 \frac{T_e}{T_0} \tag{5.3}$$

where T_0 is the room temperature and λ_0 is the conductivity at room temperature. The remaining constants depend on the specie itself. Before analysing the results for Titanium, and in order to verify the consistency of the implemented model, this same system can be tested using an element which is frequently used in TTM experiments - Gold.

TTM - Gold

The parameters for Gold are tabulated in table 5.1. The electron heat capacity is temperature dependent and the heat capacity for the lattice is considered to be the same as the bulk heat capacity of the material.

$\mathcal{C}_p$ (J cm^{-3} K^{-1})	γ (J cm^{-3} K^{-2})	R (800 nm)
2.49	6.7$\times$ 10^{-5}	0.93
h$_{ex}$ (GW cm^{-3} K^{-1})	α (cm^{-1})	λ_0 (W cm^{-1} K^{-1})
26	7.31$\times$10^5	3.1

Table 5.1: Used Au parameter values - TTM

The work of Majchrzak and Dziatkiewicz [49] and its results are compared to our model. A 200 nm thick gold foil is irradiated with a laser beam of 800 nm, a fluence of 0.001 J/cm^2 and 100 fs pulse duration.

Using these parameters, the presented TTM provides the following results:

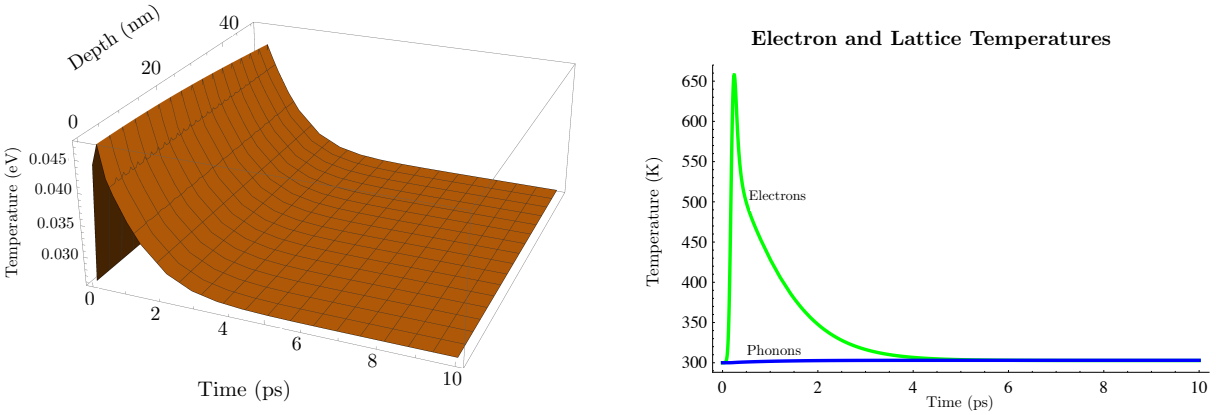

(a) Electron temperature (in eV) as a function of time and space

(b) 2-D graph for electron (green) and phonon (blue) temperatures

Figure 5.1: TTM model - Gold ($I_0 = 1 \times 10^{10}$ W/cm^2)

This leads to a peak temperature of nearly 658 K. The result from Majchrzak and Dziatkiewicz is shown in figure 5.2.

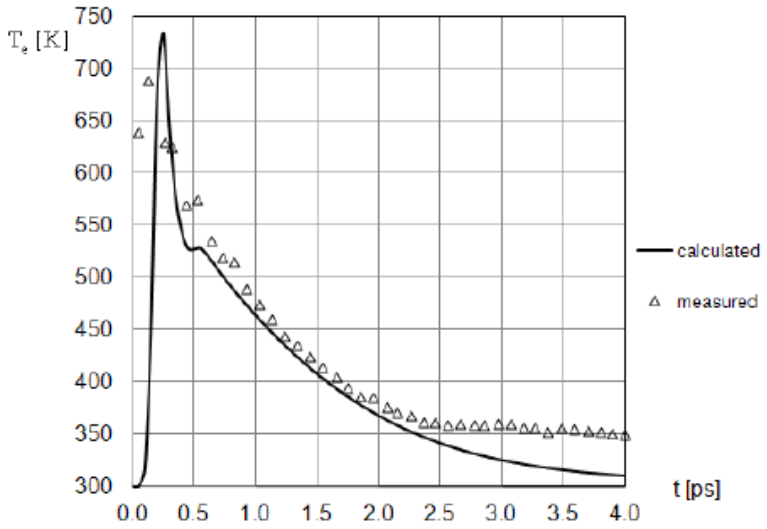

Figure 5.2: Electron temperature as a function of time (from [49])

The shape of the solutions follows a similar trend. The peak temperature for electrons is slightly

bigger (between 720-740 K), while it seems to stabilize after approximately 4 ps, which is compatible with our results of the TTM in figure 5.1.

In a paper from Tsai and Jiang [28], a 1053 nm laser with a fluence of $J = 0.05$ J/cm^2 and $\tau_p = 140$ fs duration irradiates a 100 nm thick foil. The results using those parameters in our model are the following:

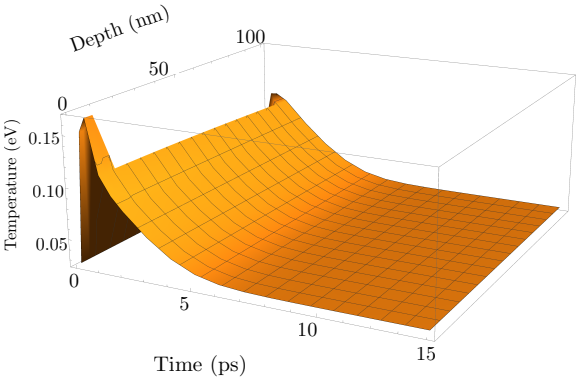

(a) Electron temperature (in eV) as a function of time and space

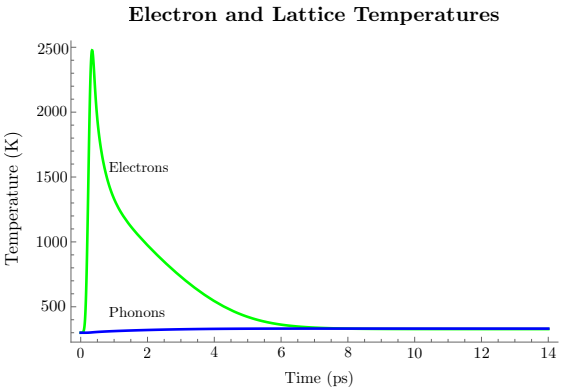

(b) 2-D graph for electron (green) and phonon (blue) temperatures

Figure 5.3: TTM model - Gold ($I_0 = 3.57 \times 10^{11}$ W/cm^2)

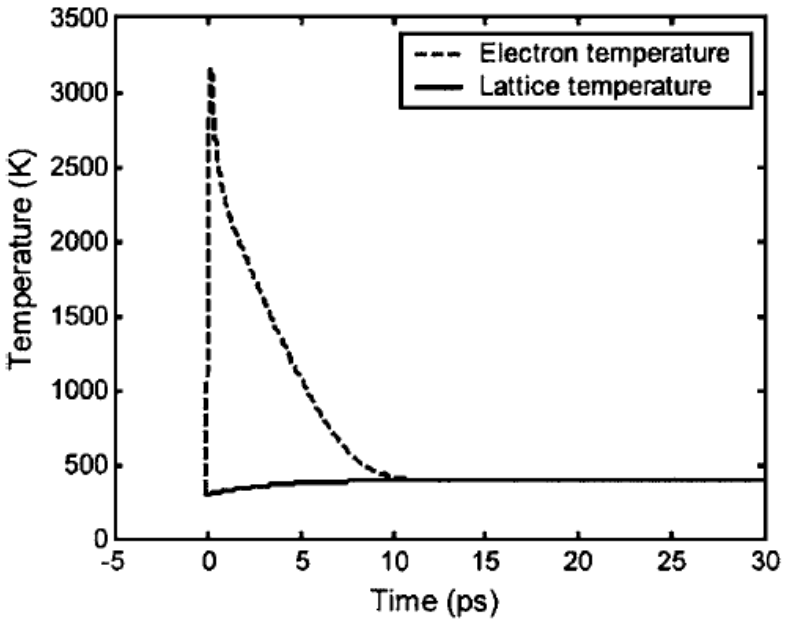

Figure 5.4: Electron and lattice temperatures as a function of time (from [28])

Like in the previous case, the shape of the graph and the temperature stability point match. The computed peak temperature is of 2477 K, which differs by some hundreds of Kelvins from the result in fig. 5.4 from Tsai and Jiang (between 3200-3300 K). However, one has to account for the fact that they did not clarify the values for some parameters, such as the reflectivity.

Therefore, from comparing the simulations of the TTM with the results from other authors, the implementation of the TTM made here is thus validated.

TTM - Titanium

To compare with the PIC results, the TTM is implemented with the same values for Ti. In table 5.2 the relevant parameters for the study-case are given.

$\mathcal{C}_p$ (J cm^{-3} K^{-1})	γ (J cm^{-3} K^{-2})	R
2.34	8.5$\times$ 10^{-5}	0.622
h$_{ex}$ (GW cm^{-3} K^{-1})	α (cm^{-1})	λ_0 (W cm^{-1} K^{-1})
1207	6.3$\times$10^5	0.22

Table 5.2: Ti parameter values - TTM

For the boundary condition, since the metallic foil has a thickness of $L = 100$ nm and that $\tau_p = 40$ fs, the spatial and temporal intervals where the equation is solved are respectively $0 < x < L$ and $0 < t < 40\tau_p$, where τ_p is 40 fs as mentioned before.

Remind that the 1D regime of this case is only true when the spot size is much bigger than the optical penetration depth δ_{max}. The penetration depth is the inverse of the absorption coefficient, therefore $\delta_{max} = \frac{1}{\alpha} \approx 15.87$ nm. Since the spot size is $w_0 = 2\mu$m = 2000 nm $\gg \delta_{max}$, the approximation is considered as valid.

I$_0$ = 10^{14} W/cm^2

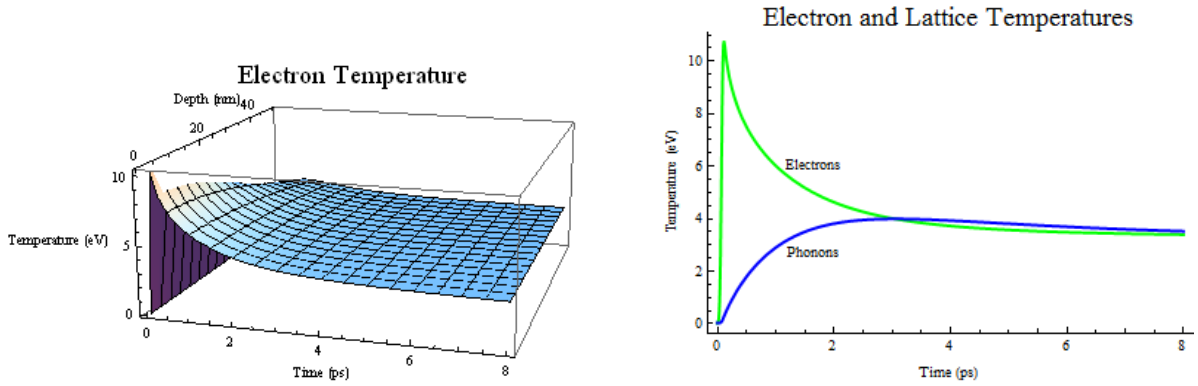

(a) Electron temperature (in eV) as a function of time and space

(b) 2-D graph for electron (green) and phonon (blue) temperatures

Figure 5.5: TTM model ($I_0 = 10^{14}$ W/cm^2)

I_0 = 10^{15} W/cm^2

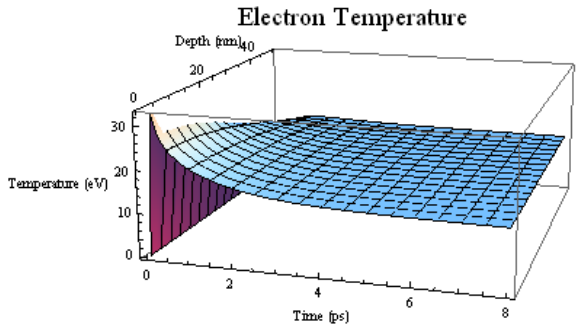

(a) Electron temperature (in eV) as a function of time and space

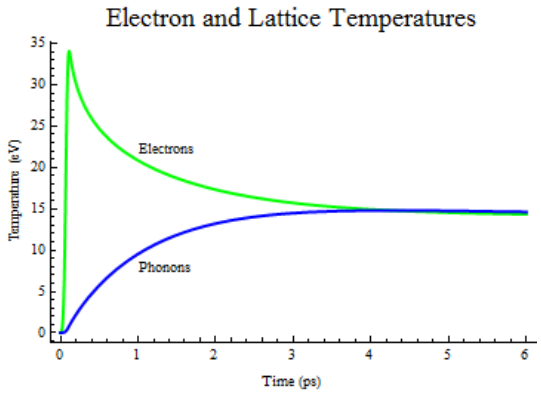

(b) 2-D graph for electron (green) and phonon (blue) temperatures

Figure 5.6: TTM model ($I_0 = 10^{15}$ W/cm^2)

I_0 = 10^{16} W/cm^2

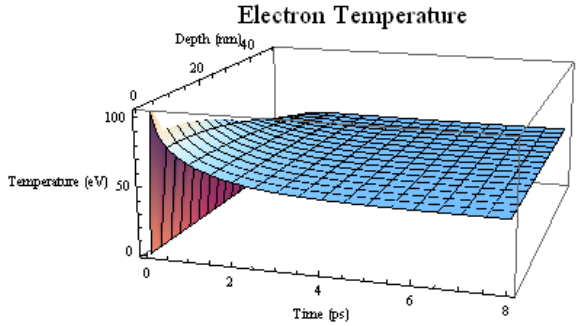

(a) Electron temperature (in eV) as a function of time and space

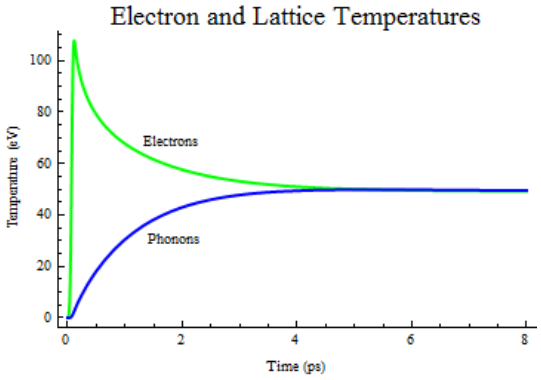

(b) 2-D graph for electron (green) and phonon (blue) temperatures

Figure 5.7: TTM model ($I_0 = 10^{16}$ W/cm^2)

5.2 Analysis of results

5.2.1 Temperature and expansion

In this subsection a discussion for both temperature and expansion is made, since both are intimately related.

The 1D simulations provide results slightly different from the ones given by the TTM. Despite the fact that in the 10^{14} W/cm^2 simulation in OSIRIS (fig. 4.4) there is a smaller peak value, the tendency is for the electron peak temperatures being even higher than the values from the solutions of the TTM as the intensity increases. A difference of $\simeq$ 10 eV for 10^{15} W/cm^2 and $\simeq$ 30 eV for 10^{16} W/cm^2 is observed between the TTM and the OSIRIS results. In a previous discussion (subsection 4.2) a similar effect was

also observed, as the protons were unexpectedly reaching a peak value. These phenomena made it clear that in OSIRIS the particles are being accelerated more intensely, acceleration which is originated by field and charge effects in narrow time scales, which are not present in hydrodynamic motion (and therefore not predicted by the TTM).

The equilibrium temperatures, in the opposite direction, are much lower than the results from the TTM, and the difference between both is getting bigger as the intensity increases. An important fact is that the 1D features side expansion as mentioned at the end of section 4.2, meaning there is lateral heat diffusion. The species temperature is decreasing slower and slower as time goes by; however, a 100$\%$ well established equilibrium temperature cannot be observed even for long expansion time (~ 15 ps) as the profile is continuously expanding. At a certain point of the simulation, though, this decrease is barely noticeable, so the species reach a fake 'thermalization', where one retrieves the equilibrium temperatures.

An ongoing matter of investigation is the reflectance of the laser pulse for different peak intensities in OSIRIS. The reflectivity of the laser in OSIRIS might be modelled in a different way than expected. Remind that the theoretical value for a Titanium slab with such geometry, given by the Fresnel formulas, is a fixed value (table 5.2) and does not take in account laser-plasma interaction. A next step for this study would be to investigate the fraction of the laser energy that is reflected by the foil.

In the 2D simulation plots it is not evident that the expansion takes place on the perpendicular direction unlike in the longitudinal direction. The reason for this behaviour is due to the initial slit width being 3 times bigger than the thickness of the foil, therefore a different scale for the axes on the x_1 and x_2 directions (x_1 is about 4 times smaller than x_2) was implemented to make it possible to observe the full picture of the system.

Again the PIC collision frequency is a sensitive point of the simulations. For this purpose a Spitzer collision frequency iteratively computed is a better approach than to fix the $\ln \Lambda$ and changing the dynamics of the ablating system. At low temperature this frequency is not well defined as regarded in subsection 3.2.2 and small tests were made using a fixed value. This difference severely modified the heating process and the expansion, showing that an automatic value leads to more reasonable results.

5.2.2 Field Enhancement

There was an additional interest for exploring whether nanoplasmonic events would take place using this same configuration, although the main interest of the simulation was not focused on the field enhancement phenomena.

In chapter 2, Gold was said to be the preferable material in field enhancement experiments, and this was due to its high thermal conductivity. Titanium otherwise, has a smaller heat conductivity and it will damage more easily, meaning it will be less likely to generate signal amplification. Usually the metals are coated with a protecting layer, like a sapphire plate, which acts as a heat dissipator that protects the nanostructure from thermal damage both during nanofabrication and when it is illuminated by the femtosecond laser [3]. Still, this is a too elaborate perspective for the study.

Though no conductivity parameter is specified in OSIRIS, the structure features the expected behaviour of a low conductivity material, making the magnitude of the enhancement go up only by a factor smaller than 10, which is quite low.

One can see too that the bigger the power of the laser, the smaller is the electric field amplification on the vicinity of the tips. A bigger power will damage the structure more prominently, meaning the electrons will not be able to oscillate.

It is also important to account for the slit size δ_{slit}, which is too big comparing to the ones used for field enhancement experiments, where the slit size is some tenths smaller than the wavelength. The degree of field enhancement is significantly affected by the geometrical shape of the nanostructure, as revealed in previous investigations of different shapes of particles, wires, and tips [50], [51], [52]. From the geometry of the configuration in the OSIRIS simulation, the ratio $\frac{\lambda}{\delta_{slit}}$ is approximately 2.67, which is relatively small. Using a smaller opening would confine a bigger amount of electrons per unit of volume, therefore a bigger constructive interference of oscillation modes, important for the amplification, would be likely to happen. The simulation with the smaller slits, in spite of showing a small increase, is consistent with this fact.

As a conclusion, field enhancement, due to the fact that in reality involves a solid crystalline structure, is probably more homogeneous along the target surface and can have even higher peaks, but the electron binding for that situation is not implemented in OSIRIS (only Coulomb interactions) and therefore cannot be modelled correctly.

Chapter 6

Conclusions

In this thesis, a comprehensive approach for the conception of a laser-plasma interaction simulation was presented and the possibility of implementing a metallic structure as a heavily dense plasma in a PIC code is explored. A deep investigation of the behaviour of species inside a plasma slab and its understanding by means of other techniques is also shown, with details about their implementation and retrieval methods. In the following sections some conclusions and future perspectives of this study-area are presented.

6.1 Achievements and improvements

Even before the execution of this work, there was an awareness when looking at the complexity for the implementation of a structure like a metallic slab in a computational code such as the PIC.

A great achievement was the observation of low scale phenomena in extremelly short time scales. The use of a tool such as OSIRIS has in fact this same advantage, the capability of providing the evolution of matter in a very narrow time interval, a characteristic which makes it distinct from most of the other simulation codes.

In spite of being expected the incompatibility with some of the models mentioned before, it is clear that OSIRIS has some limitations for the conception of a metallic foil. Some of the values implemented to 'forge' the Titanium were sustained by arguments which in a certain point lose their validity. The plasma frequency is dependent on the electron number density, which is a function of the ionization rate. The given value for this parameter (3.55 electrons per Titanium atom) was a mere average for a temperature of 10 eV, which is far above the room temperature, although it provides the typical magnitude for a solid density plasma ($\sim 10^{23}$ cm^{-3}). At higher peak intensities the first cycles of the pulse can already completely ionize the Ti atoms which leads to an approximately 7 times higher electron density.

The kinetic energy in OSIRIS, which was used for the temperature diagnostics, is calculated by the relativistic formula $K = \sqrt{p^2 + 1} - 1$, where p is the particle momentum. The problem is that room temperature ($p \sim 10^{-7}$) in a relativistic perspective is 0 at simple precision, something which raised the need for a diagnostic in double precision. The accuracy of the diagnostics, however, has a bigger

tendency for numerical errors in the way the temperature is computed.

It is important to highlight that a 2D simulation using the parameters mentioned, with a duration of 15 ps and a number of particles per cell of 60×60, is a relatively heavy simulation, thus requiring several restarts (restarts in the sense that a new simulation will start with the exact same conditions of the last iterate of the previously lanched simulation). This is due to the fact that the cluster where these simulations took place has a maximum of 12 h duration for each simulation, and so each simulation for temperature and density diagnostics took around 3 days to accomplish. Therefore, for a thorough study and due to limiting resources, the preference was given to the extreme cases, i.e., the 10^{14} W/cm^2 and 10^{16} W/cm^2 intensities. The 10^{15} W/cm^2 intensity was only used in shorter simulations.

The resolution of the grid itself was theoretically not the best one. For collisional processes the system should be resolved ideally to the Debye length - $\lambda_{Debye} = \sqrt{\frac{\varepsilon_0 k_B T}{e^2 m}}$ - since by resolving the fields at λ_{Debye} the interaction between particles, especially in terms of collisions, could be correctly modelled as this length is temperature dependent and this is inherent to the collision dynamics. Still, the value of the Debye length for a temperature of the order of 100 eV is $\lambda_{Debye} \simeq 0.15$ nm. Remind that the thickness of the foil itself (100 nm) is already more than 600 times bigger than λ_{Debye}, and for the slit size is 1800 times bigger, while for a smaller temperature the value becomes even smaller. The most adequate way found to improve the results and yet ensuring not so long simulation durations was by raising the number of particles per cell.

Another interesting feature was trying to match two different approaches, in our situation to check whether OSIRIS simulations can reproduce the two temperature model predictions. It is obvious that the model for both approaches of a metal are distinct. In OSIRIS, the metal is modelled as a gas consisting of charged particles with high densities at low temperature. In the case of the TTM, the structure is nothing but a compact structure with a bound system of electrons and vibrating lattice phonons. The temperature dynamics is distinct for both cases, as for one side the TTM doesn't include field acceleration and on the other hand OSIRIS is not 'equipped' with a function for a rigid object. In general there is an agreement between both in terms of the collective behaviour of the species' heating - the electrons cool down after reaching a peak value and as this happens the protons slowly begin to warm up -, the difference lies within the correct numbers of peak and equilibrium temperatures.

6.2 Future Work

The demonstration of solid targets interacting with powerful lasers through the use of leading-edge computational algorithms is giving way to several breakthroughs in the ultrafast optics field. This is due to their possible scalability in terms of temperature growth and expansion rates. Investigation applied to several different metals as well as new configuration schemes shall give guidance in the achievement of major breakthroughs for the understanding of the laser energy deposition in matter and nanoplasmonic phenomena.

6.2.1 OSIRIS

Although it is implemented in OSIRIS, the collisional function is not used frequently since the code was conceived mainly for high energy particles where collision become less significant. This work, therefore, led to a better insight regarding the collision function in OSIRIS and to benchmark the regimes at which different effects take place.

For future work, a module for implementing a metal in OSIRIS can be developed, by requiring an initial temperature (instead of giving the normalized thermal velocities) and by setting the collisions in two different regimes: a fixed coulomb logarithm in the beginning if the target is below a critical temperature, and an automatic value after the metal has reached a higher temperature.

6.2.2 Plasma diagnostics

As illustrated in section 3.1 (fig. 3.1), the heated double slit is probed by a high harmonic source for different times after heating. The recorded interference pattern depends on the slit width and separation.

The slit width will vary as the target expands. During the several time steps there will be an increasing density profile at the empty space and this will generate a gradient in terms of refractive index. The harmonics sent through the slits will refract differently as the target is successively expanding and the intensity pattern will become modified. For measuring electron densities of a laser created plasma plume, the probe beam wavelength should be well away from any absorption resonances so that contributions to the refractive index from bound electrons is negligible compared to that of free electrons in the plasma. In the limit of a non-collisional system, the refractive index n can be expressed as $n = \sqrt{1 - \frac{n_e}{n_c}}$, where n_e is the electron number density and n_c is the critical electron density created by the probe wavelength. The probe penetrates the plasma only to the point where the electron density reaches the critical density, where reflection occurs. The ratio of the fringe shift to the fringe spacing in the diffraction pattern can be related to the line integral of electron density along the probe beam path by

$$\Delta = \frac{1}{2\lambda n_c} \int n_e(l)\, dl \tag{6.1}$$

where λ is the probe wavelength and l is the optical path length through the plume. A 2D mapping of the density can be obtained, for example, with the help of Abel inversion technique [53]. The most common methods for measuring the density of laser-produced plumes are of interferometric nature, being the Michelson, Mach-Zender and Nomarski interferometers the most used choices.

Important is also the fact that the diffraction pattern in the experiment is observed in the far-field, which corresponds to the *Fraunhofer diffraction*. Looking at the simulation box implemented in OSIRIS, the beam can propagate a distance between 0.5 μm and 1 μm after the slit ($I_0 = 10^{16}$ W/cm^2), which corresponds to a Fresnel number $F = \frac{a^2}{L\lambda}$ between 0.5625 and 1.125 (a is the slit size, L is the distance slit to the screen and λ is the probe wavelength) for the 5th harmonic of the fundamental beam. This range of values is pretty much close to 1, meaning that the observed diffraction pattern corresponds to the Fresnel regime, which is different from the Fraunhofer case. Increasing the propagation distance to $10\ \mu m$ results in a Fresnel number $F \simeq 0.056$, which satisfies the condition $F \ll 1$ for the Fraunhofer

regime. Therefore, the diffraction pattern can be directly observed in the simulation if the window on the x_1 direction is increased. This pattern can be observed and extracted from the simulations to record data for future experiments.

Bibliography

[1] M. Schreiner, M. Strlic, R. Salimbeni. *Handbook on the use of lasers in conservation and conservation science*. COST Office, 2008. ISBN-10: 973 88109 30.

[2] M.I. Stockman. Nanoplasmonics: The physics behind the applications. *Physics Today*, February 2011. DOI:10.1063/1.3554315.

[3] S. Kim, J. Jin, Y.J. Kim, I.Y. Park, Y. Kim, Seung-Woo Kim. High-harmonic generation by resonant plasmon field enhancement. *Nature*, June 2008. DOI:10.1063/1.3554315.

[4] M.I. Stockman, L.N.Pandey, T.F. George. Inhomogeneous localization of polar eigenmodes in fractals. *Phys. Rev. B*, February 1996. DOI:10.1103/PhysRevB.53.2183.

[5] S. Lal, S.E. Clare, N.J. Halas. Nanoshell-enabled photothermal cancer therapy: impending clinical impact. *Acc. Chem. Res.*, December 2008.

[6] H.A. Atwater, A. Polman. Plasmonics for improved photovoltaic devices. *Nature Materials*, September 2010.

[7] Z.M. Sheng, S.M. Weng, L.L. Yu, W.M. Wang, Y.Q. Cui, M. Chen, J. Zhang. Absorption of ultrashort intense lasers in laser-solid interactions. *Chinese Physics B*, July 2015. DOI: 10.1088/1674-1056/24/1/015201.

[8] P. Gibbon. *Short Pulse Laser Interactions with Matter - An Introduction*, chapter 6. Imperial College Press, 2005.

[9] T.Z. Esirkepov. Exact charge conservation scheme for particle-in-cell simulation with an arbitrary form-factor. *Computer Physics Communications*, June 2001. DOI:10.1063/1.3554315.

[10] R.A.Fonseca, L.O.Silva, F.S.Tsung, V.K.Decyk, W.Lu, C.Ren, W.B. Mori, S.Deng, S.Lee, T.Katsouleas, J.C.Adam. Osiris: A three-dimensional, fully relativistic particle in cell code for modeling plasma based accelerators. In *International Conference on Computational Science (3)*, 2002.

[11] P. Gibbon. *Short Pulse Laser Interactions with Matter - An Introduction*. Imperial College Press, 2005. ISBN: 978-1-86094-135-4.

[12] R. Fonseca. *Experimental and Numerical Study of Laser-Plasma Electron Accelerators*. PhD thesis, Instituto Superior Técnico, October 2002.

[13] H. N. Chapman, K. Nugent. Coherent lensless x-ray imaging. *Nature Photonics*, June 2010. DOI:10.1038/nphoton.2010.240.

[14] J. Nejdl. *X-ray Laser Seeded by High-order Harmonic Beam*. PhD thesis, Czech Technical University in Prague, 2009.

[15] H. N. Chapman, P. Fromme, A.Barty, T. A. White, R. A. Kirian, A. Aquila, M. S. Hunter, J. Schulz, D.P. DePonte, U. Weierstall, R. B. Doak, F. R. N. C. Maia, A. V. Martin, I. Schlichting, L. Lomb, N. Coppola, R. L. Shoeman, S. W. Epp, R. Hartmann, D. Rolles, A. Rudenko, L. Foucar, N. Kimmel, G. Weidenspointner, P. Holl. Femtosecond x-ray protein nanocrystallography. *Nature*, February 2011. DOI:10.1038/nature09750.

[16] C. G. Schroer, P. Boye, J. M. Feldkamp, J. Patommel, A. Schropp, A. Schwab, S. Stephan, M. Burghammer, S. Schöder, C. Riekel. Coherent x-ray diffraction imaging with nanofocused illumination. *Physical Review Letters*, August 2008. DOI: 10.1103/PhysRevLett.101.090801.

[17] J. Goodman. *Introduction to Fourier Optics*, chapter 9. The McGraw-Hill Companies, 1996.

[18] A.V. Martin, A.J. D'Alfonso, F. Wang, R. Bean, F. Capotondi, R.A. Kirian, E. Pedersoli, L. Raimondi, F. Stellato, C.H. Yoon, H.N. Chapman. X-ray holography with a customizable reference. *Nature Communications*, July 2014. doi:10.1038/ncomms5661.

[19] W. F. Schlotter, R. Rick, K. Chen, A. Scherz, J. Stöhr, J. Lüning, S. Eisebitt, Ch. Günther, W. Eberhardt, O. Hellwig, I. McNulty. Multiple reference fourier transform holography with soft x rays. *Applied Physics Letters*, 2006. doi: 10.1063/1.2364259.

[20] M.Born, E. Wolf. *Principles of Optics: Electromagnetic Theory of Propagation, Interference and Diffraction of Light*. Cambridge University Press, 1980. ISBN-13: 978-0521642224.

[21] H. M. Milchberg, R. R. Freeman, S. C. Davey, R. M. More. Resistivity of a simple metal from room temperature to 10 million k. *Physical Review Letters*, 1988. DOI:10.1103/PhysRevLett.61.2364.

[22] R. Fedosejevs, R. Ottmann, R. Sigel, G. Kühnle, S. Szatmari, F. P. Schäfer. Absorption of femtosecond laser pulses in high-density plasma. *Physical Review Letters*, 1990. DOI:10.1103/PhysRevLett.61.2364.

[23] F. Brunel. Not-so-resonant, resonant absorption. *Physical Review Letters*, July 1987. DOI:10.1103/PhysRevLett.59.52.

[24] J M Ziman. The localization of electrons in ordered and disordered systems iii. quantum-mechanical particles in 'free' bands. *Journal of Physics C: Solid State Physics*, 1969. DOI:10.1103/PhysRevLett.59.52.

[25] E.S. Weibel. L'équation de vlasov dans la théorie spéciale de la relativité. *Plasma Physics*, 1967.

[26] W. Rozmus, V. T. Tikhonchuk. Skin effect and interaction of short laser pulses with dense plasmas. *Physical Review A*, June 1990. DOI:10.1103/PhysRevA.42.7401.

[27] J. Byskov-Nielsen, J. Savolainen, M.S. Christensen, P. Balling. Ultrashort pulse laser ablation of copper, silver and tungsten: experimental data and two-temperature model simulations. *Applied Physics A*, 521:447–453, March 2011. doi:10.1007/s00339-011-6363-7.

[28] L. Jiang, H.L. Tsai. Improved two-temperature model and its application in ultrashort laser heating of metal films. *Journal of Heat Transfer*, 2005.

[29] J.K. Chen, D.Y. Tzou, J.E. Beraun. A semiclassical two-temperature model for ultrafast laser heating. *International Journal of Heat and Mass Transfer*, 2005.

[30] S.I. Anisimov, A.M. Bonch-Bruevich, M.A. El'yashevich, YaA Imas, N.A. Pavlenkoa, G.S. Romanov. Effect of powerful light fluxes on metals. *Soviet Physics Technical Physics*, 1967.

[31] M.I. Anisimov, I.M. Lifshitz, L.V. Tanatarov. Relations between electrons and the crystalline structure. *Soviet Physics*, 1957.

[32] W.L. McMillan. Transition temperature of strong-coupled superconductors. *Physical Review*, 1968.

[33] N.W.Ashcroft, N.D.Mermin. *Solid State Physics*, chapter 2. Saunders College Publishing, 1976.

[34] S.D. Brorson, A Kazeroonian, J.S. Moodera, D.W. Face, T.K. Cheng,E.P. Ippen, M.S. Dresselhaus, G. Dresselhaus. Femtosecond room-temperature measurement of the electron-phonon coupling constant in metallic superconductors. *Physical Review Letters*, 1990.

[35] D.E. Gray. *American Institute of Physics Handbook*. McGraw-Hill Book Company, 1957.

[36] L. Spitzer Jr., R. Härm. Transport phenomena in a completely ionized gas. *Physical Review*, 1952.

[37] Ya. B. Zel'dovich, Yu. P. Raiser. *Physics of Shock Waves and High Temperature Hydrodynamic Phenomena*. Academic Press, 1966.

[38] M.D. Rosen. Scaling laws for femtosecond laser-plasma interactions. Technical report, Lawrence Livermore National Laboratoiy, 1990.

[39] D. Jou, J. Casas-Vazquez, G. Lebon. Extended irreversible thermodynamics revisited. *Rep Prog Phys*, 1999.

[40] D.D. Joseph, L. Preziozi. Heat waves. *Reviews of Modern Physics*, January 1989. DOI:10.1103/RevModPhys.61.41.

[41] D.D. Joseph, L. Preziozi. Addendum to the paper heat waves. *Reviews of Modern Physics*, April 1990. DOI:10.1103/RevModPhys.62.375.

[42] T.T. Luu, M. Garg, S. Yu. Kruchinin, A.Moulet, M.Th.Hassan. Extreme ultraviolet high-harmonic spectroscopy of solids. *Nature Physics*, 521, May 2015. doi:10.1038/nature14456.

[43] P.B. Corkum. Plasma perspective on strong-field multiphoton ionization. *Physical Review Letters*, 1993. DOI: 10.1088/1674-1056/24/1/015201.

[44] J. L. Krause, K.J. Schafer, K.C. Kulander. High-order harmonic generation from atoms and ions in the high intensity regime. *Physical Review Letters*, June 1992. DOI: 10.1103/PhysRevLett.68.3535.

[45] L. Veisz, W. Theobald, T. Feurer, H. Schillinger, P. Gibbon, R. Sauerbrey. Three-halves harmonic emission from femtosecond laser produced plasmas. *Physics of Plasmas*, August 2002. DOI: 10.1063/1.1493794.

[46] L. Veisz, W. Theobald, T. Feurer, H. Schwoerer, I. Uschmann, O. Renner. Three-halves harmonic emission from femtosecond laser produced plasmas with steep density gradients. *Physics of Plasmas*, May 2004. DOI: 10.1063/1.1748174.

[47] H.-K. Chung, M.H. Chen, W.L. Morgan, Yu. Ralchenko, R.W. Lee. Flychk: Generalized population kinetics and spectral model for rapid spectroscopic analysis for all elements. *High Energy Density Physics*, 1:3, 2005.

[48] K. Eidmann, J. Meyer ter Vehn, T. Schlegel, S. Hüller. Hydrodynamic simulation of subpicosecond laser interaction with solid-density matter. *Physical Review E*, July 2000. DOI: 10.1103/PhysRevE.62.1202.

[49] E. Majchrzak, J. Dziatkiewicz. Application of the two-temperature model for a numerical study of multiple laser pulses interactions with metals. *Scientific Research of the Institute of Mathematics and Computer Science*, 11:63–70, July 2012.

[50] E.X. Jin, X. Xu. Enhanced optical near field from a bowtie aperture. *Applied Physics Letter*, 11:63–70, July 2006. DOI: 10.1103/PhysRevE.62.1202.

[51] T.D. Onuta, M. Waegele, C.C. DuFort, W.L. Schaich, B. Dragnea. Optical field enhancement at cusps between adjacent nanoapertures. *Applied Physics Letter*, 11, 2007.

[52] W.X. Sun, Z.X. Shen. Optimizing the near field around silver tips. *J Opt Soc*, 11, 2003.

[53] S. Merk, A. Demidov, D. Shelby, I.B. Gornushkin, U. Panne, B.W. Smith , N. Omenetto. Diagnostic of laser-induced plasma using abel inversion and radiation modeling. *Applied Spectroscopy*, August 2013. doi: 10.1366/12-06929.